早稲田大学審査学位論文(博士)

博士論文

Nuclear shapes in the inner crust of a neutron star

中性子星内殻における原子核の形状

早稲田大学大学院理工学研究科
物理学及応用物理学専攻
理論核物理学研究

親松　和浩

Kazuhiro Oyamatsu

1994年10月

①

博士論文

Nuclear shapes in the inner crust of a neutron star

中性子星内殻における原子核の形状

早稲田大学大学院理工学研究科
物理学及応用物理学専攻
理論核物理学研究

親松　和浩
Kazuhiro　Oyamatsu

1994年10月

Contents

Chapter 1

Introduction

Nuclei we usually observe are essentially spherical except that some nuclei are deformed to some extent. However, under some condition, the shape of stable nuclei may not be spherical. This possibility was pointed out with the compressible liquid-drop model by two groups about ten years ago [1,2]; namely as the density of the matter increases from subnuclear to nuclear density, the stable nuclear shape may change from sphere to cylinder, slab, cylindrical hole and spherical hole before going into uniform matter.

These non-spherical nuclei are expected to exist in the inner crust of a neutron star and in the transient matter during the collapse of the supernova core. For brevity, we refer to the matter in the neutron-star crust as NSM and to the matter in the supernova core as SNM. NSM is charge neutral and β-stable, being composed of neutrons, protons and electrons. The temperature of NSM can be taken as zero in a good approximation because it is much lower than the Fermi energies of neutrons and protons. Electrons are relativistic and distributed almost uniformly. The electron Fermi energy is so high that the β-stability is achieved by making the matter extremely neutron rich. The proton fraction in the nucleons, Y_p, is about 3~5% in NSM. Protons are localized so as to make full use of nuclear forces. We refer to the part in which protons and neutrons coexist as "nucleus" in the following. Some neutrons drip out of the nuclei to form a neutron gas, while the nuclei form a lattice to reduce the Coulomb energy. In addition to the three kinds of particles included in NSM, neutrinos are also trapped in SNM, and both Y_p and the temperature of SNM are significantly higher than those of NSM.

The shape of the above nucleus has been studied in the liquid-drop model by the authors of refs. [1-4]. Ravenhall, Pethick and Wilson [1] made the liquid-drop calculations of SNM by taking account of the five nuclear shapes, of which three were

non-spherical. Recently, Lorenz, Ravenhall and Pethick [3] studied NSM by the same method with an improved nuclear interaction. Cooperstein and Baron [5] and Lattimer and Swesty [6] also considered the geometrical effects in more simplified ways. All of the above authors assumed specific nuclear interactions and used the Coulomb energy calculated in the Wigner-Seitz cell approximation. On the other hand, Hashimoto, Seki and Yamada [2] presented a geometrical argument using the necessary condition for equilibrium that the surface energy is twice as much as the Coulomb energy. Later, Oyamatsu, Hashimoto and Yamada [4] refined the treatment, taking account of several lattice types, and determined the energetically most favorable nuclear shape as a function of the volume fraction of the nucleus in the cell. The result of ref. 4 is independent of specific nuclear interactions because it is derived from a purely geometrical argument. Although the primary interest of that study was in NSM, the above result is also valid for SNM.

In this thesis we discuss the existence of the non-spherical nuclei in NSM. In chapter 2, we give a brief sketch of a neutron star to summarize the present understandings of NSM related to this work. The study of the matter provides us with the basic information for understanding the structure and evolution of a neutron star. Actually some implications of the existence of the non-spherical nuclei have been discussed by Lorenz, Ravenhall and Pethick [3] for NSM and also by Coopertein and Baron [5] for SNM.

We start with the discussion of NSM at subnuclear densities by reviewing the predictions in the compressible liquid-drop model in chapter 3. We follow the discussions by Hashimoto, Seki and Yamada [2] and Oyamatsu, Hashimoto and Yamada [4].

Since the predictions with the liquid-drop models by the two groups [1,2], no attempt has been made to take account of realistic nucleon distributions beyond the liquid-drop model for NSM, although Williams and Koonin [7] and Lassaut et al. [8] made Thomas-Fermi calculations for SNM, which is closer to symmetric nuclear matter. In chapter 4, we perform the Thomas-Fermi calculation and investigate

quantitatively the nuclear shape and the phase transitions accompanying the shape change in NSM. We consider several nuclear shapes and lattice types with parametrized neutron and proton distributions, and perform the calculations with four different energy density functionals. The method employed here is an extension of Arponen's [9] in his study of NSM composed of spherical nuclei. The present author reported simplified preliminary calculations for NSM and SNM [10]. In chapter 4, we consider more carefully the nuclear surface energy from the viewpoint of the energy density functional and the nucleon distributions.

Moreover, shell effects are important in normal nuclei. Therefore, in chapter 5 we calculate the shell energies of the above non-spherical nuclei. Although a self-consistent calculation is desirable, considerable difficulties are expected to perform it. Since masses of normal nuclei are well reproduced with the description of the liquid-drop energies supplemented with the shell energy corrections, we adopt this strategy to the present problem. Namely, we calculate the shell energies of the non-spherical nuclei by making full use of the result of the Thomas-Fermi calculation. Specifically, we construct the non-spherical single-particle (SP) potential with the energy-density functional and resultant nucleon distributions. Then, we calculate the SP energies in these SP potentials and extract the shell energies using an appropriate prescription. The central component of the SP potential is constructed with use of the energy-density functionals and resultant nucleon distributions paying special attention to the finite range effects of nuclear interactions. In addition to this central potential, we add a spin-orbit potential in a simple form. We introduce three parameters in these SP potentials and the values of these parameters are determined so as to be consistent with SP energies in normal nuclei. With the SP energies in the non-spherical nuclei we derive shell energies of non-spherical nuclei. We add these shell energies to the energies calculated in the Thomas-Fermi calculation and discuss existence of the non-spherical nuclei.

In chapter 6, we discuss how the existence of the non-spherical nuclei affects the neutron star. Since studies along this line have just begun, we merely mention some observations which we have at the present stage.

Finally, chapter 7 is devoted to the conclusion of this study.

Chapter 2

Brief sketch of a neutron star

In this chapter, we take a glance at the structure of a typical neutron star for the discussion in the following chapters.

A neutron star is a compact object with the radius of ~10 km and the mass of ~1 $M_\odot$ (solar mass unit). The density profile in a neutron star is mainly determined by the high-density part of the equation of state (EOS) of neutron-star matter above normal nuclear density ($\rho_0 \approx 2.8\times10^{14}$ g/cm^3 or $n_0 \approx 0.16$ fm^{-3}). In this thesis, the density is mainly shown in terms of the nucleon number density in fm^{-3}. Conversion from the nucleon number density n_b fm^{-3} to the matter density ρ (g/cm^3) can be obtained from

$$\rho \text{ (g/cm}^3) \approx 1.7\times10^{15}\, n_b \text{ (fm}^{-3}). \qquad (2.1)$$

Various EOS's of neutron matter and symmetric nuclear matter are available. An EOS of the neutron-star matter is constructed from the EOS of these hypothetical nuclear matter but in most cases EOS of neutron-star matter can be approximated to that of pure neutron matter. The high-density EOS of neutron matter is quite uncertain even at present. In this thesis, we take an EOS calculated with the two-body potential UV14 and the three-nucleon potential TNI by Wiringa, Fiks and Fabrocini [11] as a standard high-density EOS of nuclear matter. This EOS is a revised version of the one calculated by Friedman and Pandharipande [12] obtained by correcting some error at high densities.

The density profile in a neutron star is obtained with EOS by solving the Tolman-Oppenheimer-Volkoff equation which will be described in chapter 6. The central density of a neutron star depends on EOS and the mass of the star; typically it can become about 8 times as high as the normal nuclear density. In Fig. 2-1, we show the density profile in a typical 1.4 $M_\odot$ neutron star. As the density of matter increases

from atmosphere to the stellar center, the neutron star is divided into three parts: the outer and inner crusts, and the core.

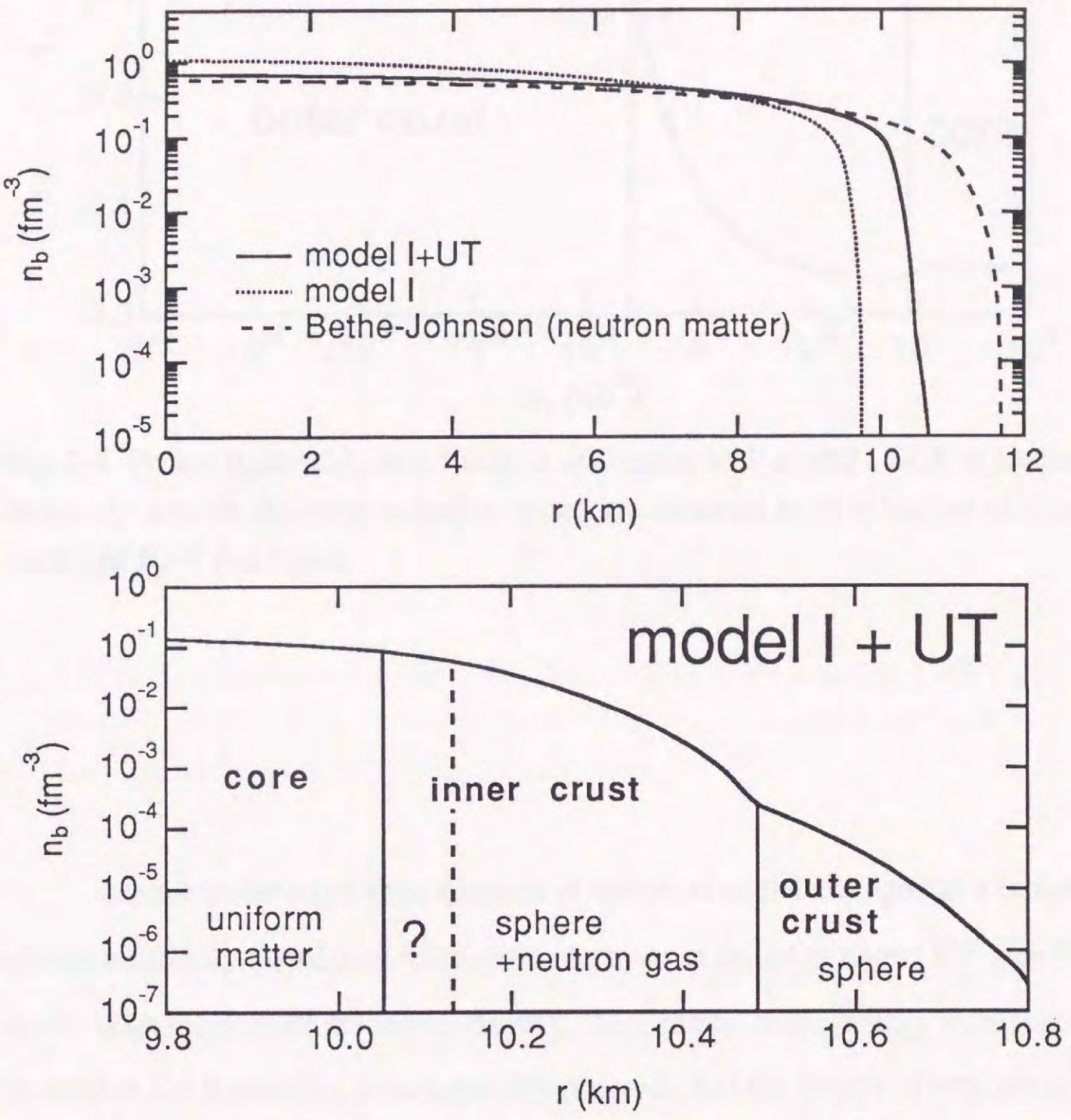

Fig. 2-1. Density profile in a typical 1.4 $M_\odot$ neutron star. In the upper box, three different EOS are used to calculate the density profile. Model I is an EOS in chapter 4 and model I + UT is a modified version of model I which will be described in chapter 6. For comparison we also calculate the density profile with an EOS of pure neutron matter by Bethe and Johnson [13]. The lower box shows the structure of the crust with the modified model I EOS.

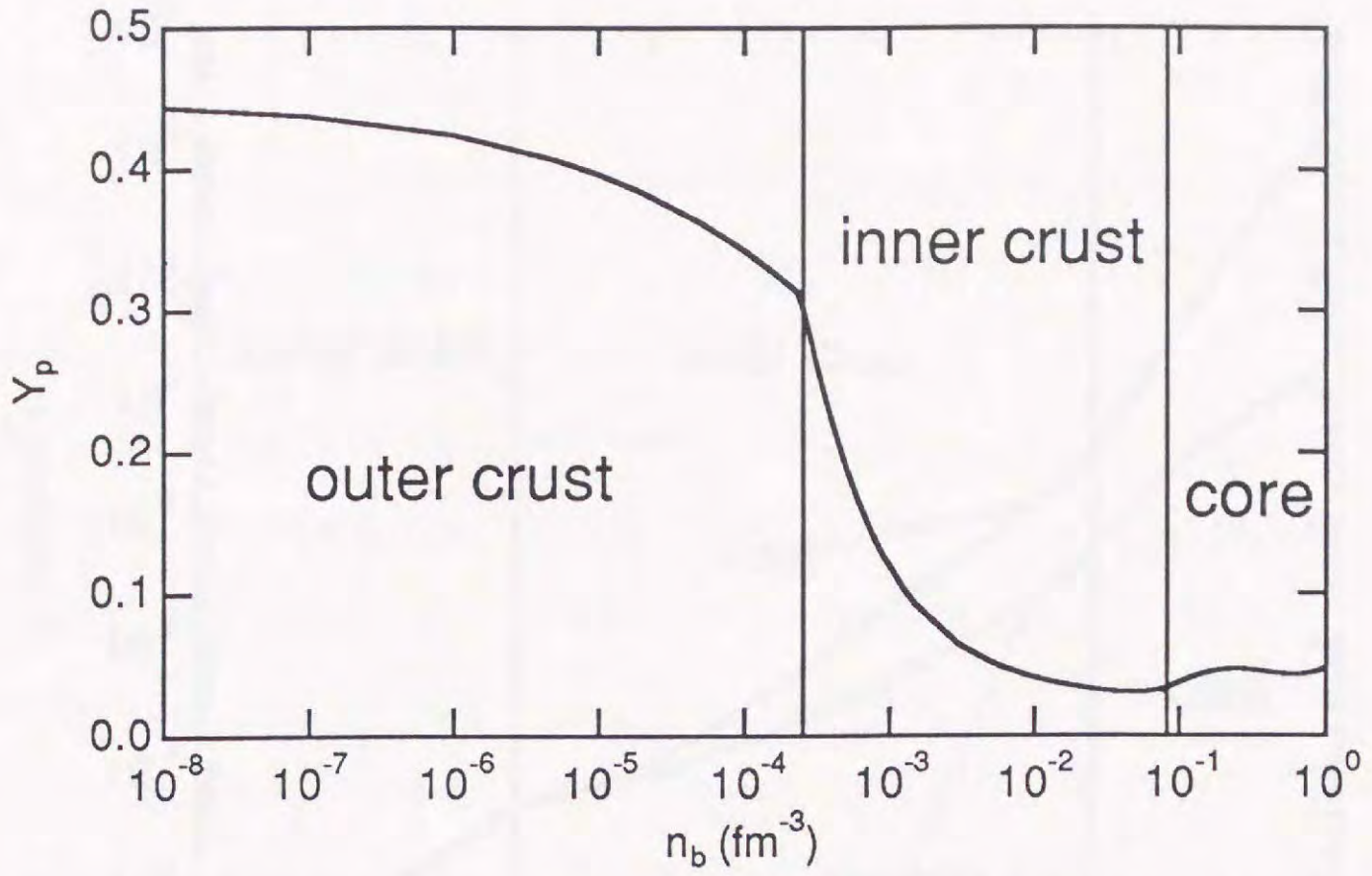

Fig. 2-2. Proton fraction Y_p as a function of density with model I EOS in chapter 4. The shape of nuclei in the inner and outer crusts are assumed to be spherical to calculate values of Y_p in this figure.

Matter in the outer crust consists of spherical nuclei arranged in a lattice with almost uniformly distributed relativistic electrons at densities above 10^7 g/cm^3(10^{-8} fm^{-3}). With increase of the matter density, the electron Fermi energy increases. In order to achieve the β-stability, neutronization proceeds and the neutron Fermi energy also increases. In Fig. 2-2, the proton fraction Y_p is shown as a function of density. We see from this figure that the electron fraction, which is equal to Y_p due to the charge neutrality condition, decreases with increase of density because of the neutronization. At about 4×10^{11} g/cm^3 (2.4×10^{-4} fm^{-3}), the neutron Fermi energy reaches zero and this density is called neutron drip point (NDP). The regions at densities below and above NDP are called the outer crust and inner crust, respectively. In the inner crust some neutrons drip out of nuclei. Therefore, nuclei above 4×10^{11} g/cm^3 are embedded in the sea of dripped neutrons.

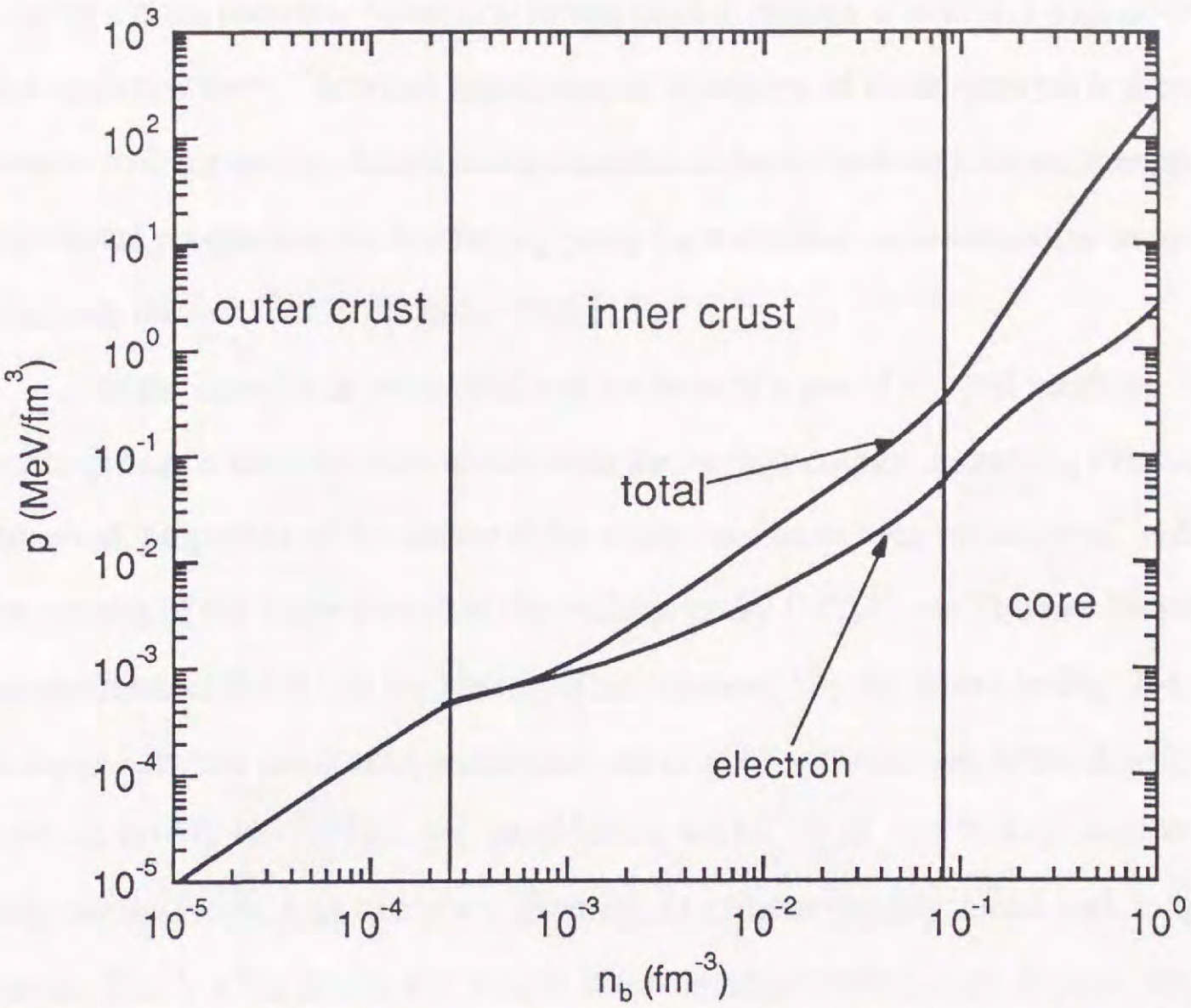

Fig. 2-3. Total and electron pressures as functions of matter density with model I EOS in chapter 4. The shape of nuclei in the inner and outer crusts are assumed to be spherical to calculate the pressures in this figure.

In Fig. 2-3, we show the pressure of neutron-star matter as a function of matter density. We also show the electron pressure in this figure for comparision. While the electron pressure is dominant in the outer crust, nucleon degrees of freedom become rapidly important in the inner crust by the presence of dripped neutrons and are dominant in the core.

In Fig. 2-4, we show neutron and proton distributions along the line joining the centers of neighboring nuclei. In the outer crust, nuclei are located far away from each other, and the energy of matter can be taken, in the first approximation, as the masses of an isolated nuclei supplemented with the kinetic energy of relativistic electrons and the lattice Coulomb energy. In 1972, Baym, Pethick and Sutherland [14] calculated the nuclides existing in the outer crust using experimental mass data and predicted mass

data by a mass formula. Necessary information is masses of nuclides with N=50 and 82 due to shell effects. Therefore measurement of masses of these nuclides is directly related with the determination of the nuclides in the neutron star. Experimental and theoretical progress in the last twenty years have enabled us to determine more precisely the nuclides in the outer crust [15].

In the inner crust we should take account of a gas of dripped neutrons. We can no longer use a mass formula to calculate the nuclear energy. Assuming that nuclei are spherical, properties of the matter in the inner crust have been investigated within the framework of the commpressible liquid-drop model [16,17], the Thomas-Fermi approximation [9,18] and the Hartree-Fock method [19]. As shown in Fig. 2-4, the distance between the nearest nuclei become smaller with increase of the density. At $n_b \approx 0.06$ fm^{-3} ($\rho \approx 1\times10^{14}$ g/cm^3), neighboring nuclei are so near that interactions with neighboring nuclei may become important. At a higher density nuclei melt into uniform matter. This is a big geometric change in the nucleon distributions. Strange things can happen in this transition. Lamb et al. [20] suggested that, when nuclei occupy the sufficient volume fraction in a cell as shown in Fig. 2-5, the spherical bubble (hole) becomes the favorable nuclear shape because the suface area for the bubble shape is smaller than the normal shape.

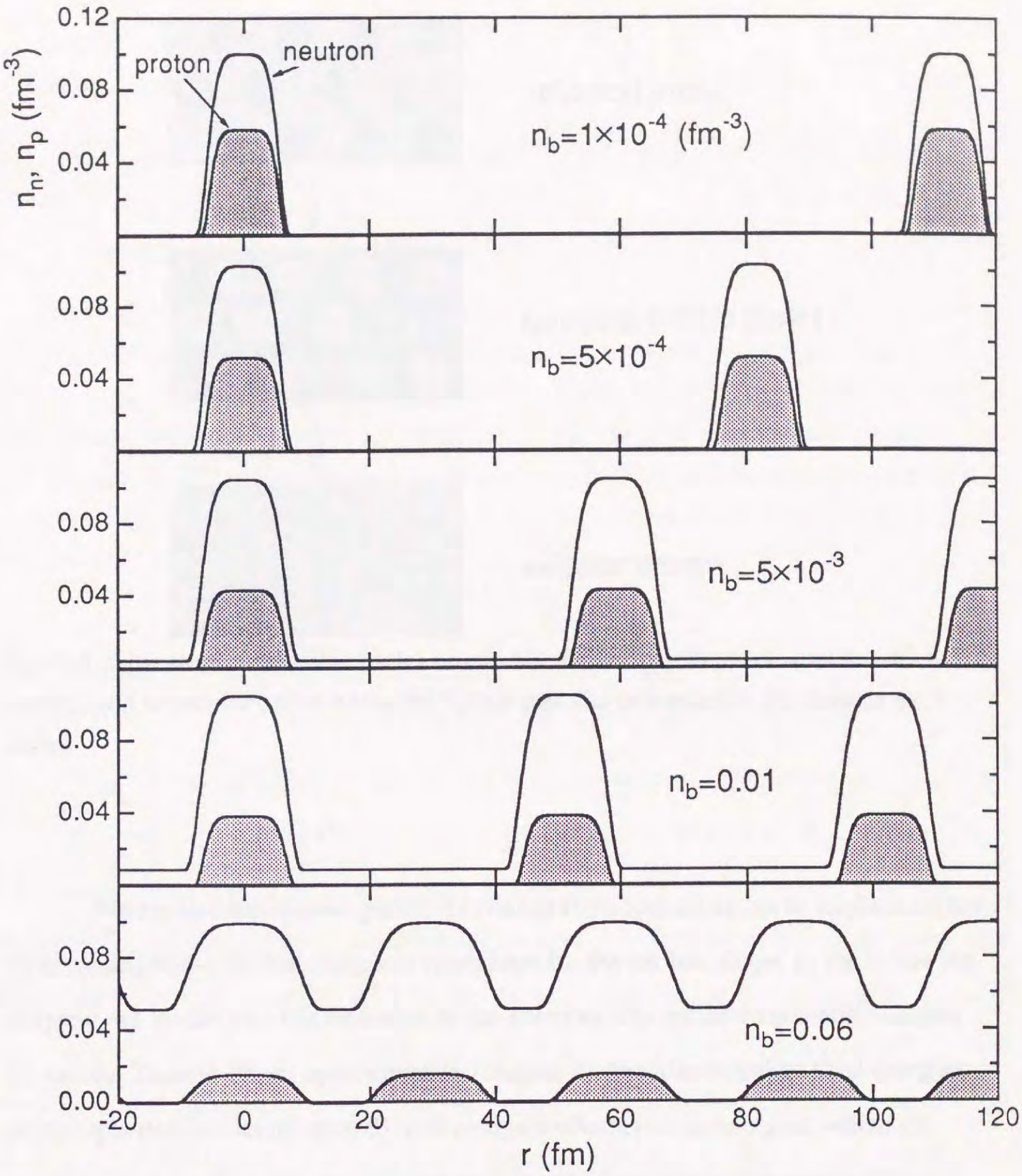

Fig. 2-4. The neutron (upper) and proton (lower, shaded) distributions along the straight lines joining the centers of the nearest nuclei. Calculations are performed in the case of spherical nuclei with model I interaction in chapter 4.

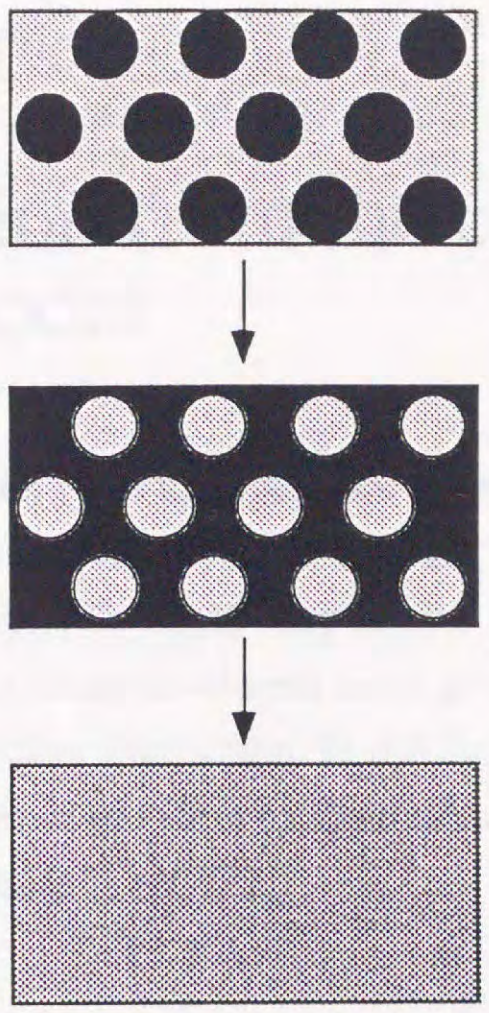

Fig. 2-5. Appearance of bubble (hole) phase. The darker part shows nuclei in which protons and neutrons coexist while the lighter part shows a neutron gas outside the nuclei.

We explore this drastic geometric change from normal nuclei to uniform matter by assuming non-spherical shapes as candidates for the nuclear shape. In the following chapters, we investigate this transition in the compressible liquid-drop model (chapter 3), and the Thomas-Fermi approximation (chapter 4). We also calculate shell energies of non-spherical nuclei (chapter 5) to investigate whether these energies, which are important in normal nuclei, may change the pictures described in the semiclassical treatment.

Chapter 3

Prediction from the compressible liquid-drop model

About ten years ago, possible existence of non-spherical nuclei was first pointed out by Ravenhall, Pethick and Wilson [1] and also by Hashimoto, Seki and Yamada [2] with the compressible liquid-drop model. While the former group used specific nuclear interactions, the latter developed more general geometrical argument independent of any specific nuclear interaction. In this chapter, we describe, in a slightly different form, the argument put forth by Oyamatsu, Hashimoto and Yamada [4] who improved the treatment made in ref. [2].

3.1. Candidates for nuclear shape

The nuclear shapes considered in this thesis are sphere, cylinder, slab, cylindrical hole, and spherical hole. These shapes can be considered as the one-, two- or three-dimensional spheres which minimize the surface energies. The spherical as well as non-spherical nuclei form lattices to minimize the Coulomb energy. We consider three lattice types for spherical nuclei. They are body-centered cubic (bcc), face-centered cubic (fcc) and simple cubic (sc). In the cases of cylindrical nuclei, we consider the two-dimensional lattice on the plane perpendicular to the central axes of the cylinders. The lattice types for cylindrical nuclei treated in this thesis are hexagnal (hex) and simple square (ss). Fig. 3-1 shows the lattice type to minimize the Coulomb energy for each nuclear shape. The spherical nuclei as well as the spherical hole nuclei form the bcc lattice. The cylindrical nuclei and the cylindrical hole nuclei form the two-dimensional hexagonal lattice, i.e., any cross section perpendicular to their sides shows a pattern of regular hexagon. The slab nuclei form the one-dimensional lattice, i.e., they are all parallel and equally spaced.

The length of the cylinder and the area of the slab are essentially infinite. However, for convenience, we divide the whole space into three-dimensional cells of volume a^3. In this paper, we refer to a as the lattice constant. In the case of spherical nuclei or spherical hole nuclei, each cell contains one nucleus or one hole. For cylindrical nuclei or cylindrical hole nuclei (see fig. 3-2 (a)), the cell is a prism with base area a^2 and height a. The base area is perpendicular to the sides of cylinders or cylindrical holes, and includes one cross section of the cylinder or cylindrical hole. For slab-shape nuclei (see fig. 3-2 (b)), the cell is a cube whose edge is equal to the lattice constant in the direction perpendicular to the surface of the slab.

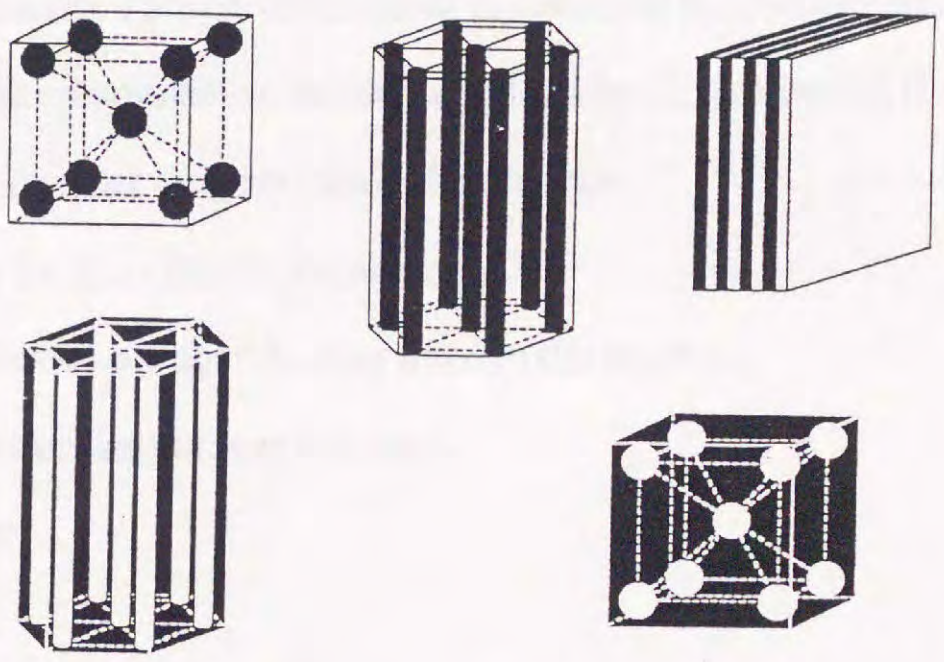

Fig. 3-1 Candidates for nuclear shapes

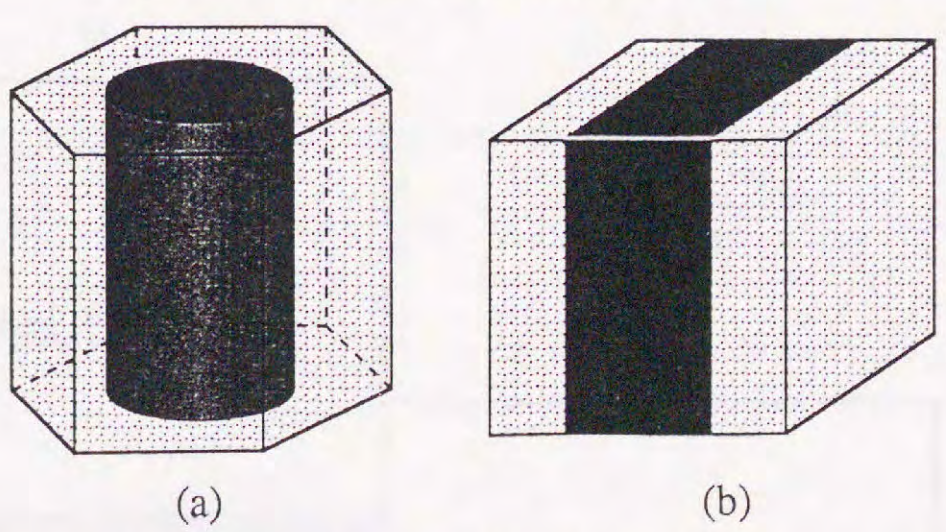

(a) (b)

Fig. 3-2. Unit cells for the cylindrical and slab-shape nuclei.

The above-defined cells are inconvenient for some practical calculations. Therefore, we also define the Wigner-Seitz cell as follows. For spherical (hole) nuclei, it is a sphere with volume a^3. For cylindrical (hole) nuclei, it is a cylinder with base area a^2 and height a.

3.2. Parameters in the nucleon distribution

In the liquid-drop model, a sharp nuclear surface (or boundary) is assumed, and each of the local proton and neutron number densities inside the nucleus and the neutron number density outside the nucleus is assumed to be constant. As shown in Fig. 3-3, the nucleon distributions can be characterized by the following five parameters:

n^{in} : total nucleon number density inside the nucleus,

x : proton number fraction inside the nucleus,

n^{out} : nucleon (neutron) number density outside the nucleus,

u : volume fraction of the nucleus in a cell,

a : lattice constant.

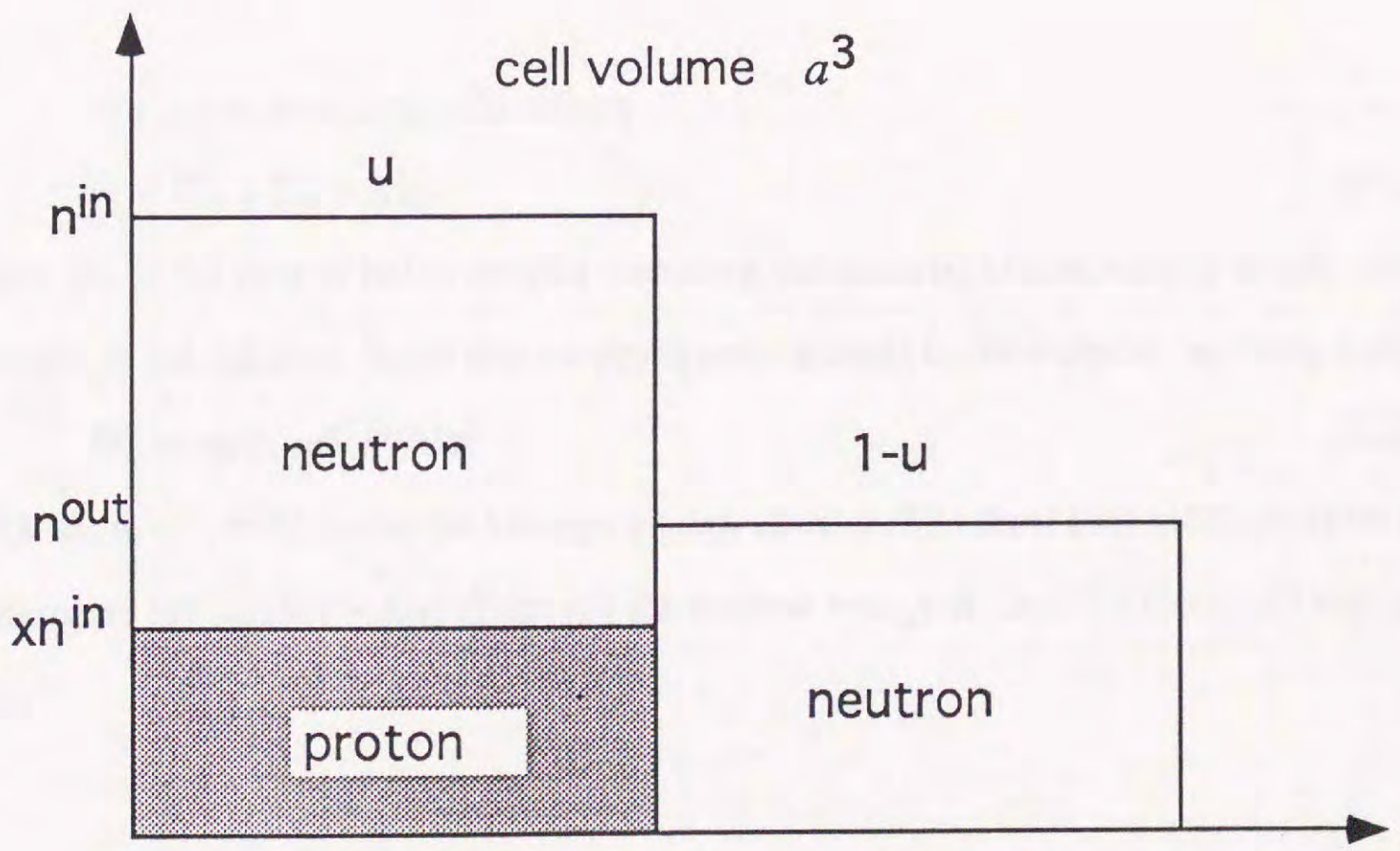

Fig. 3-3. Parameters for nucleon distributions.

Because of the charge neutrality condition, the number of electrons is equal to that of protons. At the densities of interest, electrons are relativistic, and the Coulomb energy variation felt by an electron when it moves around is very small compared with the electron Fermi energy. Therefore we assume a uniform electron distribution with the density xun^{in}.

Ravenhall, Pethick and Wilson (RBP) [1] first pointed out the existence of non-spheerical nuclei in the compressible liquid-drop model for superenova matter. Since supernova matter is much closer to symmetric nuclear matter, the density of a neutron gas outside nuclei is much smaller than that in the neutron star matter. Then, RBP negelcted the outside neutron gas (n_{out}=0) and calculated the energy of the matter with appropriate expressions for the bulk energy and the surface tension. The Coulomb energy was calculated in the Wigner-Seitz approximation.

In the following we demonstrate an argument independent any specific nuclear interaction. Therefore, the result obtained by RBP can be considered as a special case of our general arugument.

3.3. Energy of a cell

We write the energy of a cell as

$$W = W_b + W_s + W_C. \tag{3.1}$$

Here, W_b is the sum of bulk energies including the electron kinetic energy inside and outside of the nucleus. Since this energy is proportional to the volume, we write it as

$$W_b = w_b(u, n^{in}, n^{out,})a^3 \tag{3.2}$$

with $w_b(u, n^{in}, n^{out,})$ being the average energy density. The most important energies to determine the stable nuclear shape are the surface energy W_s and the Coulomb energy W_C.

We assume that the surface energy is proportional to the area of the surface. While the bulk energy W_b does not depend on the nuclear shape, the surface energy W_s does depend on it as the surface area does. We write the surface energy of a cell as

$$W_S = \sigma(n,^{in}, x, n^{out}) g(u, shape) a^2, \tag{3.3}$$

where $\sigma(n,^{in}, x, n^{out})$ is the surface tension and $g(u, shape)$ is the relative surface area which depends on the nuclear shape. The function $g(u, shape)$ is calculated as

$$g\left(u, \text{sphere}\right) = \left(6\sqrt{\pi}\, u\right)^{2/3}, \tag{3.4a}$$

$$g\left(u, \text{cylinder}\right) = \sqrt{4\pi\, u}\,, \tag{3.4b}$$

and

$$g\left(u, \text{slab}\right) = 2\,. \tag{3.4c}$$

The expressions of $g(u, shape)$ for the cylindrical hole and spherical hole nuclei can be obtained by replacing u by $1-u$ in Eqs. (3.4a) and (3.4c), respectively:

$$g\left(u, \text{cylindrical hole}\right) = \sqrt{4\pi\left(1-u\right)}\,, \tag{3.4d}$$

$$g\left(u, \text{spherical hole}\right) = \left[6\sqrt{\pi}\left(1-u\right)\right]^{2/3}. \tag{3.4e}$$

Fig. 3-4 shows the relative surface area $g(u, shape)$ for various shapes. From Eqs. (3.4a)-(3.4e), this figure is symmetric about the line u=1/2.

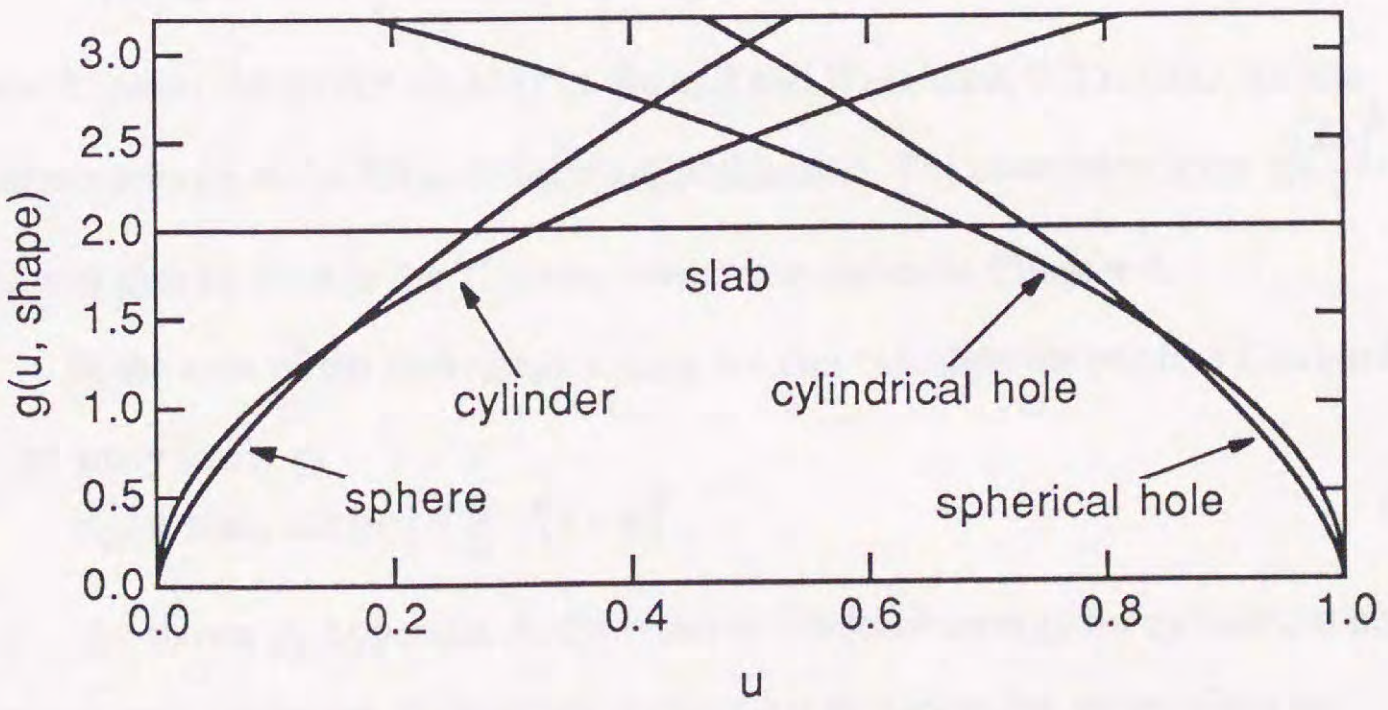

Fig. 3-4. Relative surface area $g(u, shape)$.

We write the Coulomb energy as

$$W_C = \left(e\, n^{in}\, x\right)^2 w_{C1}\left(u, \mathit{shape}, \mathit{lattice}\right) a^5 . \tag{3.5}$$

Where, e is the elementary charge and $w_{C1}\left(u, \mathit{shape}, \mathit{lattice}\right)$ is the relative Coulomb energy which depends on u as well as on the nuclear shape and lattice type. Table 3-1 lists the maximum u values together with the maximum nuclear radii R that are geometrically realizable for various lattice types. Expressions of $w_{C1}\left(u, \mathit{shape}, \mathit{lattice}\right)$ for spherical and cylindrical nuclei are given in forms of series in Appendix A.

With detailed numerical calculations we have found that the relative Coulomb energies for sphere and cylinder with various lattice types can be written in a very good approximation as

$$w_{C1}\left(u, \mathit{shape}, \text{lattice}\right) = w_{C1}\left(u, \mathit{shape}, \text{WS}\right) + c_l u^2 , \tag{3.6}$$

where $w_{C1}\left(u, \mathit{shape}, \text{WS}\right)$ is the relative Coulomb energy in the Wigner-Seitz approximation. The relative Coulomb energies in the Wigner-Seitz-cell approximation are given by

$$w_{C1}\left(u, \text{sphere, WS}\right) = \frac{3}{5}\left(\frac{\pi}{6}\right)^{1/3}\left(2u^{5/3} - 3u^2 + u^{8/3}\right), \tag{3.7}$$

$$w_{C1}\left(u, \text{cylinder, WS}\right) = \frac{u^2}{2}\left(u - 1 - \log u\right). \tag{3.8}$$

The values of c_l for various lattice types are given in Table 3-2. From Eqs. (3.5) and (3.6), the Coulomb energy can be written as

$$W_C\left(\mathit{shape}, \mathit{lattice}\right) = W_C\left(\text{shape, WS}\right) + c_l \frac{\left(Ze\right)^2}{a} , \tag{3.9}$$

where Z means the proton number in the cell and $W_C(\mathit{shape}, \text{WS})$ stands for the Coulomb energy in the Wigner-Seitz approximation. The correction term $c_l \frac{\left(Ze\right)^2}{a}$ in Eq. (3.9) will also be used in the Thomas-Fermi calculation in Chapter 4.

In the case of the slab-shape nuclei, we can calculate the relative Coulomb energy analytically as

$$w_{C1}\left(u, \text{slab, simple}\right) = \frac{\pi}{6} u^2\left(1 - u\right)^2 . \tag{3.10}$$

As shown in Appendix A, the relative Coulomb energy for cylindrical hole and spherical hole nuclei are obtained by replacing u by $1-u$ in the expressions for cylindrical and spherical hole nuclei, respectively:

$$w_{C1}\left(u, \text{cylindrical hole}, \textit{lattice}\right) = w_{C1}\left(u, \text{cylinder}, \textit{lattice}\right), \tag{3.11}$$

$$w_{C1}\left(u, \text{spherical hole}, \textit{lattice}\right) = w_{C1}\left(u, \text{sphere}, \textit{lattice}\right). \tag{3.12}$$

Fig. 3-4 shows $w_{C1}\left(u, \textit{shape}, \textit{lattice}\right)$ for sphere (top box), cylinder (middle box) and all shapes (bottom box). We see from the top and middle boxes that bcc for spherical nuclei and hex for cylindrical nuclei give the lowest energies.

Table 3-1

Values of maximum u and maximum nuclear radii R that are allowed geometrically.

	sphere			cylinder		slab
	bcc	fcc	sc	hex	ss	simple
u_{max}	$\frac{\sqrt{3}\pi}{8}$	$\frac{\pi}{3\sqrt{2}}$	$\frac{\pi}{6}$	$\frac{\pi}{2\sqrt{3}}$	$\frac{\pi}{4}$	1/2
R_{max}/a	$\frac{\sqrt{3}\sqrt[3]{2}}{4}$	$2^{-5/6}$	1/2	$\frac{1}{\sqrt{2\sqrt{3}}}$	1/2	1/2

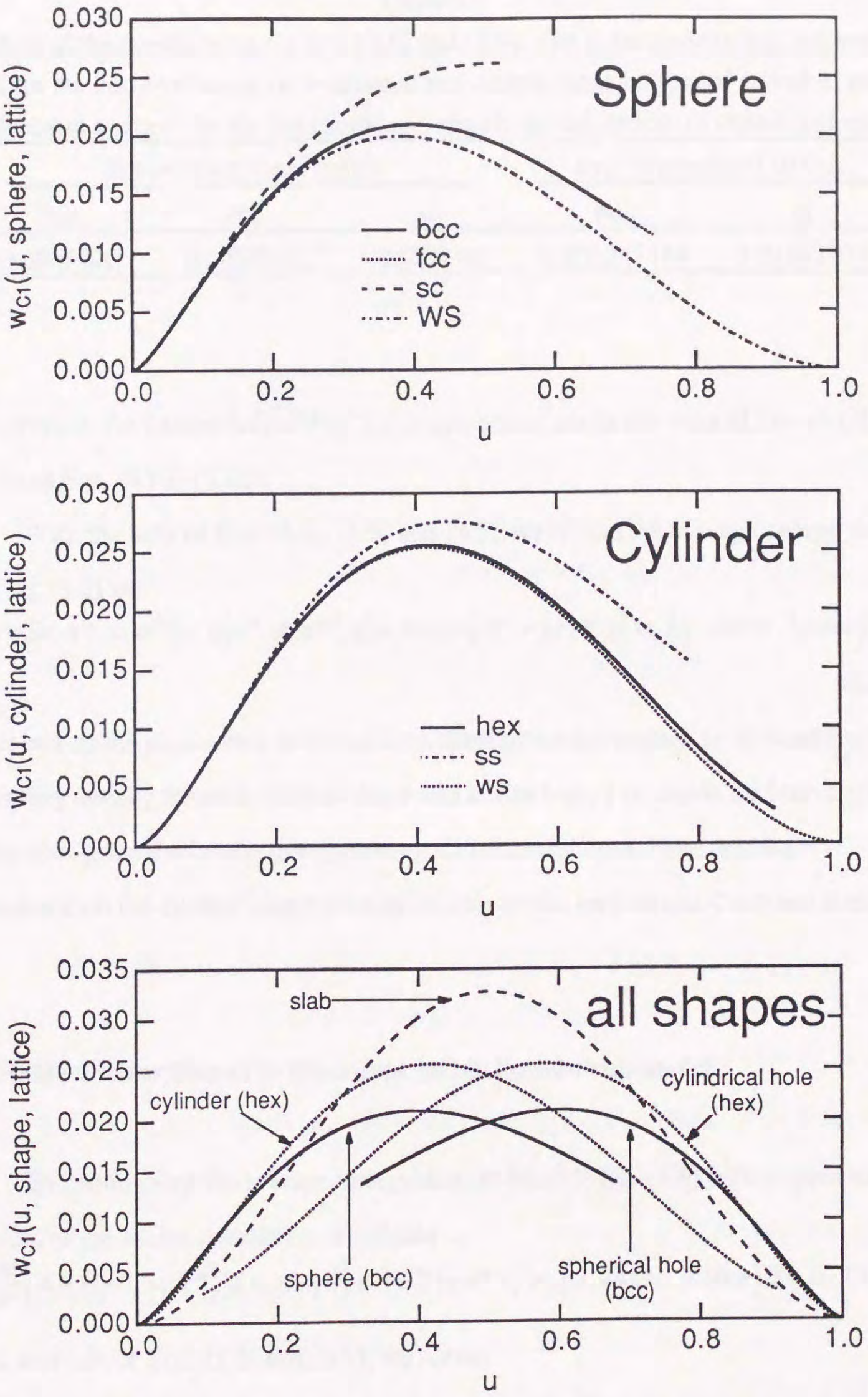

Fig. 3-5. Relative Coulomb energy $w_{C1}(u, shape, lattice)$. The abbreviations of lattice types are given in text. In the top box, the lines for bcc and fcc lattices are hardly distinguishable.

Table 3-2

Values of the coefficient c_l in Eqs. (3.6) and (3.9). The abbreviations bcc, fcc and sc stand for the body-centered, face-centered and simple cubic lattices of spherical nuclei, and hex and ss stand for the hexagonal and simple square lattices of cylindrical nuclei.

three-dimensional lattice			two-dimensional lattice	
bcc	fcc	sc	hex	ss
0.0065620	0.0066517	0.032144	0.001247514	0.01183202

The curves in the bottom box of Fig. 3-5 is symmetric about the vertical line u=1/2 as seen from Eqs. (3.10)-(3.12).

With the help of Eqs. (3.2), (3.3) and (3.5), we obtain the average energy density from Eq. (3.1) as

$$\frac{W}{a^3} = w_b\left(u, n^{in}, x, n^{out}\right) + \sigma\left(n^{in}, x, n^{out}\right) g\left(u, shape\right) a^{-1} + \left(e\, n^{in}\, x\right)^2 w_{C1}\left(u, shape, lattice\right) a^2 \,. \tag{3.13}$$

The values of the parameters in the nucleon distribution are chosen so as to minimize this energy density for each nuclear shape and lattice type. The stable nuclear shape is the one that gives the lowest energy among all nuclear shapes. Note that the dependence on the nuclear shape is included only in the surface and Coulomb energies.

3.4. Stable nuclear shapes in the compressible liquid-drop model

By minimizing the average energy density W/a^3 in Eq. (3.6) with respect to variation of the lattice constant a, we obtain

$$\frac{\partial}{\partial a}\left(\frac{W}{a^3}\right) = -\sigma\left(n^{in}, x, n^{out}\right) g\left(u, shape\right) a^{-2} + 2\left(e\, n^{in}\, x\right)^2 w_{C1}\left(u, shape, lattice\right) a = 0 \,. \tag{3.14}$$

Then, with use of Eqs. (3.3) and (3.5), we obtain

$$W_S = 2W_C. \tag{3.15}$$

This is an expression useful for determining the stable nuclear shape. Since the dependence of the average energy density on the nuclear shape is present only in the

surface and Coulomb energies, the stable nuclear shape is determined by minimizing the sum of them. We can eliminate a from Eq. (3.14) using Eqs.(3.3) and (3.5):

$$a = \left[\frac{\sigma\left(n^{\text{in}}, x, n^{\text{out}}\right) g\left(u, shape\right)}{2\left(en^{\text{in}}x\right)^2 w_{\text{Cl}}\left(u, shape, lattice\right)} \right]^{1/3} . \tag{3.16}$$

Then, Eq. (3.13) can be written as

$$\frac{W}{a^3} = w_b\left(u, n^{in}, x, n^{out}\right) + \frac{3}{2}\sqrt[3]{2}\left[en^{in}x\sigma\left(n^{in}, x, n^{out}\right)\right]^{2/3} g\left(u, shape\right)^{2/3} w_{\text{Cl}}\left(u, shape, lattice\right)^{1/3} . \tag{3.17}$$

Now we can determine the stable nuclear shape and lattice type by minimizing the last term of Eq. (3.17). We see from this equation that the stable nuclear shape and lattice type are determined uniquely for a given u (volume fraction occupied by the nucleus in a cell). Namely, the stable shape and lattice type are those that minimize the geometric factor defined as

$$G\left(u, shape, lattice\right) = g\left(u, shape\right)^{2/3} w_{\text{Cl}}\left(u, shape, lattice\right)^{1/3} . \tag{3.18}$$

The term "geometric factor" was used by Cooperstein and Baron [?] although the definition (3.18) is slightly different from and more general than theirs. The result is shown in Fig. 3-6. The curves in this figure are symmetric about the vertical line u=1/2 as are in Figs. 3-4 and 3-5. Fig. 3-6 indicates that, with increase of u, the nuclear shape changes successively from sphere to cylinder, slab, cylindrical hole and spherical hole. The limiting value u=1 corresponds to uniform matter while $u \approx 0$ corresponds to the situation in our daily life in which the nuclei occupy only a very small portion of the whole space. The above conclusion obtained from Fig. 3-6 may look queer at first glance, but it is consistent with the fact that the stable nucleus in our daily life (at $u \approx 0$) is spherical. Note that the shape change occurs at extremely large u values compared with the environment realizable in the laboratory.

Table 3-3 summerizes the u values at which the stable shape changes. In addition to the values in which the lattice is taken into account, the values obtained in the Wigner-Seitz approximation are also listed for comparison. This table and Fig. 3-5 shows that the Wigner-Seitz approximation is relatively good in the ranges of u in which the stable nuclear shape changes. From Figs. 3-4, 3-5 (bottom box) and 3-6, we

see that the relative surface area mainly determines the stable nuclear shape as expected from Eqs. (3.15) and (3.18). Therefore these shape change can be regarded as a geomerical property of the nuclei. It is also interesting to note that the approximate ratio of the linear nuclear size to the cell size, which is given by $u^{1/3}$ for sphere, $u^{1/2}$ for cylinder and u for slab, is roughly 1/2 when the shape is stable with an exception that a much smaller value is allowed for spherical nuclei.

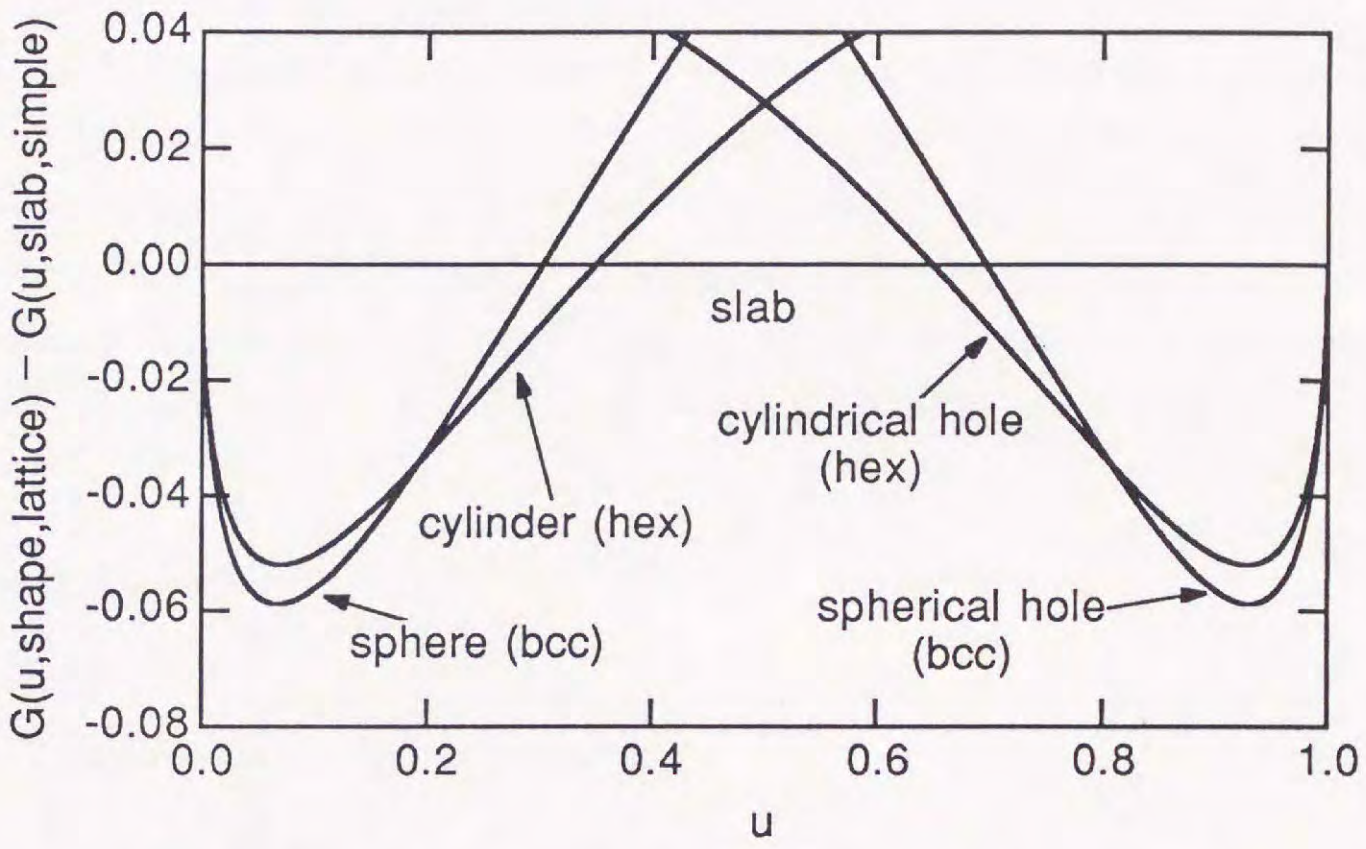

Fig. 3-6. Geometric factor $G(u, shape, lattice)$ relative to that of slab.

Table 3-3

Values of u at which the stable nuclear shape changes. The abbreviations SP, C, SL, CH, and SPH stand for sphere, cylinder, slab, cylindrical hole and spherical hole. In the upper column (bcc, hex), the transition u values are calculated with the bcc laittce for spherical (hole) nuclei and the hexagonal lattice for cylindrical (hole) nuclei. In the lower column, the u values are calculated in the Wigner-Seitz approximation.

lattice	SP → CY	C → SL	SL → CH	CH → SPH
bcc, hex	0.19252	0.35012	0.64988	0.80748
WS	0.21525	0.35499	0.64501	0.78475

In this section, we have described the condition for the stable nuclear shape in a simpler form than that of ref. [4]. Although we have followed the procedure of ref. [1] in deriving Eq. (3.17) from Eq.(3.14), the above condition is essentially the same as the one in Ref. [4].

Chapter 4

Thomas-Fermi calculation of non-spherical nuclei

The compressible liquid-drop model predicts that non-spherical nuclei become stable if the nucleus occupies a certain fraction of volume in a cell. However, it does not tell whether these values of volume fraction u are attainable in the neutron star crust. Therefore, the conclusion of Chapter 3 does not necessarily guarantee the existence of non-spherical nuclei in reality. Although the liquid-drop model provides us with intuitive physical pictures, it lacks in describing the diffuseness of the surface which is an important property of normal nuclei. Moreover, the geometrical argument in Chapter 3 does not tell the matter densities where the non-spherical nuclei exist. Therefore in this chapter we perform, with an appropriate nuclear interaction, the Thomas-Fermi calculation by taking the surface diffuseness into account.

4.1. Energy of matter

We write the energy per cell as

$$W=W_N+W_e+W_C, \tag{4.1}$$

where W_N, W_e and W_C are the nuclear energy, the electron (kinetic) energy, and the Coulomb energy, respectively.

The nuclear energy is assumed to be written in terms of the energy density functional ε as

$$W_N = \int_{cell} \left[\varepsilon(n_n(\boldsymbol{r}), n_p(\boldsymbol{r}), \nabla n_n(\boldsymbol{r}), \nabla n_p(\boldsymbol{r})) + m_n n_n + m_p n_p \right] d\boldsymbol{r} . \tag{4.2}$$

Here, $n_n(\boldsymbol{r})$ ($n_p(\boldsymbol{r})$) and m_n (m_p) are, respectively, the local number density and the mass of the neutron (proton). The nuclear energy is expected to depend little on the lattice type because the nuclear forces are of short range. We calculate W_N using the Wigner-Seitz cell:

$$W_N = \int_{\text{WS cell}} \left[\varepsilon(n_n(\boldsymbol{r}), n_p(\boldsymbol{r}), \nabla n_n(\boldsymbol{r}), \nabla n_p(\boldsymbol{r})) + m_n n_n + m_p n_p \right] d\boldsymbol{r} \,. \tag{4.3}$$

This nuclear energy is discussed in more detail in the next section.

Electrons interact only with charged particles through the Coulomb forces. Since the electron Fermi energy is much higher than the Coulomb energy, we approximate W_e to the energy of the uniform relativistic Fermi gas:

$$\frac{W_e}{a^3} = \frac{{m_e}^4 c^5}{8\pi^2 \hbar^3} \left\{ x_e \left(2{x_e}^2+1\right)\left({x_e}^2+1\right)^{1/2} - \ln\left[x_e + \left({x_e}^2+1\right)^{1/2} \right] \right\} \,, \tag{4.4}$$

with

$$x_e = \left(3\pi^2\right)^{1/3} \left(\hbar / m_e c\right) {n_e}^{1/3} \,, \tag{4.5}$$

where m_e is the electron mass and c is the velocity of light. The electron number density n_e is determined by the charge neutrality condition.

In the approximation that the electron distribution is uniform, the Coulomb energy per cell, W_C, is given by

$$W_C = \frac{1}{2} \int_{\text{cell}} e \left[n_p(\boldsymbol{r}) - n_e \right] \phi(\boldsymbol{r}) d\boldsymbol{r} \,, \tag{4.6}$$

where $\phi(\boldsymbol{r})$ stands for the electrostatic potential obtained as the solution of Poisson's equation:

$$\nabla^2 \phi(\boldsymbol{r}) = 4\pi e \left[n_p(\boldsymbol{r}) - n_e \right] . \tag{4.7}$$

Because of the long range nature of the Coulomb interactions, the Coulomb energy depends on both the nuclear shape and the lattice type. The Coulomb energy is very difficult to calculate exactly except for the slab-shape nuclei unless the nuclei have sharp surfaces as in Chapter 3. The Wigner-Seitz cell approximation, in which the Coulomb interactions with the charged particles in the other cells are neglected, can not treat the dependence on the lattice type. The difference between the exact value and the result of the Wigner-Seitz approximation is expected to be relatively insensitive to the diffuseness of the nuclear surface. Therefore, we write the Coulomb energy as

$$W_{\mathrm{C}} = \frac{1}{2}\int_{\mathrm{WS\ cell}} e\left[n_{\mathrm{p}}(\boldsymbol{r}) - n_{\mathrm{e}}\right]\phi_{\mathrm{WS}}(\boldsymbol{r})d\boldsymbol{r} + \Delta W_l\,, \tag{4.8}$$

where $\phi_{\mathrm{WS}}(\boldsymbol{r})$ is the electrostatic potential calculated in the Wigner-Seitz approximation. We use the correction term ΔW_l in Eq. (3.9) derived from the liquid drop model:

$$\Delta W_l = c_l \frac{(Ze)^2}{a} \tag{4.9}$$

with Z being the proton number per cell. The values of the coefficient c_l are listed in Table 3-2. As for the hole nuclei, we can also use Eq. (4.9) by replacing Z by Z', which is the proton number necessary to fill the hole in the proton distribution.

4.2. Energy density functional ε

We assume the energy density functional ε to be a function of the local neutron and proton number densities, $n_{\mathrm{n}}(\boldsymbol{r})$ and $n_{\mathrm{p}}(\boldsymbol{r})$, and their gradients. We divide the functional ε into two parts as

$$\varepsilon\left(n_{\mathrm{n}}, n_{\mathrm{p}}, \nabla n_{\mathrm{n}}, \nabla n_{\mathrm{p}}\right) = \varepsilon_0\left(n_{\mathrm{n}}, n_{\mathrm{p}}\right) + \varepsilon_g\left(n_{\mathrm{n}}, n_{\mathrm{p}}, \nabla n_{\mathrm{n}}, \nabla n_{\mathrm{p}}\right). \tag{4.10}$$

The first term ε_0 is the energy density of uniform nuclear matter, and the second term ε_g gives the contribution from the density inhomogeneity.

By using the potential energy density of symmetric nuclear matter $\upsilon_{\mathrm{s}}(n)$ and that of pure neutron matter $\upsilon_{\mathrm{n}}(n)$, we write ε_0 as

$$\varepsilon_0\left(n_{\mathrm{n}}, n_{\mathrm{p}}\right) = \frac{3}{5}\left(3\pi^2\right)^{2/3}\left(\frac{\hbar^2}{2m_{\mathrm{n}}} n_{\mathrm{n}}^{5/3} + \frac{\hbar^2}{2m_{\mathrm{p}}} n_{\mathrm{p}}^{5/3}\right) + \left[1 - \left(1-2x\right)^2\right]\upsilon_{\mathrm{s}}(n) + \left(1-2x\right)^2 \upsilon_{\mathrm{n}}(n), \tag{4.11}$$

where $n = n_{\mathrm{n}} + n_{\mathrm{p}}$ and $x = n_{\mathrm{p}} / n$. We adopt the functional form of the potential energy density proposed by Bludman and Dover [21] for $\upsilon_{\mathrm{s}}(n)$ and $\upsilon_{\mathrm{n}}(n)$:

$$v_s(n) = a_1 n^2 + \frac{a_2 n^3}{1 + a_3 n}, \tag{4.12}$$

$$v_n(n) = b_1 n^2 + \frac{b_2 n^3}{1 + b_3 n}. \tag{4.13}$$

With reasonable parameter values the denominators in Eqs. (4.12) and (4.13) ensure that the sound velocity does not exceed the speed of light and the equation of state (EOS) always satisfies the causality.

As for the inhomogeneity term ε_g, we use the following expression:

$$\varepsilon_g\left(n_n, n_p, \nabla n_n, \nabla n_p\right) = \frac{\alpha}{36}\left(\frac{\hbar^2}{2m_n}\frac{\left|\nabla n_n\right|^2}{n_n} + \frac{\hbar^2}{2m_p}\frac{\left|\nabla n_p\right|^2}{n_p}\right) + F_0\left[\left|\nabla\left(n_n + n_p\right)\right|^2 - \beta\left|\nabla\left(n_n - n_p\right)\right|^2\right]. \tag{4.14}$$

The first term on the right hand side of Eq. (4.14) is the kinetic energy correction, which is often referred to as the Weizsäcker term. The value of the coefficient α originally derived by Weizsäcker [22] was 9, while the correct semi-classical value [23] is 1. The last term in Eq. (4.14) including two parameters F_0 and β represents the finite-range effect of nuclear forces.

The functional ε_g is the most important nuclear term in determining the shape of the nucleus. If we put

$$W_g = \int_{\text{cell}} \varepsilon_g(n_n(\boldsymbol{r}), n_p(\boldsymbol{r}), \nabla n_n(\boldsymbol{r}), \nabla n_p(\boldsymbol{r}))\, d\boldsymbol{r}, \tag{4.15}$$

then the condition to minimize the average energy density W/a^3 with respect to variation of the lattice constant a is simply written as

$$W_g = W_C. \tag{4.16}$$

This equation, used by Arponen [9], holds for general forms of $n_n(\boldsymbol{r})$ and $n_p(\boldsymbol{r})$, and corresponds to the condition in the liquid-drop model that the surface energy is twice as much as the Coulomb energy.

4.3. Parametrization of nucleon distributions

In order to avoid complexities due to boundary conditions, we assume the following nucleon distributions $n_i(r)$ (i=n, p), where r represents the distance from the center (central axis for cylinder, and central plane for slab) of the nucleus (or hole):

$$n_i(r) = \begin{cases} \left(n_i^{in} - n_i^{out}\right)\left[1 - \left(\frac{r}{R_i}\right)^{t_i}\right]^k + n_i^{out}, & r < R_i \\ n_i^{out}. & r \geq R_i \end{cases} \tag{4.17}$$

Fig.1 shows an example of the parametrized nucleon distributions. The parameter R_i represents the (finite) boundary of the nucleus and t_i determines the relative surface thickness. In the limit $t_i \to \infty$, Eq. (4.17) gives a sharp surface at $r = R_i$. Eq. (4.17) coincides with the form used by Arponen [9] if k=2, R_n=R_p and t_n=t_p. In this paper, we put k=3, because ε_g diverges at $r = R_i$ if k=2 and α=1. In the case of the spherical, cylindrical or slab-shape nucleus, n_p^{out} is taken to be zero. As for the hole nucleus, n_p^{in}=0 instead.

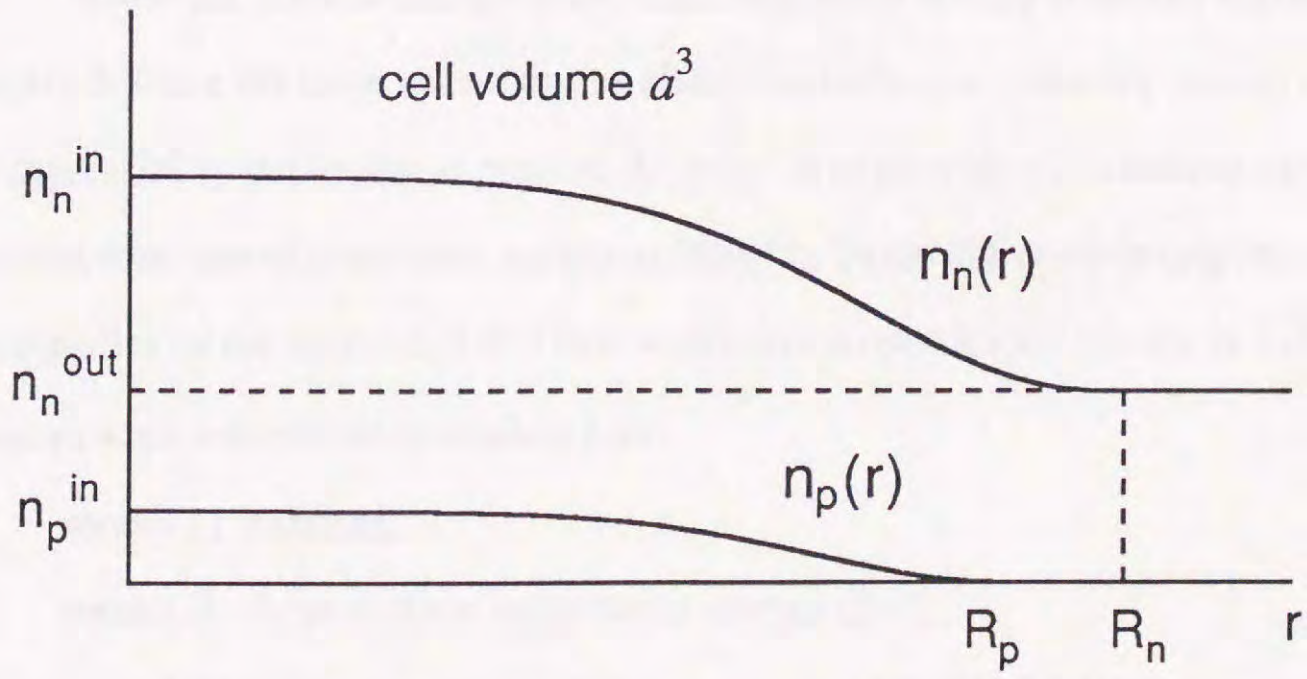

Fig. 4-1. Parametrization of nucleon distributions.

To describe the cell size and the nucleon distributions in the cell, we have eight parameters, a, n_n^{in}, n_n^{out}, n_p^{in} (or n_p^{out}), R_n, R_p, t_n and t_p. When the average nucleon number density in a cell, n_b, is fixed, seven parameters among them are independent. In this paper, we minimize the average energy density W/a^3 for a given n_b with respect to variation of these parameters. We can further eliminate one parameter by using Eq. (4.16), but we use it simply to check the degree of convergence of the minimization.

4.4. EOS of nuclear matter and normal nuclei

We can calculate the masses of normal nuclei by taking the limit $a \to \infty$. Values of the nine parameters in the energy density functional ε are determined so as to be consistent with

(a) experimental masses and radii of normal nuclei,

(b) EOS of nuclear matter obtained from many-body calculations up to a density a few times as high as the normal nuclear density.

Usually the latter condition is not necessary to describe the properties of normal nuclei. However, we do need the condition (b) because the matter in the neutron-star inner crust is extremely neutron rich. Details of this procedure are described in Appendix B.

While the surface energy is the most important energy from the argument in Chapter 3, there are large uncertainties about the surface asymmetry energy and incompressiblity parameter at present. In order to cope with this situation, we have obtained four sets of parameter values as listed in Table 4-1 considering the uncertainties of the functional ε. Their saturation properties are shown in Table 4-2. These sets are referred to as models I-IV:

model I : standard,

model II : large surface asymmetry energy (β=1),

model III : high incompressibility parameter (K=293 MeV),

model IV : no kinetic term in ε_g (α=0).

We consider model IV because in many Thomas-Fermi calculations, the explicit kinetic energy term in ε_g (α=0) was dropped and the kinetic energy was assumed to be represented by a term similar to the last terms of Eq. (4.14).

Table 4-1

Parameter values in the energy density functional ε. The difinition of ξ is given in Appendix B.

	model			
	I	II	III	IV
a_1(MeV·fm^3)	−473.37	−473.43	−429.69	−475.62
a_2(MeV·fm^6)	2327.7	2242.2	1497.4	2366.6
a_3(fm^3)	3.6667	3.2759	1.6487	3.7347
b_1(MeV·fm^3)	−205.46	−191.47	−205.48	−202.69
b_2(MeV·fm^6)	635.72	592.43	635.81	627.15
b_3(fm^3)	1.5863	1.5863	1.5863	1.5863
ξ	0.9788	0.9121	0.9789	0.9656
α(MeV/fm)	1	1	1	0
F_0(MeV•fm^5)	47.399	49.522	47.294	68.650
β	0	1	0	0

Table 4-2

Saturation properties of nuclear matter. n_0 : nucleon number density, E_0 : energy per nucleon, S_0 : symmetry energy coefficient, K : incompressibility parameter.

	model			
	I	II	III	IV
n_0 (fm^{-3})	0.159	0.152	0.158	0.158
E_0 (MeV)	−16.1	−16.0	−16.3	−16.0
S_0 (MeV)	31.1	31.9	31.4	31.3
K (MeV)	222	235	293	221

As shown in Fig. 4-2, all these four models give similar EOS to those by Friedman and Pandharipande [12] for both pure neutron matter and symmetric nuclear matter. The differences among these models, especially at densities below the nuclear density, are not very large compared with the differences among phenomenological Skyrme intercations by various authors [17,,24,25]. Models I and IV give nearly the same EOS for both matters. Model II gives slightly higher energies of pure neutron matter than model I. As shown in Fig. 4-3, the proton chemical potentials of models I and III in pure neutron matter are slightly different, although the energies per nucleon of that matter are almost the same. It is very interesting that all the phenomenological EOS (models I-IV, Ska, SKM, and RBP) in Fig. 4-2 give the almost same saturation density and energy, and the symmetry energy at the saturation density. However, the gradient of the EOS of neutron matter and the curvature at the saturation density are different. These differences reflect the present uncertainties about the surface symmetry energy and the incompressibility parameter.

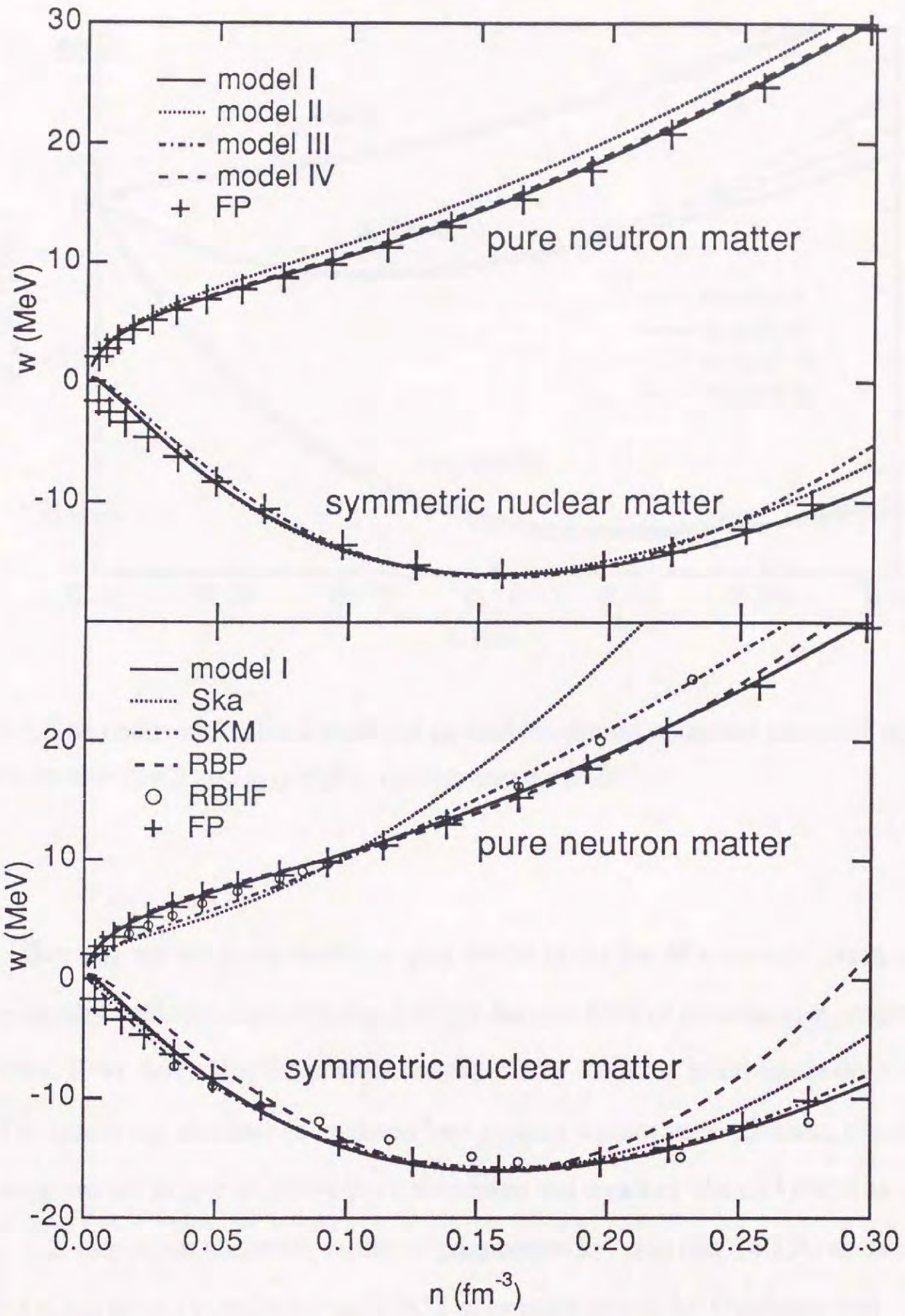

Fig. 4-2. EOS of neutron matter and symmetric nuclear matter. Shown is the energy per nucleon measured from the nucleon mass. In the upper box, the present four models are shown together with the EOS by Friedman and Pandharipande (FP) [12]. The results of models I and IV are indistinguishable. In the lower box, model I is compared with three EOS's of Skyrme interactions; Ska, SKM and RBP indicate the results with the parameter sets by Köhler [24], Krivine et *al.* [25] and Ravenhall et *al.* [17], respectively. Also shown is the EOS obtained from the relativistic Brueckner Hartree-Fock calculation (RBHF) [26].

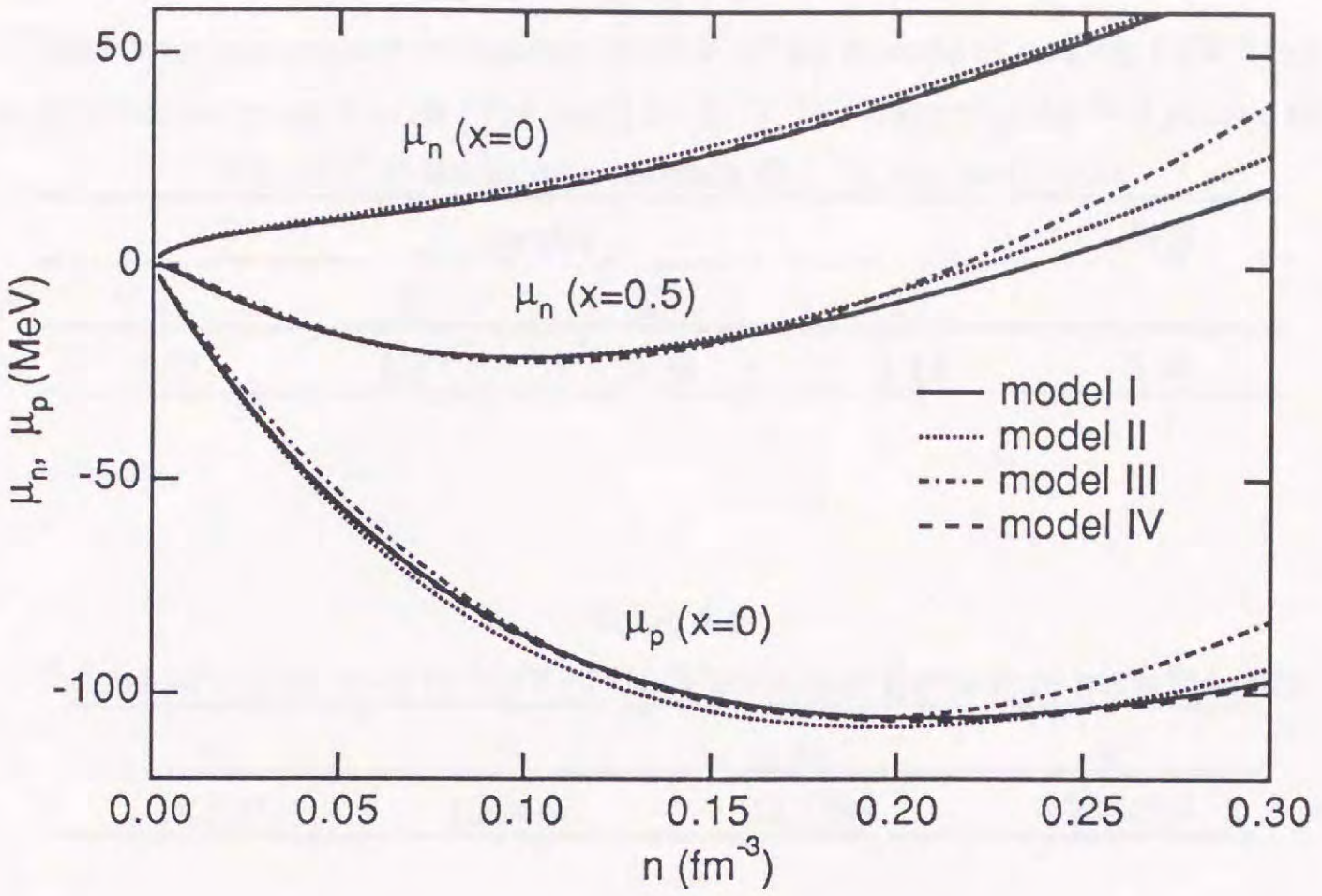

Fig. 4-3. The neutron chemical potential μ_n and the proton chemical potential μ_p in pure neutron matter (x=0) and symmetric nuclear matter (x=0.5).

Because we are going to investigate nuclei in the sea of a neutron gas at the matter density below nuclear density, the low density EOS of pure neutron matter is important. If we determine the energy density ε only from the information on normal nuclei in which the numbers of neutrons and protons are not very different, the energies of neutron matter at low densities tend to become too small as Ska and SKM as shown in Fig. 4-2. Hence we constrain values of parameters in $\upsilon_n(n)$ (Eq. (4.13)) so as to obtain a good fit to a commonly used EOS of neutron matter by Freedman and Pandharipande [12]. As a result, we have only one free parameter ξ in $\upsilon_n(n)$, which corresponds to the symmetry energy of nuclear matter (see also Eq. (B.2)).

Table 4-4 shows the root-mean-square deviations of the masses of models I-IV from experimental mass data of 1657 nuclides [27]. For comparison, we also show those of the Weizsäcker-Bethe type formula fitted to the same data; the formula used here is

Table 4-4

The root-mean-square deviations in MeV of the masses of models I-IV from experimental mass data of 1657 nuclides [27]. The abbreviation WB means the Weizsäcker-Bethe type formula fitted to the same data

model				WB
I	II	III	IV	
3.47	3.37	4.31	3.18	3.48

Table 4-5

Values of coefficients in MeV of the Weizsäcker-Bethe type mass formula

a_v	a_s	a_I	a_C
-15.5391	16.9666	22.7739	0.703893

$$M_{WB}(Z,N) = m_n N + (m_p + m_e)Z + a_v A + a_s A^{2/3} + a_I \frac{(N-Z)^2}{A} + a_C \frac{Z^2}{A^{1/3}}, \quad (4.18)$$

with the parameter values listed in Table 4-5. The masses given by the four models are reasonable in the absence of shell terms. In Fig. 4-4, we show the charge distributions in ^{90}Zr and ^{208}Pb calculated from our proton distributions $n_p(r)$ and the proton charge form factor [28]

$$\rho(r) = \left(\frac{1}{\sqrt{\pi}\, a_p}\right)^3 \exp\left[-(r/a_p)^2\right], \qquad a_p = 0.65 \text{ fm}. \quad (4.19)$$

Our models are in fair agreement with experiment not only for the radius but also for the surface diffuseness, although we did not fit the surface diffuseness in determining the parameter values in ε.

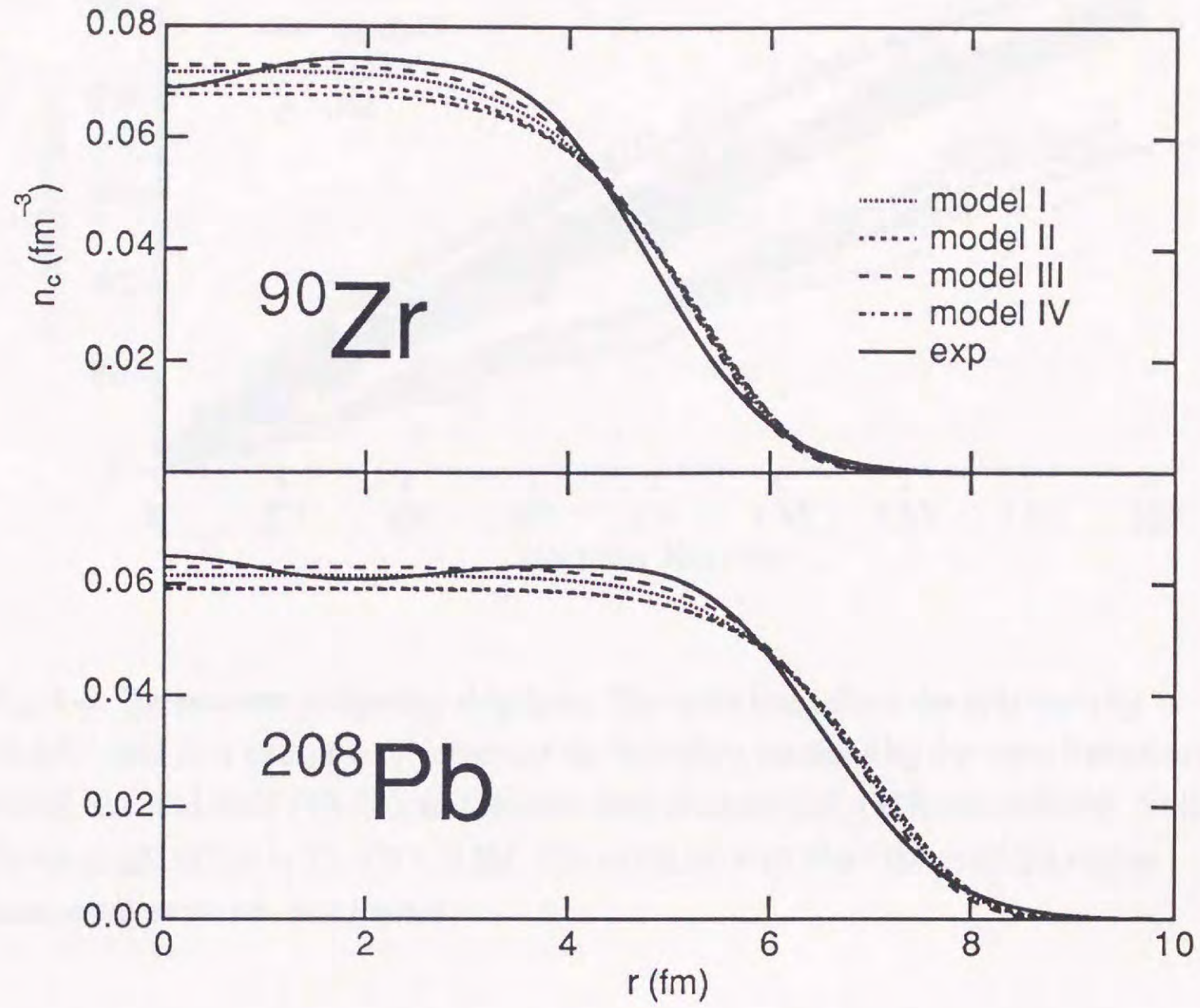

Fig. 4-5. Charge distributions in ^{90}Zr and ^{208}Pb. Experimental data are taken from ref. [29]. In ^{208}Pb, the results of models II and IV are indistinguishable.

Fig. 4-6 shows the neutron and proton drip lines by model I together with those by two recent mass formulas [30,31] that give two extreme results. The drip lines by the other three models are almost the same as the ones by model I; the maximum difference among them is ±1 in N and Z values. The actual location of the neutron drip line, especially at large N, is quite uncertain at present, and the neutron drip lines by our models lie between those by the two extreme mass formulas.

As we have seen so far, all of our four models describe known nuclei fairly well ranging from stable nuclei to neutron-rich ones, and also reproduce approximately EOS of nuclear matter by Freidman and Pandharipande [12].

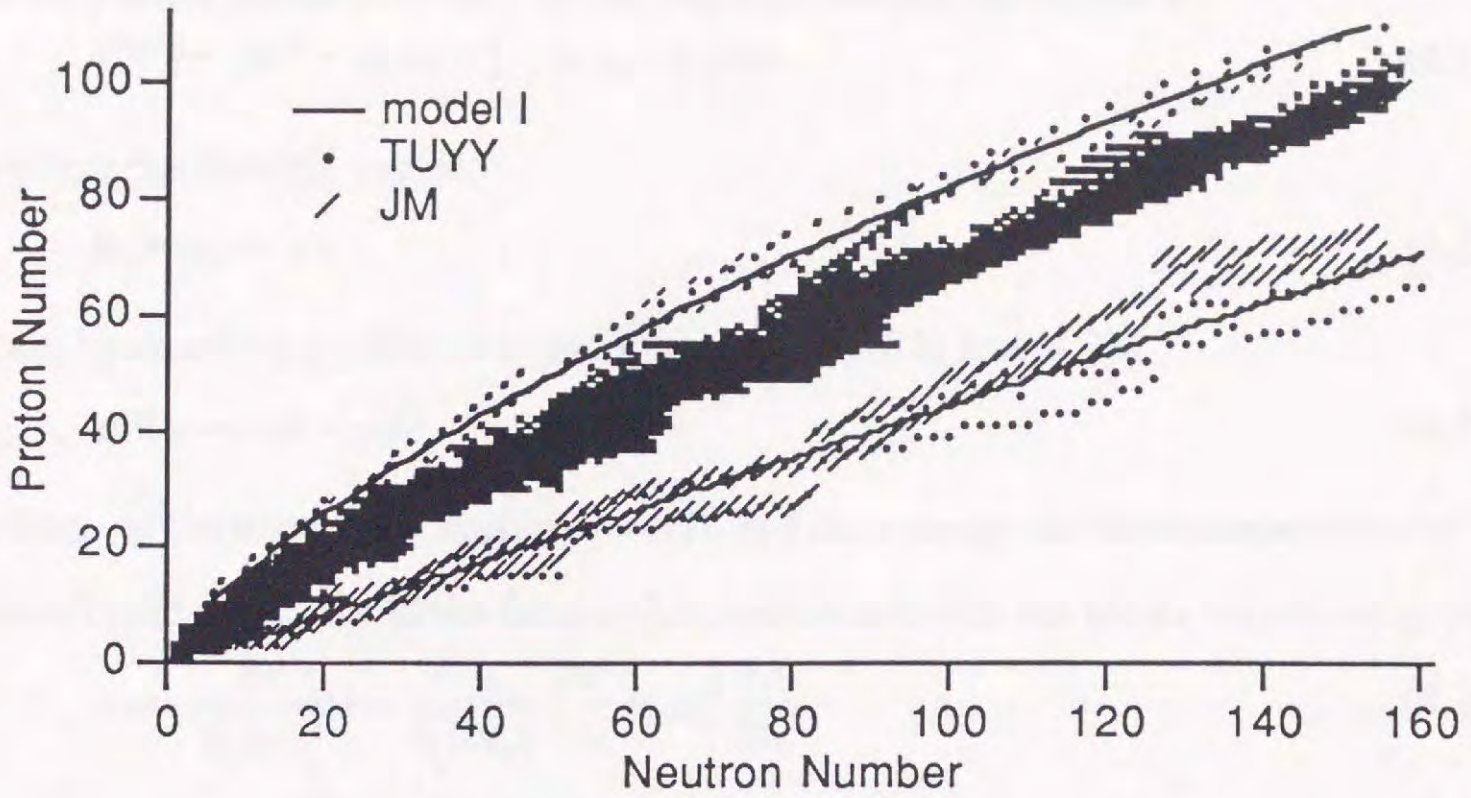

Fig. 4-6. The neutron and proton drip lines. The solid lines show the drip lines by Model I, and dots and slashes represent the boundary nuclides by the mass formulas of Tachibana et al. (TUYY) [30] and Jänecke and Masson (JM) [31], respectively. Notice the even-odd effect in TUYY and JM. The small squares show the nuclides whose masses are exprimentally known.

4.5. Pressure and chemical potential

In the full Thomas-Fermi calculation, the chemical potentials are Lagrange multipliers which corespond to the particle number consevations. However, in our treatment , they are functions of the point $\boldsymbol{r}$ in the cell because we parametrize nucleon distributions and assume a uniform distribution of electrons. In order to overcome this drawback, we start with the following general relationship.

We consider a unit cell with volume V, in which there are Z protons and N neutrons. Due to the charge neutrality condition, the number of electrons is Z. We write the energy per cell as W, and the chemical potential of the i-th species as μ_i with i=n,p,e. Then, we obtain

$$dW = -pdV + \mu_n dN + \left(\mu_p + \mu_e\right)dZ. \tag{4.20}$$

where p is the pressure. With $A=N+Z$, this equation can be written as

$$dW = -pdV + \mu_n dA + \left(\mu_p + \mu_e - \mu_n\right)dZ . \tag{4.21}$$

We treat the β-stable matter:

$$\mu_n = \mu_p + \mu_e . \tag{4.22}$$

Then, by rewriting μ_n as μ, we obatin from Eqs. (4.21) and (4.23)

$$dW = -pdV + \mu dA . \tag{4.23}$$

In terms of the energy per nucleon $w=W/A$ and the average nucleon number density $n_b=A/V$, the pressure and the (neutron) chemical potential are given, respectively, by

$$p = -\frac{\partial w}{\partial\left(1/n_b\right)} = -\frac{\partial n_b}{\partial\left(1/n_b\right)}\frac{\partial w}{\partial n_b} = n_b^{\,2}\frac{\partial w}{\partial n_b}, \tag{4.24}$$

and

$$\mu = \frac{\partial\left(w\, n_b\right)}{\partial n_b} = w + n_b\frac{\partial w}{\partial n_b} . \tag{4.25}$$

In this thesis, we calculate the pressure of matter by (4.24). We call μ in Eq. (4.26) as the (neutron) chemcal potential of matter. These quantities will be used to calculate the phase transitions in sects. 4.6 and 4.7.

4.6. Spherical nuclei in the neutron-star crust

At the densities in the outer crust, electrons are relativistic and nuclei are located so far away from each other that they are more or less spherical as the normal ones. Therefore, the nuclear energies can be approximated to those of the laboratory nuclei. Then, the necessary information is the masses of nuclides which can be measured by experiments or obtained from theoretical predictions. Baym, Pethick and Sutherland [14] determined the stable nuclides in early 70's and recently a more precise determination has been carried out by Haensel and Pichon [15] with the help of mass data which have become available in these twenty years. As shown in the following, our results obtained with models I-IV are not very different from each other and from those of previous studies with various methods except that no shell effects appear with

our semiclassical models. Table 4-6 lists the neutron drip point ρ_D, at which the neutron chemical potential becomes zero. The neutron drip point in our models is about 4×10^{11} g/cm^3, which is in good agreement with the previous studies with various methods [14,16-20,32]. Fig. 4-7 shows the variation in the stable nuclide at the matter densities below ρ_D on the *NZ* plane. At very low densities, the stable nuclide is ^{56}Fe whose binding energy per nucleon is the lowest. At denisties higher than 3×10^6 g/cm^3, the stable nuclide varies from ^{56}Fe because the electrons become relativistic and the Coulomb energy deviates from that of a normal nucleus due to the lattice contributions. As the density increases, the neutronization proceeds and on the average the stable nuclide changes from the left to the right in Fig. 4-7. We see from this figure that the neutron shell effects at N=50 and 82 are strong. Neutrons begin to drip out of the nucleus approximately when the stable nucleus reaches the neutron drip line of isolated nuclei. Although our semiclassical models are not capable of describing the shell effects, our results reproduce the transitions of the stable nuclide on the average.

Table 4-6
Neutron drip point ρ_D in 10^{11} g/cm^3 in models I-IV.

	model			
	I	II	III	IV
n_b (10^{-4} fm^{-3})	2 52	2.53	2.50	2.46
ρ (10^{11} g/cm^3)	4.21	4.22	4.18	4.10
Z	39	38	41	39
A	131	126	134	126

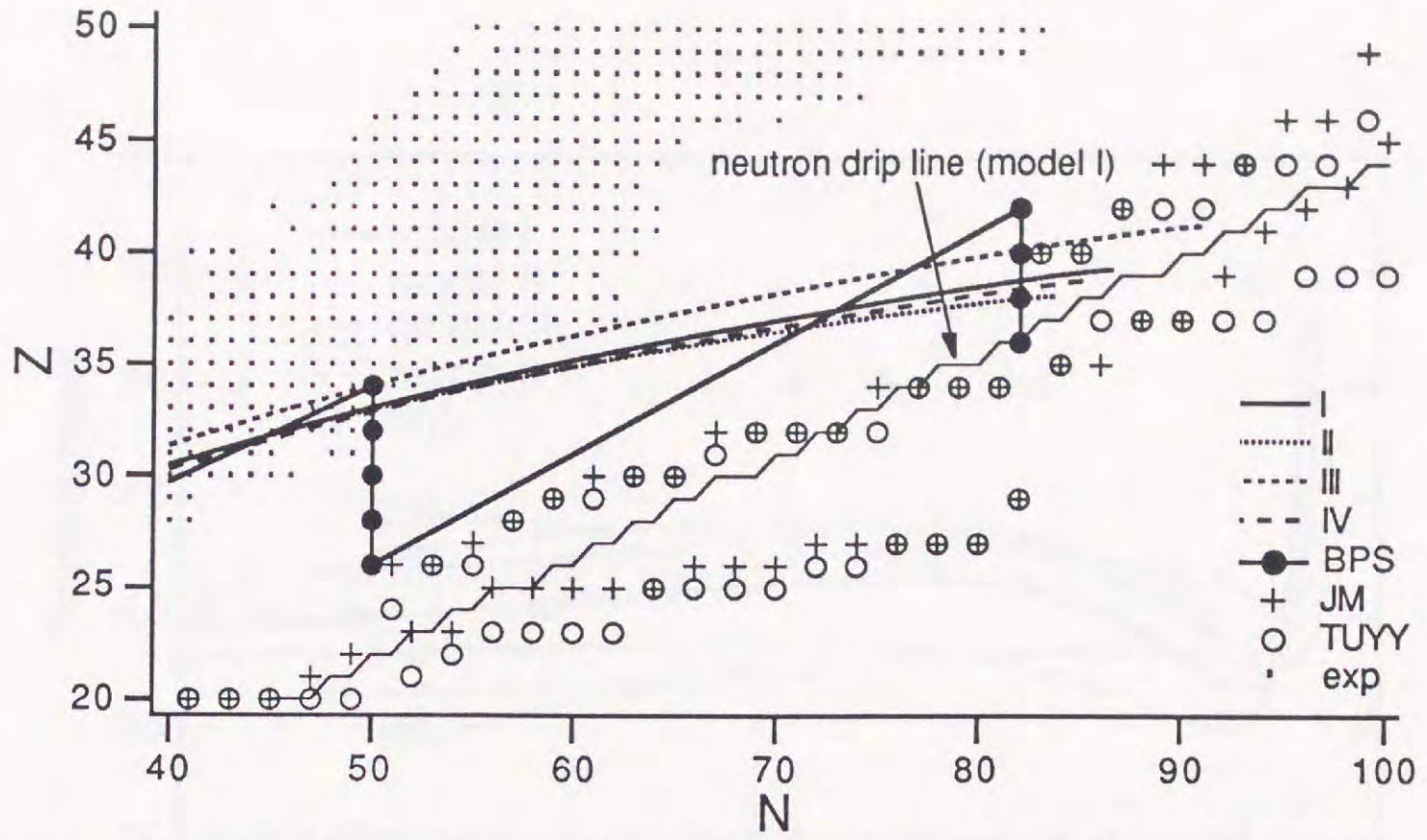

Fig. 4-7 Change of the stable nuclide at the matter densities below ρ_D. The stable nuclide moves from the left to the right on the average as the matter density increases. The results with our semiclassical models I-IV are continuous curves because we allow fractional values for *N* and *Z*. Note that the neutron shell effects cause some abrupt change of *N* and *Z* values in the result obtained with a mass formula by Baym, Pethick and Sutherland (BPS) [14]. For comparision, we also show the neutron drip line by model I and the boundary nuclides by mass formulas by Tachibana et al. (TUYY) [30] and Jäneke and Masson (JM) [31]. Dots means the nuclides whose masses are experimentally known [27].

In order to compare our results above ρ_D with those by other methods, we show the proton number of the most stable nuclei in Fig. 4-8. At the matter densities $\rho \leq 1\times10^{14}$ g/cm^3, our results are fairly close to the liquid-drop calculation by Ravenhall, Bennett and Pethick [17] and to the Thomas-Fermi calculation by Ogasawara and Sato [32]. Although the Hartree-Fock calculation by Negele and Vautherin [19] gives the maximum Z as large as 50, this is attributed to the shell effect which is neglected in our semiclassical calculations. It should be noted that the transition from sphere to cylinder occurs at $\rho \approx 1.0\times10^{14}$ g/cm^3.

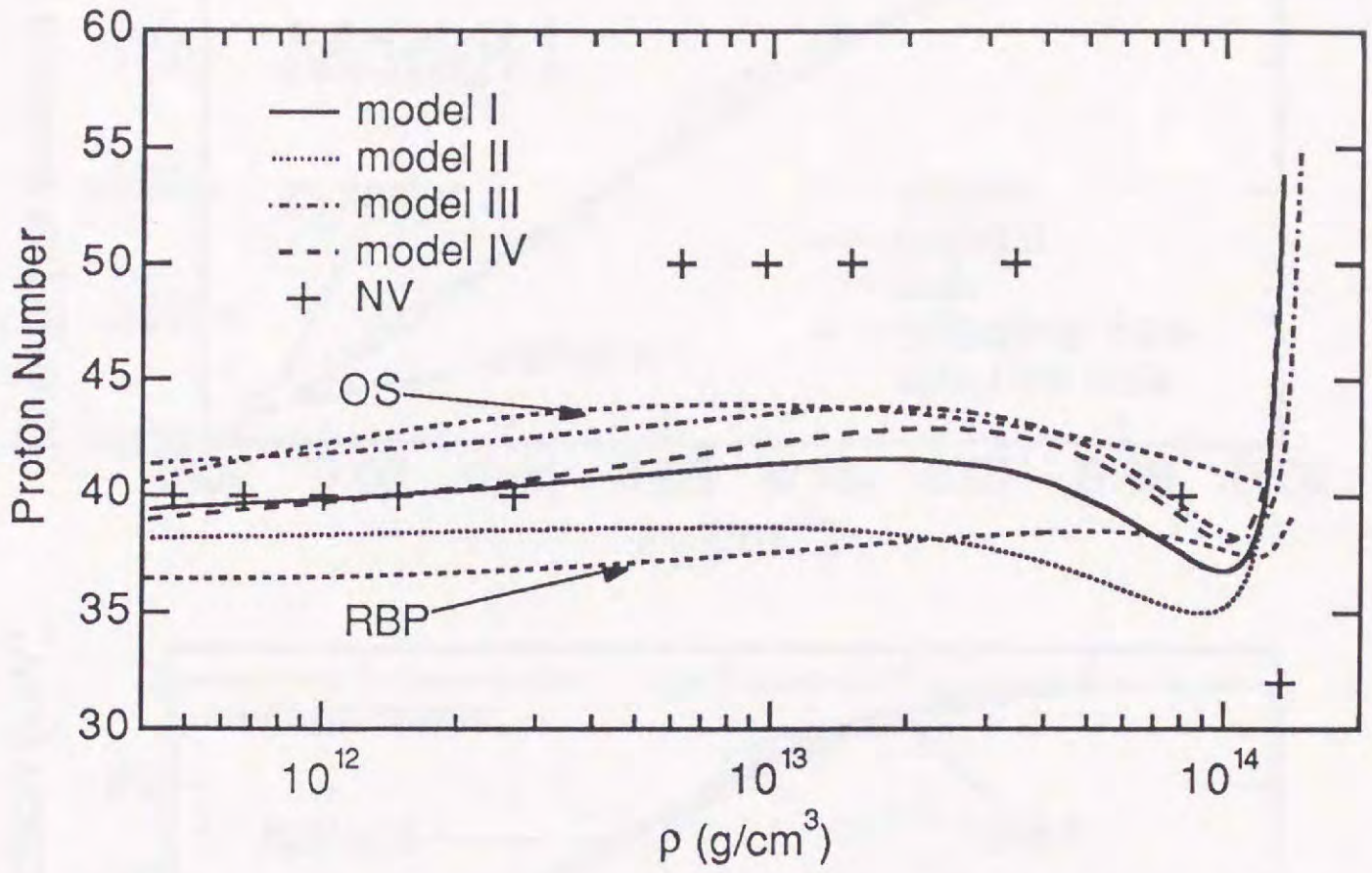

Fig. 4-8. Proton number of the most stable spherical nucleus. RBP and OS mean the liquid-drop calculation by Ravenhall, Bennett and Pethick [17] and the Thomas-Fermi calculation by Ogasawara and Sato [32], respectively. Crosses represent the Hartree-Fock results by Negele and Vautherin [19].

4.7. Non-spherical nuclei in the inner crust of a neutron star

4.7.1. Energy of non-spherical nuclei

When the matter density reaches about 10^{14} g/cm^3, the nucleus occupies a substantial portion of the cell, and non-spherical nuclei become energetically favorable. Figs. 4-9 to 4-12 show the energy per nucleon of the matter in question relative to that of uniform matter. In all of our models, as the density of matter increases, the energetically most favorable nuclear shape changes from sphere, to cylinder, slab, cylindrical hole and spherical hole, and the nuclei finally melt into uniform matter.

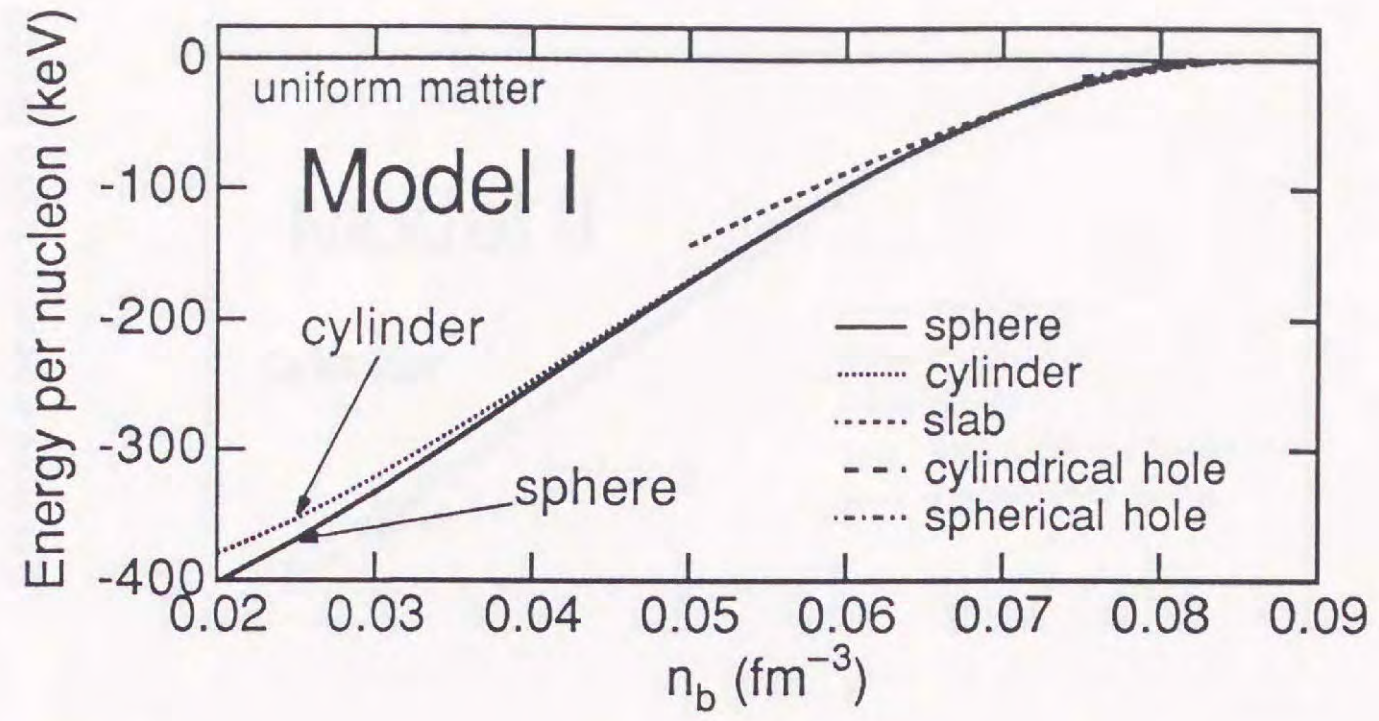

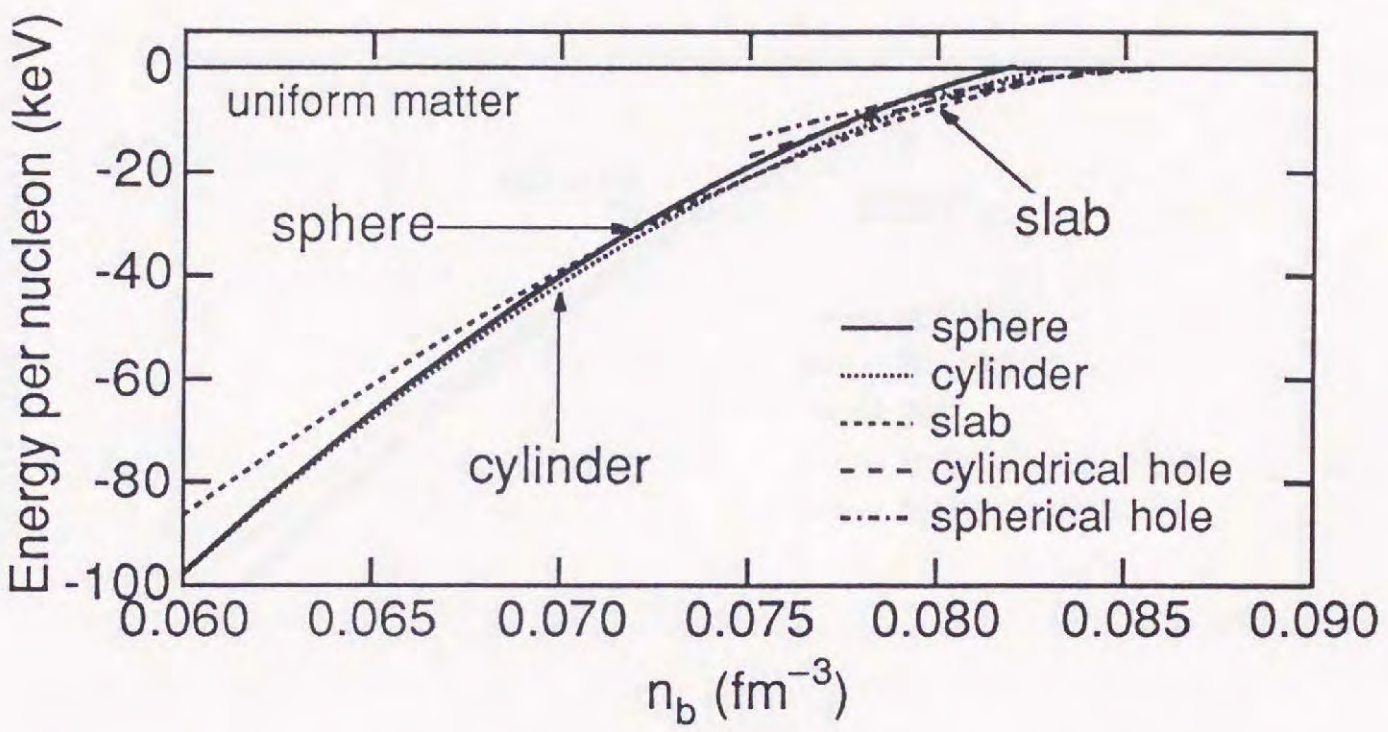

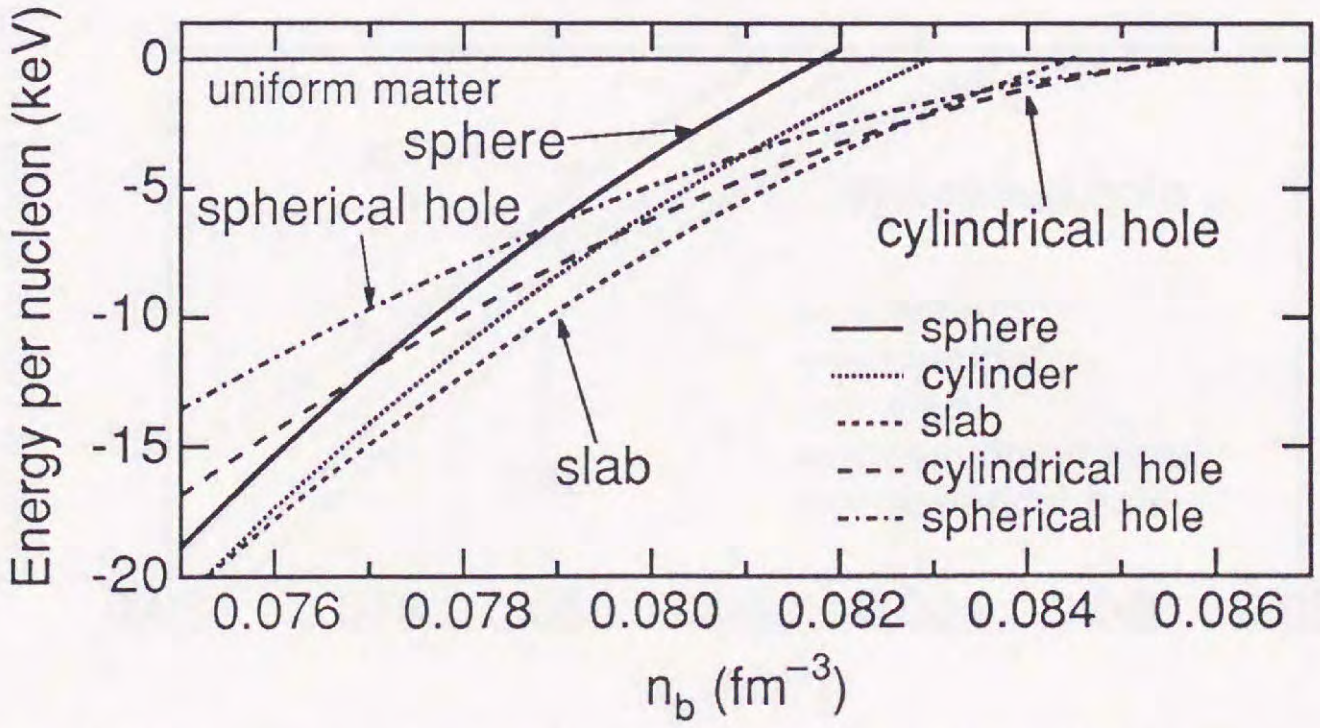

Fig. 4-9. Energy per nucleon relative to uniform matter in model I.

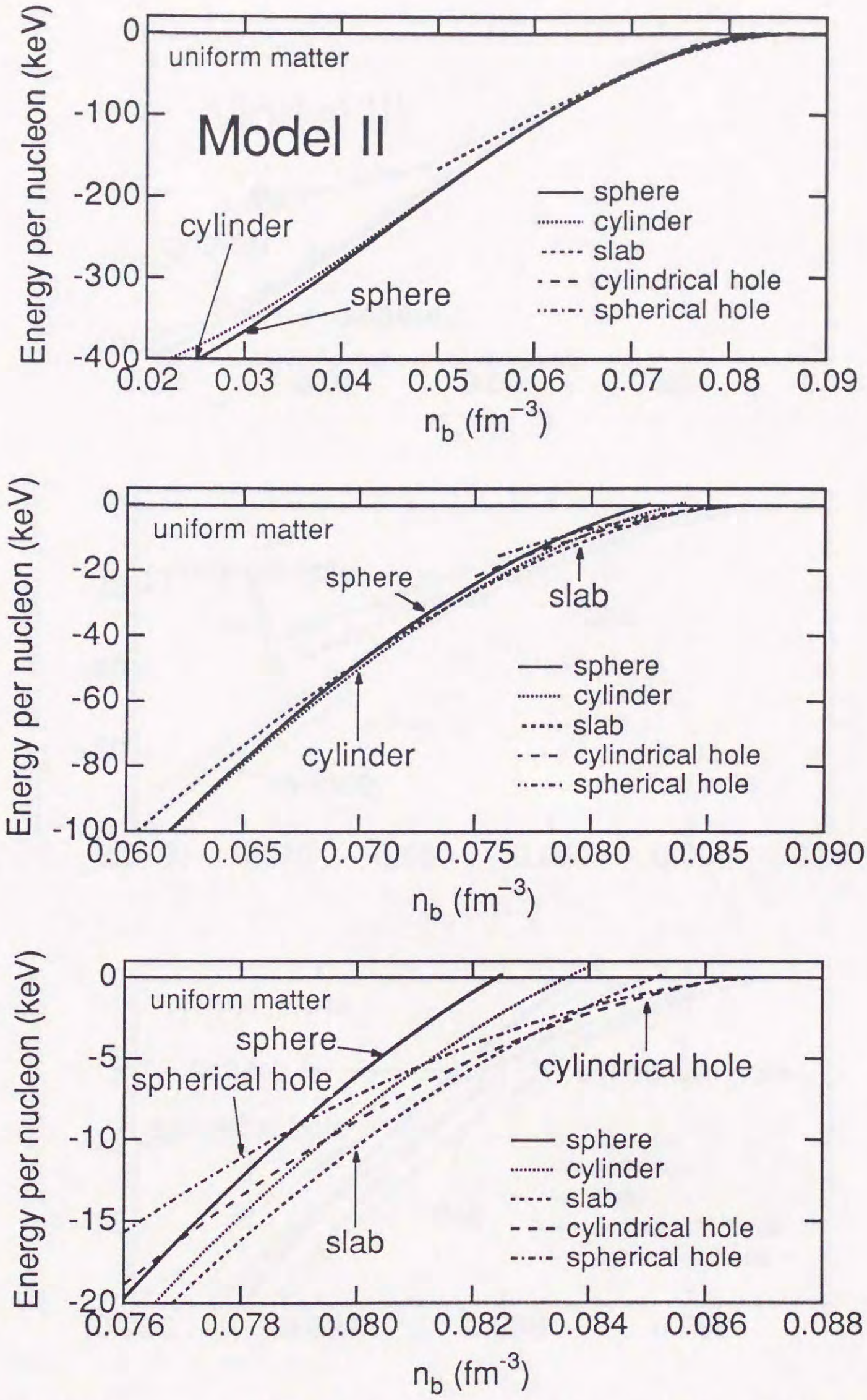

Fig. 4-10. Energy per nucleon relative to that of uniform matter in model II.

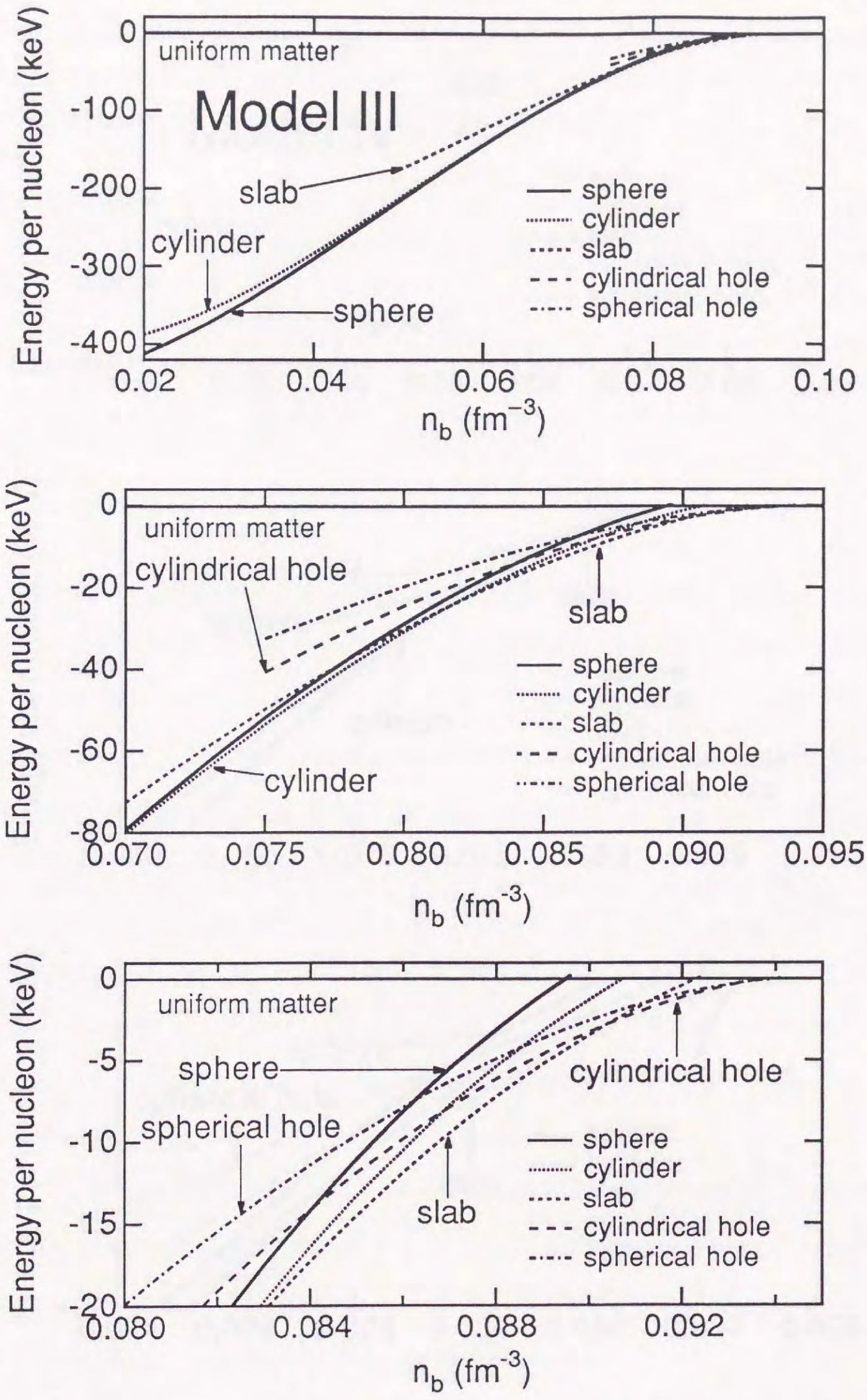

Fig. 4-11. Energy per nucleon relative to that of uniform matter in model III.

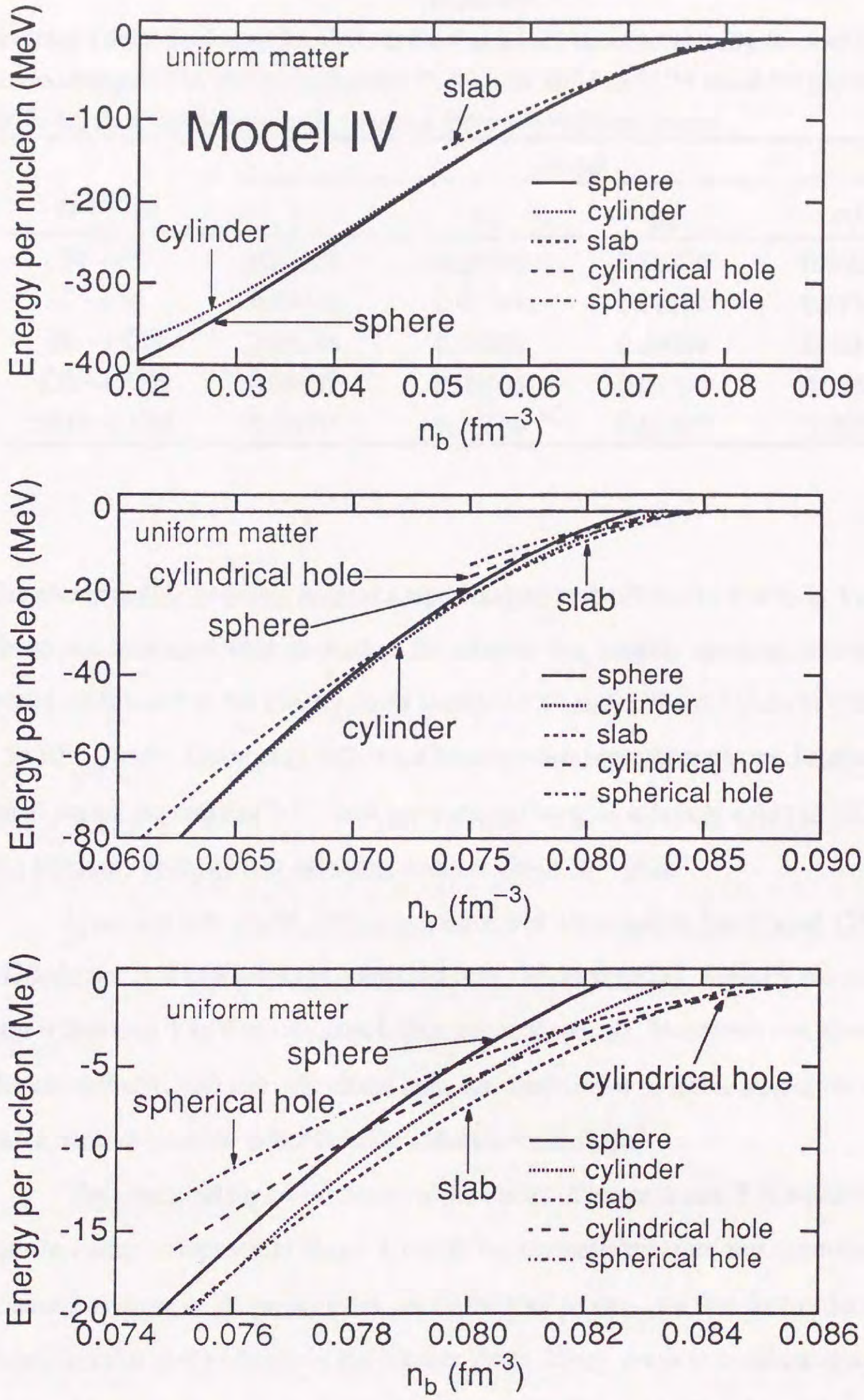

Fig. 4-12. Energy per nucleon relative to that of uniform matter in model IV.

Table 4-7

Average nucleon number densities in fm^{-3} at which the energetically favored nuclear shape changes. The abbreviations SP, C, SL, CH, SPH and UM stand for sphere, cylinder, slab, cylindrical hole, spherical hole and uniform matter.

transition	model			
	I	II	III	IV
SP → C	0.05858	0.05790	0.06375	0.06059
C → SL	0.07492	0.07397	0.08162	0.07544
SL → CH	0.08274	0.08309	0.09039	0.08342
CH → SPH	0.08537	0.08605	0.09330	0.08541
SPH → UM	0.08605	0.08689	0.09407	0.08582

The energetically favorable nuclear shape changes at the densities shown in Table 4-7. These densities somewhat depend on the models, but, roughly speaking, non-spherical nuclei are favored in the density range between 0.06 and 0.09 fm^{-3} (1.0×10^{14} and 1.5×10^{14} g/cm^3). The energy difference between two successive phases is generally small (up to the order of 0.1-1 keV per nucleon) because it is only a part of the surface and Coulomb energies that are rather small at about 10^{14} g/cm^3.

Spherical hole nuclei, whose existence was discussed by Lamb et *al.* [20] in 1978, do not gain much energy compared with the other nuclei. Actually the energy gain is less than 1 keV per nucleon independent of models. Therefore, non-spherical shapes, cylinder, slab and cylindrical hole, are much more probable shapes for the stable nucleus than the rather familiar spherical-hole shape.

The condition for co-existence of the nuclei of shape A and B in equilibrium is that the matter composed of shape-A nuclei has the same pressure and chemical potential as those of shape-B nuclei. In all the four models, we find first-order phase transitions due to the change of the nuclear shape. Every shape in consideration can exist stably in the density range listed in Table 4-8. This table also shows that the density range for each nuclear shape becomes successively narrower although this feature is not seen in the recent liquid-drop calculation [3].

Table 4-8

Ranges of the average nucleon number density in 10^{-2} fm^{-3} where various nuclear shapes exist stably. The abbreviations for the nuclear shapes are the same as those in Table 4-7.

shape	model							
	I		II		III		IV	
	lowest	highest	lowest	highest	lowest	highest	lowest	highest
SP		5.851		5.784		6.369		6.053
C	5.864	7.477	5.797	7.381	6.381	8.146	6.065	7.530
SL	7.508	8.256	7.413	8.290	8.179	9.020	7.558	8.325
CH	8.292	8.530	8.327	8.599	9.057	9.323	8.359	8.535
SPH	8.544	8.597	8.612	8.679	9.337	9.398	8.547	8.573
UM	8.613		8.698		9.416		8.590	

From Table 4-8 and Figs. 4-9 to 4-12, we can see that the phase transitions are rather weak. Density jumps due to these transitions are about 10^{-4} fm^{-3} as reported by Lorenz, Ravenhall and Pethick with the compressible liquid-drop model. Consideration of non-spherical nuclear shapes makes the transition to uniform matter smoother. The existence of non-spherical nuclei reduces the energy per nucleon by an amount up to 3-5 keV compared with the case in which only spherical and spherical hole nuclei are considered.

4.7.2. Nucleon distributions

In spite of the differences in the nuclear energy density ε, all the four models yield similar nucleon distributions. We mainly show results in model I. As for the average composition, the proton fraction Y_p varies slowly with the matter density as shown in Fig. 4-13. This figure also shows that the differences of Y_p among various shapes are small.

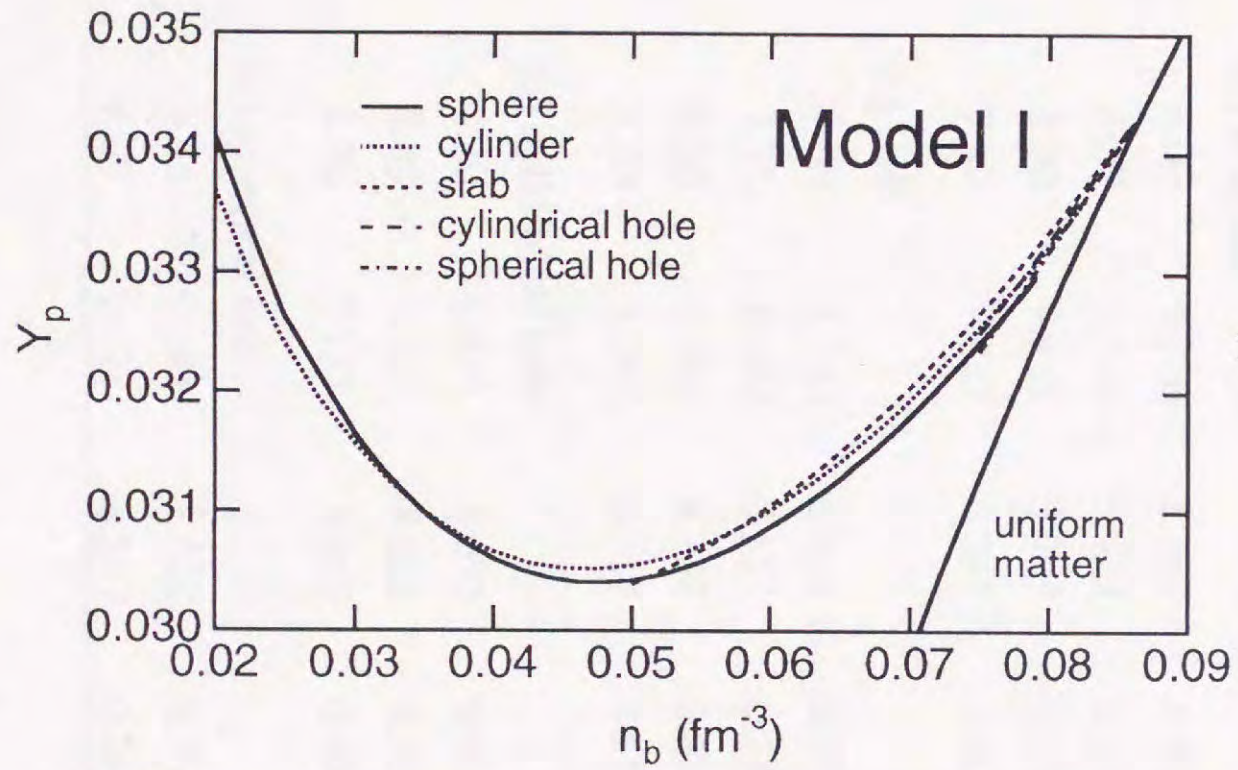

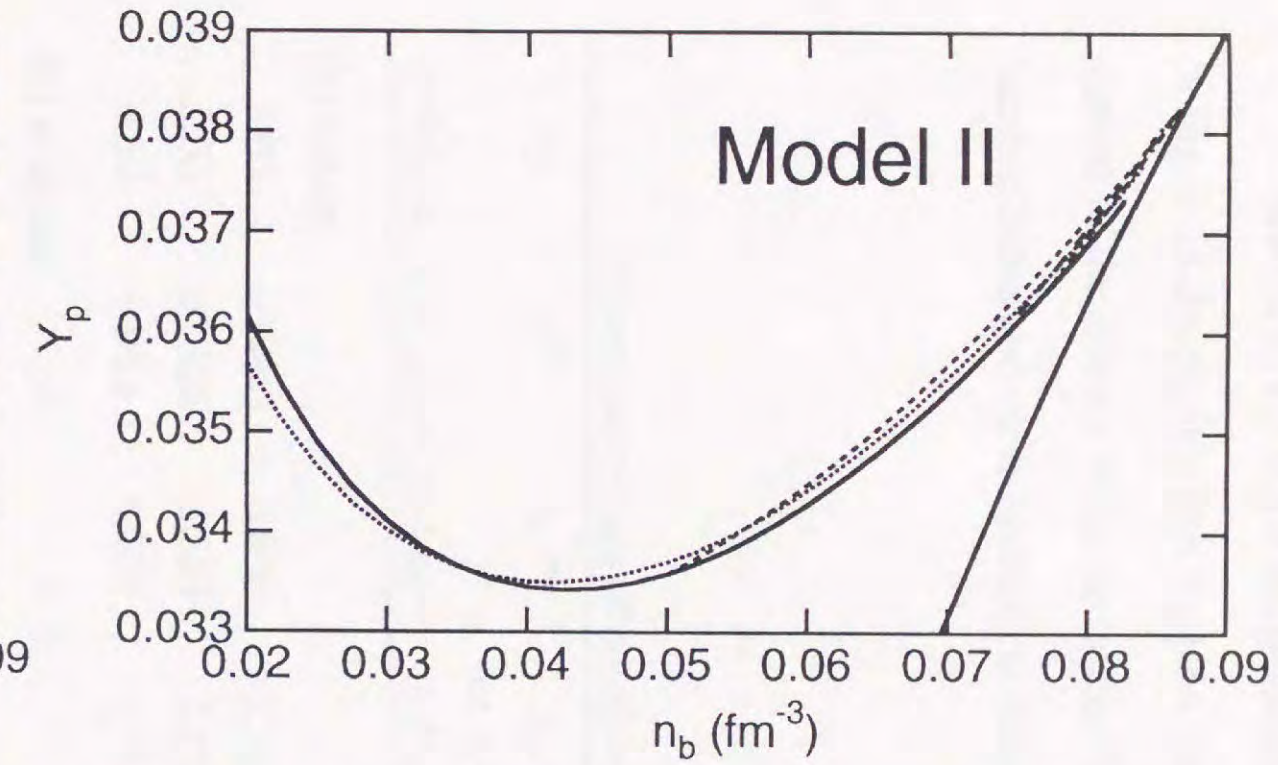

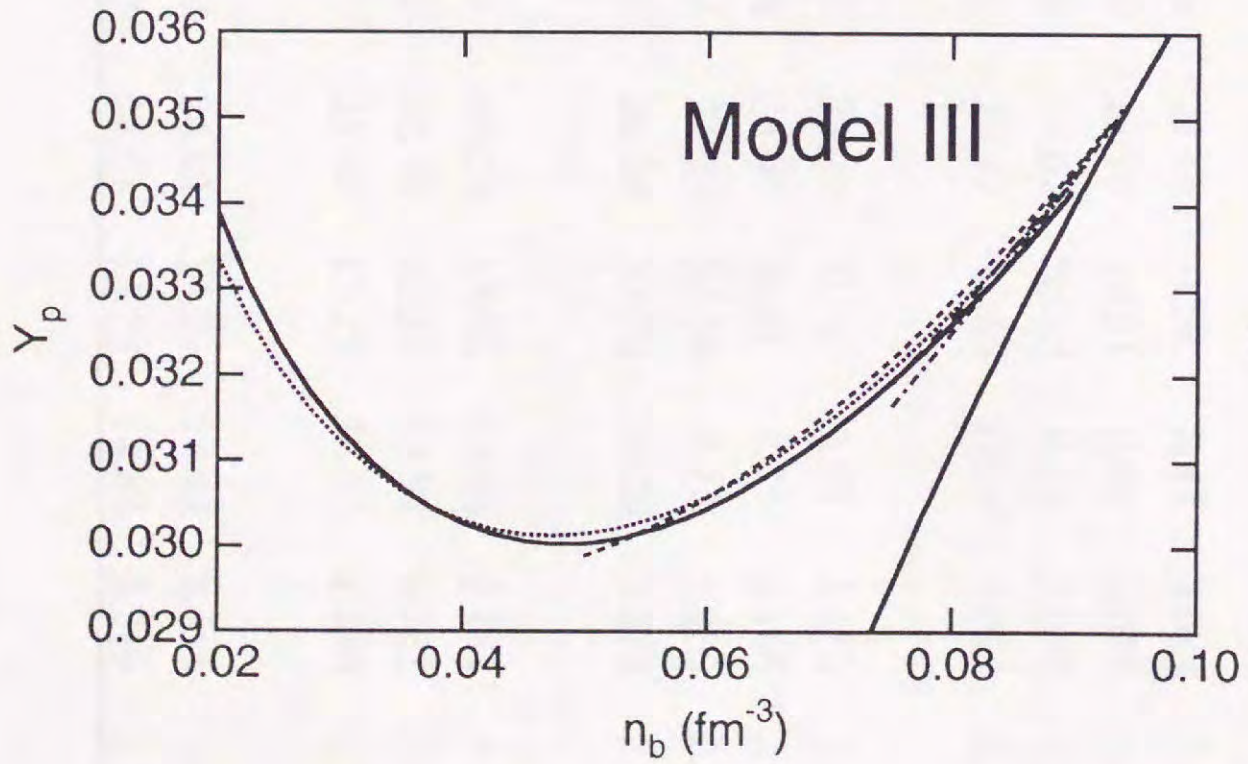

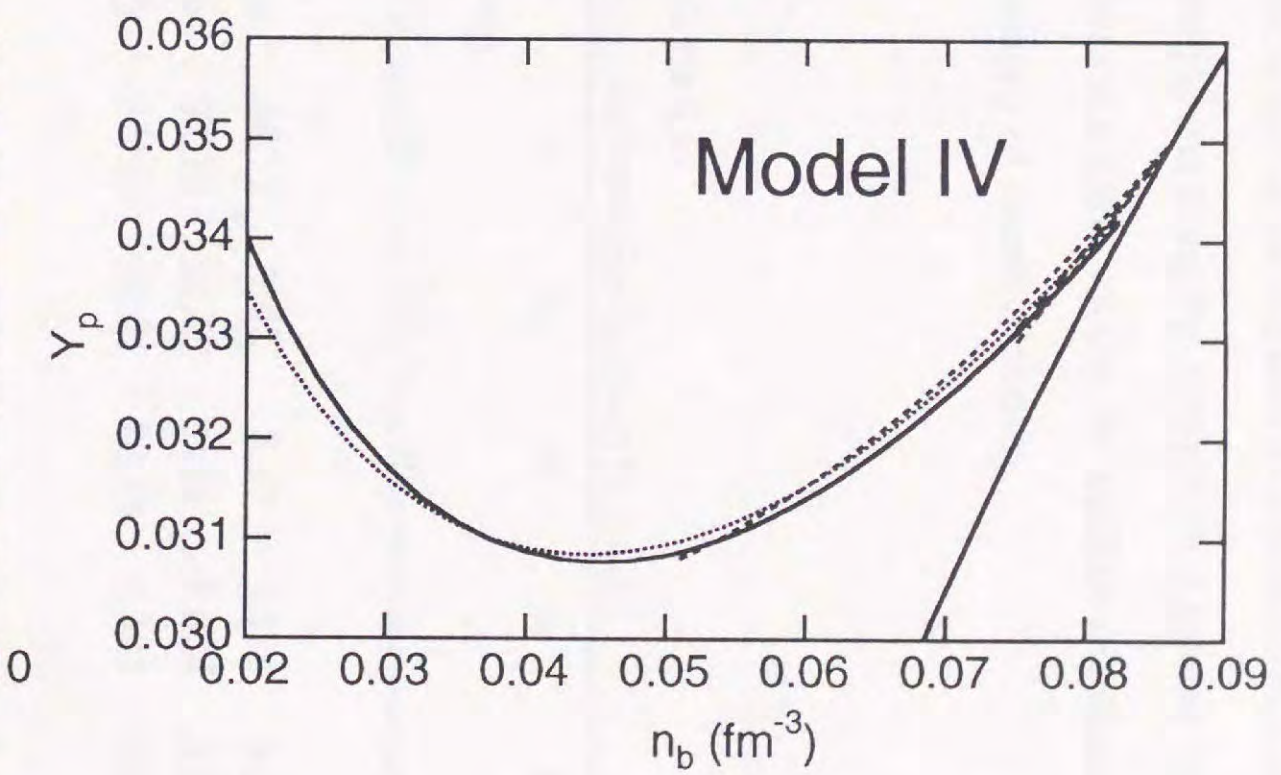

Fig. 4-13. Proton fraction as a function of density

We list in Table 4-9 the parameter values of the nucleon distributions and show in Fig. 4-14 the equilibrium nucleon distributions along the straight lines joining the centers of the nearest nuclei or holes. There is a tendency that the nucleon distributions become more and more uniform as the density of matter increases.

Table 4-9

Parameter values of equilibrium nucleon distributions in model I.

n_b	n_n^{in}	n_n^{out}	n_p^{in} (or n_p^{out})	a	R_n	R_p	t_n	t_p
10^{-2} fm^{-3}	10^{-2} fm^{-3}	10^{-2} fm^{-3}	10^{-2} fm^{-3}	fm	fm	fm		
(a) sphere								
1.00	10.490	0.830	3.866	46.75	9.42	8.17	4.825	6.291
3.00	10.354	2.554	2.725	34.75	10.62	9.19	4.624	5.849
5.50	9.984	4.701	1.755	27.99	12.01	10.73	4.395	5.086
(b) cylinder								
6.00	9.720	5.107	1.517	27.17	9.78	8.43	3.084	3.386
6.50	9.630	5.527	1.338	25.77	10.27	9.01	3.076	3.303
7.00	9.525	5.943	1.156	24.62	10.92	9.78	3.079	3.221
7.40	9.427	6.275	1.007	23.97	11.66	10.64	3.097	3.169
(c) slab								
7.60	8.987	6.401	0.785	23.71	9.06	7.92	2.151	2.120
7.75	8.982	6.527	0.744	23.07	9.44	8.35	2.166	2.116
8.00	8.966	6.738	0.673	22.23	10.20	9.24	2.203	2.132
8.20	8.944	6.917	0.613	21.84	10.92	10.20	2.275	2.167
(d) cylindrical hole								
8.30	6.934	8.675	0.484	24.30	13.52	13.03	3.187	4.117
8.40	7.029	8.666	0.457	23.79	13.35	12.91	2.737	3.411
8.50	7.137	8.645	0.427	23.48	13.25	12.91	2.294	2.714
(e) spherical hole								
8.55	7.145	8.522	0.374	24.89	15.27	14.83	2.455	2.968
8.57	7.171	8.517	0.367	24.81	15.28	14.86	2.289	2.727

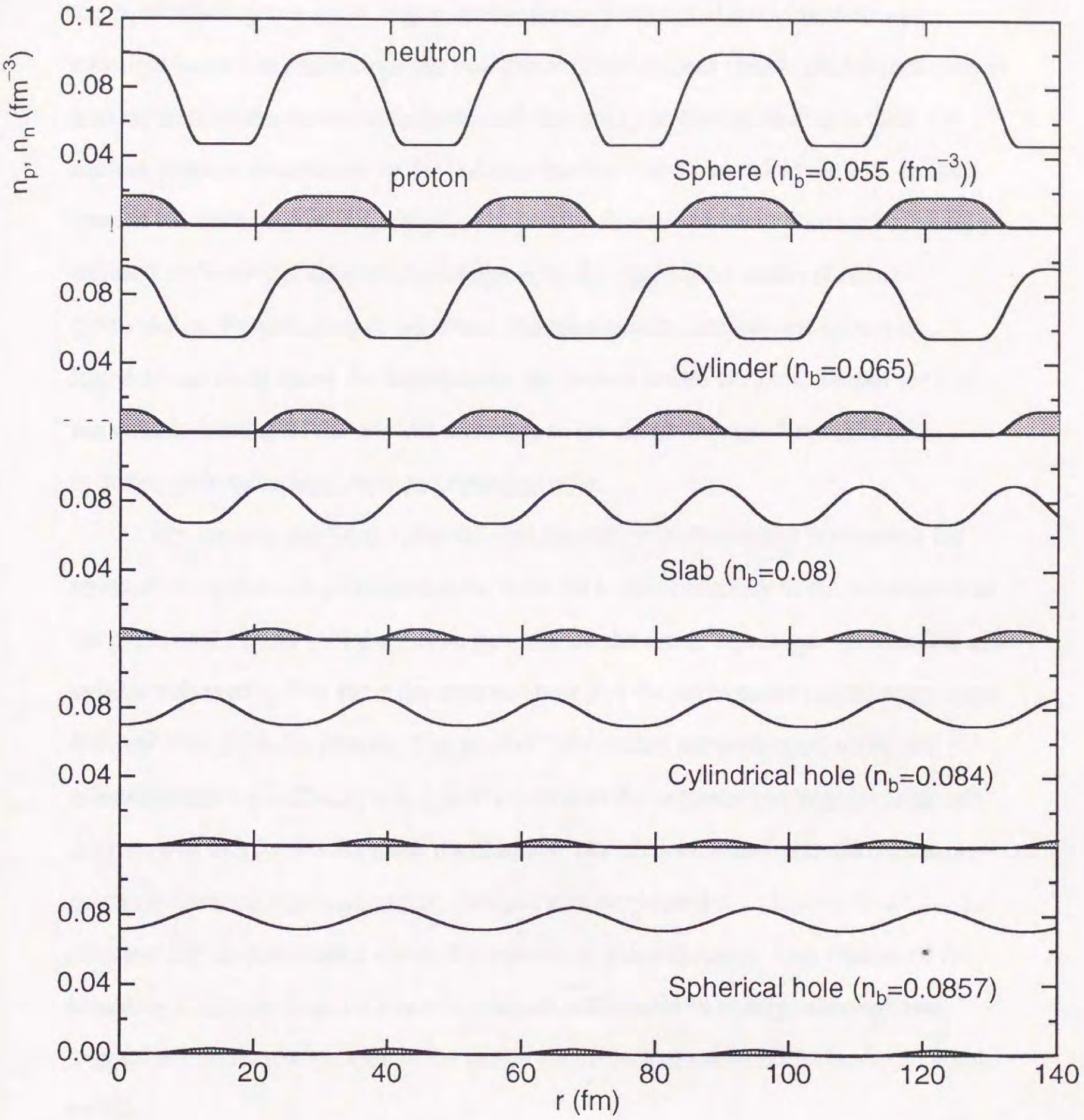

Fig. 4-14. The neutron (upper) and proton (lower, shaded) distributions along the straight lines joining the centers of the nearest nuclei or hole. Calculations are made with model I, but the other models give similar results.

The size of the cell shows appreciable dependence on the geometry of the nucleus. Fig. 4-15 shows the lattice constant as a function of matter density. The lattice constant in the equilibrium geometry is largest for the three-dimensional nuclei (sphere and spherical hole) and smallest for the one-dimensional nucleus (slab). This dependence is also reported in the recent liquid-drop calculation [3]. In the liquid-drop model, the nuclear shape is determined by the volume fraction of the nucleus in the cell. In the present calculations, the slab-shape, cylindrical hole and spherical hole nuclei have so diffused surfaces that the correspondence with the liquid-drop model is rather questionable. Nevertheless, if we notice that the nucleon distributions shown in Fig. 4-14 are those along the lines joining the nearest nuclei or holes, we can see that the volume fraction of the nucleus increases as the shape changes from sphere to cylinder, slab, cylindrical hole and spherical hole.

We can also see from Table 4-9 that the values of the surface parameters for neutrons are appreciably different from those for protons contrary to the assumption in the preliminary study [10] that these surfaces are the same. The larger values of R_n and smaller values of t_n than those for protons show that the surfaces for neutrons are more diffused than those for protons. The present calculations are performed under the constraint that the radius R_i is less than or equal to the radius of the Wigner-Seitz cell. Above $n_b \approx 0.082$ fm^{-3} in model I, the diameter $2R_i$ thus obtained exceeds the nearest-neighbor distance. For comparison, we have also performed calculations in which the diameter $2R_i$ is constrained within the nearest-neighbor distance. This change of the boundary condition does not cause significant differences in energy, although non-negligible differences are seen in the lattice constants and nucleon distributions of hole nuclei.

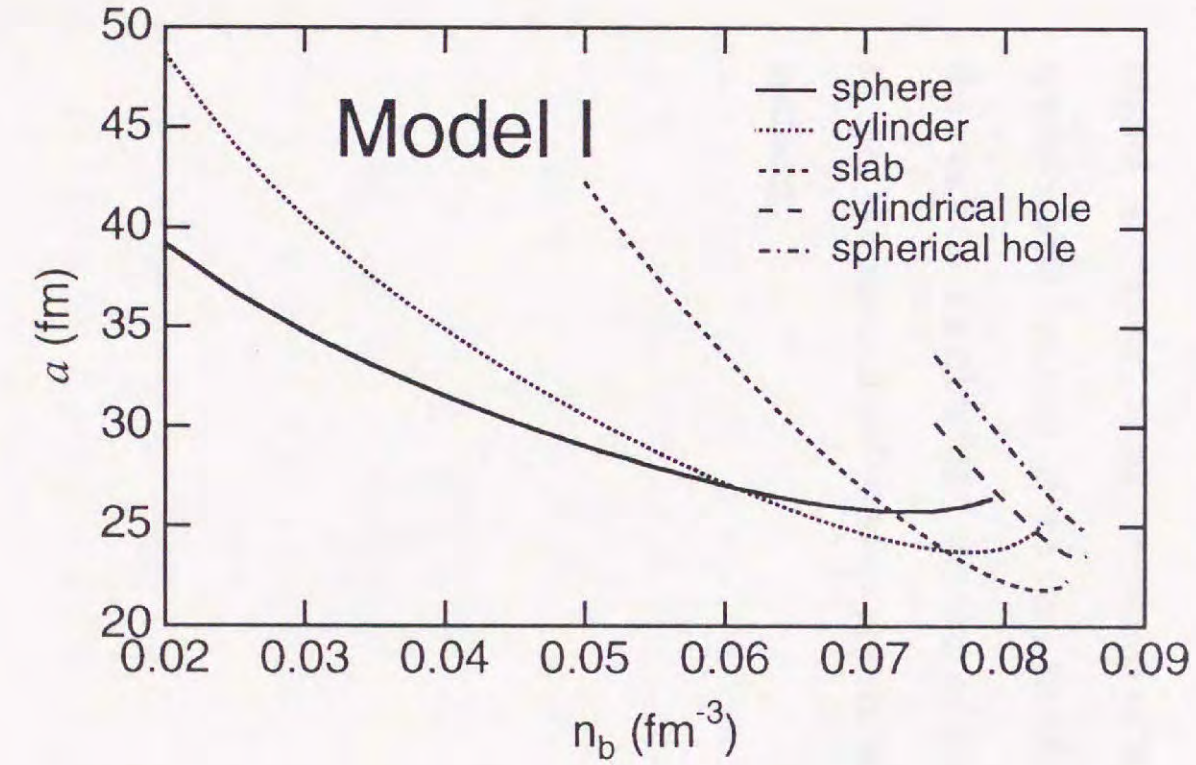

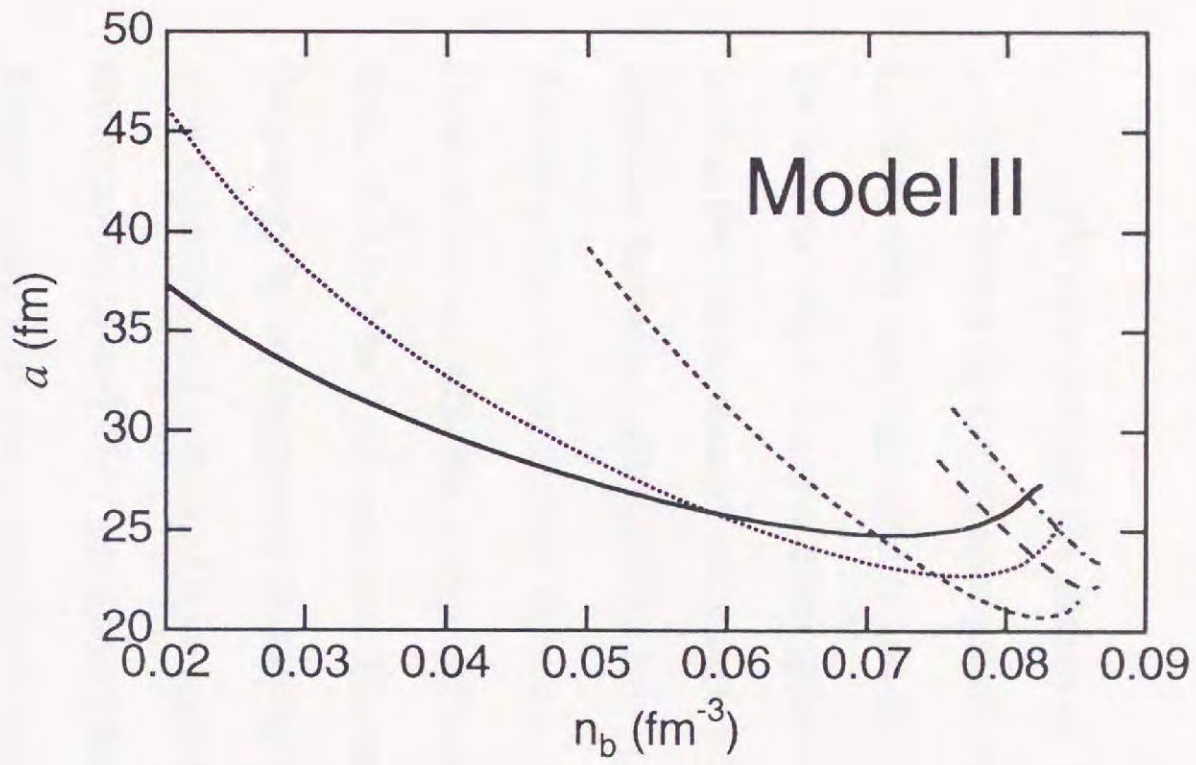

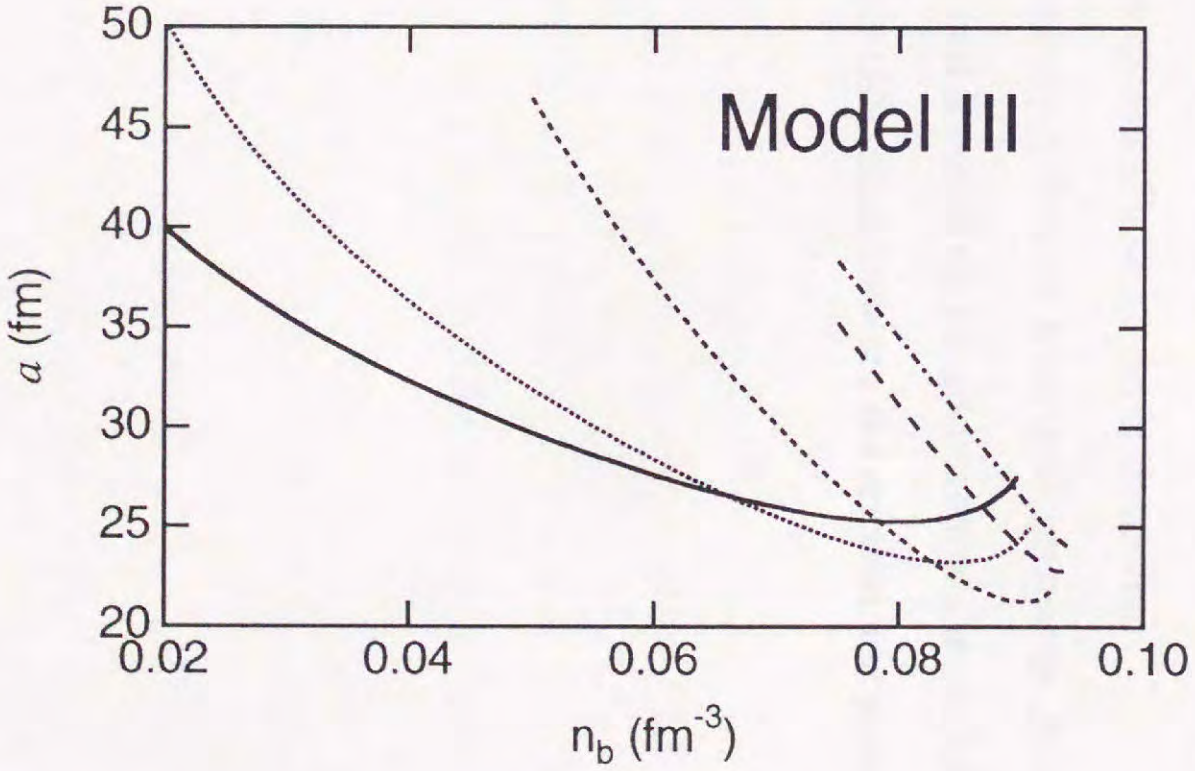

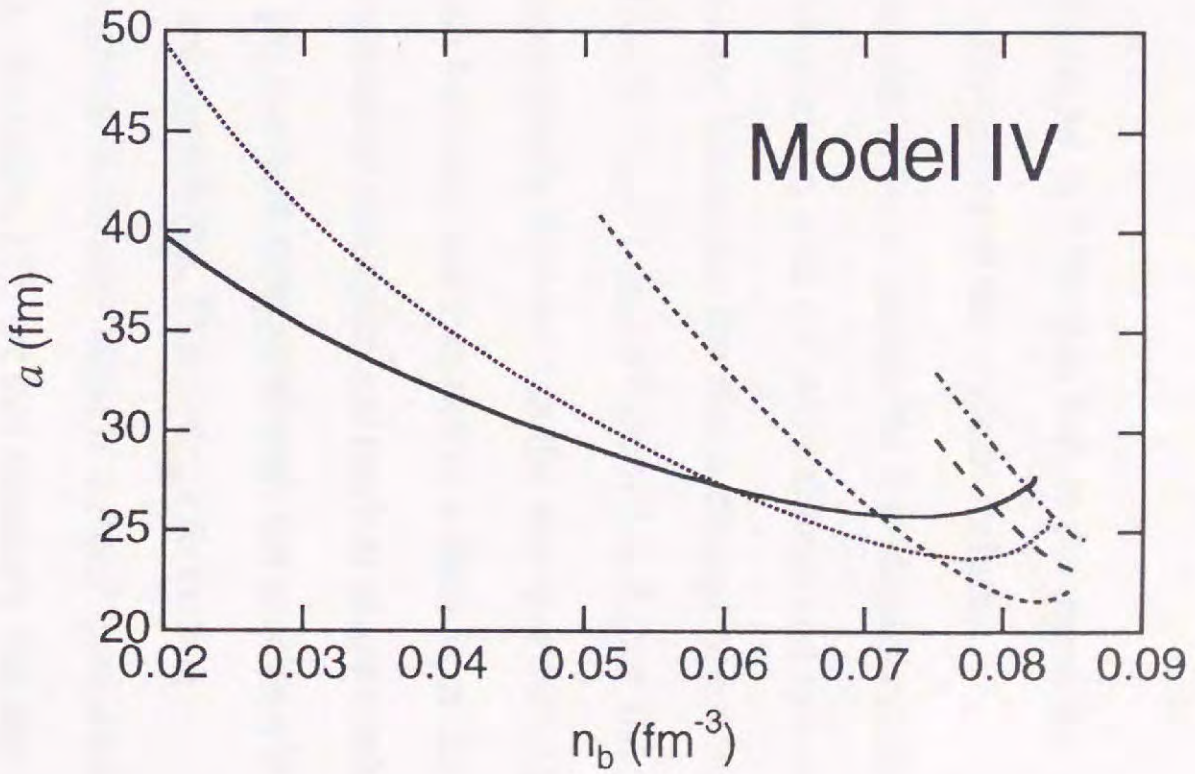

Fig. 4-15. Lattice constant as a function of matter density

4.8. Conclusion of the Thomas-Fermi calculation

We have studied the shapes of the nuclei in NSM just before the transition to uniform matter by taking account of the diffuseness of the nuclear surface. Qualitatively, this inclusion of the diffuseness did not change the liquid drop result that the nuclear shape changes from sphere to cylinder, slab, cylindrical hole and spherical hole as the matter density increases. We have found that the shape change occurs at densities between 0.06 and 0.09 fm^{-3} (1.0×10^{14} and 1.5×10^{14} g/cm^3) and that the density range for each shape becomes successively narrower in the above order. At a fixed matter density, the energy difference between two successive shapes is of the order of 0.1~1 keV per nucleon. The existence of non-spherical nuclear shapes reduces the energy by an amount up to 3~5 keV per nucleon compared with the case in which only spherical and spherical hole nuclei are considered. This energy reduction corresponds to 4~6 MeV per spherical nucleus. Although there is a small quantitative disagreement with the recent liquid-drop calculation [3], we can conclude that the cylindrical and slab nuclei are more important than the rather familiar spherical hole nuclei. Moreover, actual existence of the spherical hole nuclei is somewhat questionable because of the very small energy difference from uniform matter. As for the nucleon distributions, the size of the cell depends on the geometry of the nuclear shape. We have also found an appreciable difference between the neutron and proton surfaces.

Chapter 5

Shell energies of non-spherical nuclei

It is well known that the normal spherical nuclei show shell effects. Non-spherical nuclei will also show some shell effects. These shell effects are not taken into account in the preceding chapters. In this chapter we calculate the shell energies of the non-spherical nuclei.

5.1. Single-particle potential

We calculate single-particle energies e_{SP} for a nucleon by solving the following Schrödinger equation: For a proton

$$\left\{-\frac{\hbar^2}{2m_p}\Delta + U(r) + V_{LS}(r) + V_C(r)\right\}\psi(r) = e_{SP}\,\psi(r)\,, \qquad (5.1a)$$

and for a neutron

$$\left\{-\frac{\hbar^2}{2m_n}\Delta + U(r) + V_{LS}(r)\right\}\psi(r) = e_{SP}\,\psi(r)\,. \qquad (5.1b)$$

Here, m_i (i=n, p) is the nucleon mass and r is the distance from the center of the nucleus (central axis for cylinder and central plane for slab). We assume that the SP potential, which consists of the central potential $U(r)$, the spin-orbit potential $V_{Ls}(r)$ and the Coulomb potential $V_C(r)$, depends only on r, although there may be some dependence on the direction in the actual SP potential when the nuclei constitute a lattice. The potentials $U(r)$ and $V_{Ls}(r)$ for a neutron differ from those for a proton although no distinction is made in Eqs. (5.1a) and (5.1b). These potentials are determined in the following way with use of the potential-energy-density functional and the nucleon distributions obtained in Chapter 4.

The nucleon SP potential in uniform nuclear matter is defined as

$$U_0 = \frac{\partial \upsilon(n_n, n_p)}{\partial n_i}, \qquad \text{(i=n, p)} \qquad (5.2)$$

where $\upsilon(n_n, n_p)$ is the potential-energy density in uniform nuclear matter with neutron (proton) number density n_n (n_p). We use the same function for $\upsilon(n_n, n_p)$ as in Chapter 4,

$$\upsilon(n_n, n_p) = \left[1 - (1 - 2x)^2\right] \upsilon_s(n) + (1 - 2x)^2 \upsilon_n(n) \tag{5.3}$$

with $n=n_n+n_p$ and $x=n_p/n$.

In this chapter we use the parameter sets named models I, II and III in Chapter 4, and omit model IV because it is rather close to model I. Model I may be taken as a standard one, while model II has a large surface symmetry energy and model III has a large incompressibility. These models also differ from each other in the inhomogeneity energy. If we neglect the finite-range effect of nuclear forces, we can calculate U_0 as a function of r with use of the nucleon distributions obtained in Chapter 4. Actually this effect can not be neglected in the present case in which the nucleon distributions are clearly non-uniform by making nuclei. In Chapter 4, we represented this effect by energy terms proportional to squares of the gradients of the local nucleon densities (Eq. (4.14)). In this chapter, we take it into account by modifying $U_0(r)$ by the following convolution:

$$U(r) = \left(\frac{1}{\sqrt{\pi}\,\kappa}\right)^3 \int d\boldsymbol{r}'\, U_0(r') \exp\left[-|\boldsymbol{r}'-\boldsymbol{r}|^2/\kappa^2\right], \tag{5.4}$$

where κ is a parameter representing the range of nuclear interactions. The integration in Eq. (5.4) should be taken over the whole space. In the limit $\kappa \to 0$, $U(r)$ becomes equal to $U_0(r)$.

The spin-orbit potential is caused by the gradients of nucleon distributions, and we assume the following form for it:

$$V_{LS}(r) = \left\{ \lambda_1 \frac{dn(r)}{dr} \pm \lambda_2 \frac{d}{dr}\left[n_n(r) - n_p(r)\right] \right\} \boldsymbol{u}\times\boldsymbol{k}\cdot\boldsymbol{s}\,, \tag{5.5}$$

where the sign + is used for a proton, and – for a neutron. The vector $\boldsymbol{u}$ is the unit vector perpendicular to the surface of the nucleus, $\boldsymbol{k}$ is the wave-number vector, and $\boldsymbol{s} = \frac{1}{2}\boldsymbol{\sigma}$ with σ being the Pauli operator. The parameters λ_1 and λ_2 determine the isoscalar and isovector strengths of the spin-orbit potential, respectively. For the spherical nucleus, Eq. (5.5) can be written in the following form:

$$V_{\mathrm{LS}}(r) = \frac{1}{r}\left\{\lambda_1 \frac{dn(r)}{dr} \pm \lambda_2 \frac{d}{dr}\left[n_{\mathrm{n}}(r) - n_{\mathrm{p}}(r)\right]\right\}(\boldsymbol{l}\cdot\boldsymbol{s}) \tag{5.6}$$

with $\boldsymbol{l}$ being the orbital angular momentum.

The values of the three parameters κ, λ_1 and λ_2, listed in Table 5-1, are chosen so as to give reasonable SP energies of ^{208}Pb. The SP potentials of ^{208}Pb in our models are shown in Fig. 5-1. Note that the central potential $U(r)$ extends beyond the nucleon distributions due to the convolution. The present value of λ_2 is so small in all models that the strength of $V_{\mathrm{LS}}(r)$ for a proton is almost indistinguishable from that for a neutron, though the former is slightly larger than the latter. In Fig. 5-2 we show the SP energies of ^{208}Pb obtained by our models together with those obtained by other authors [33,34]. All of our three models reproduce the correct sequences of the SP states for both neutrons and protons. The relative positions of the SP levels are also reproduced fairly well though the proton levels are systematically higher than the experimental ones. As will be seen in the next section, the shell energies mainly depend on the relative SP level positions. Therefore, the systematic shift of all the proton SP levels will not cause a serious problem.

Table 5-1
Values of the parameters in Eqs. (5.4) and (5.5)

	model		
	I	II	III
κ(fm)	1.170	1.229	1.229
λ_1(MeV·fm^5)	175.8	184.6	172.6
λ_2 (MeV·fm^5)	16.39	19.49	24.59

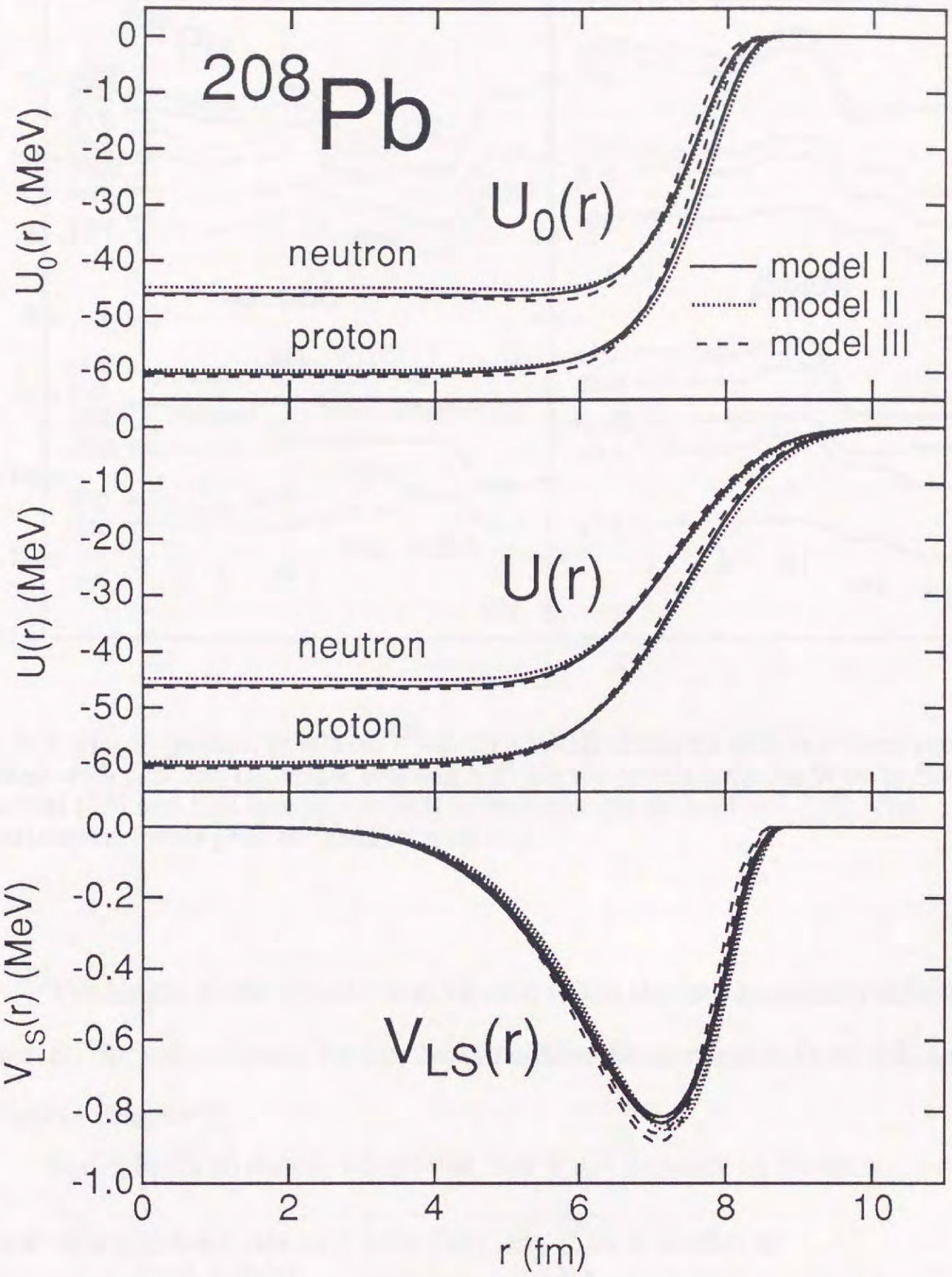

Fig. 5-1. Single-particle potentials of ^{208}Pb. The spin-orbit potential $V_{LS}(r)$ is shown for the $1p_{3/2}$ state.

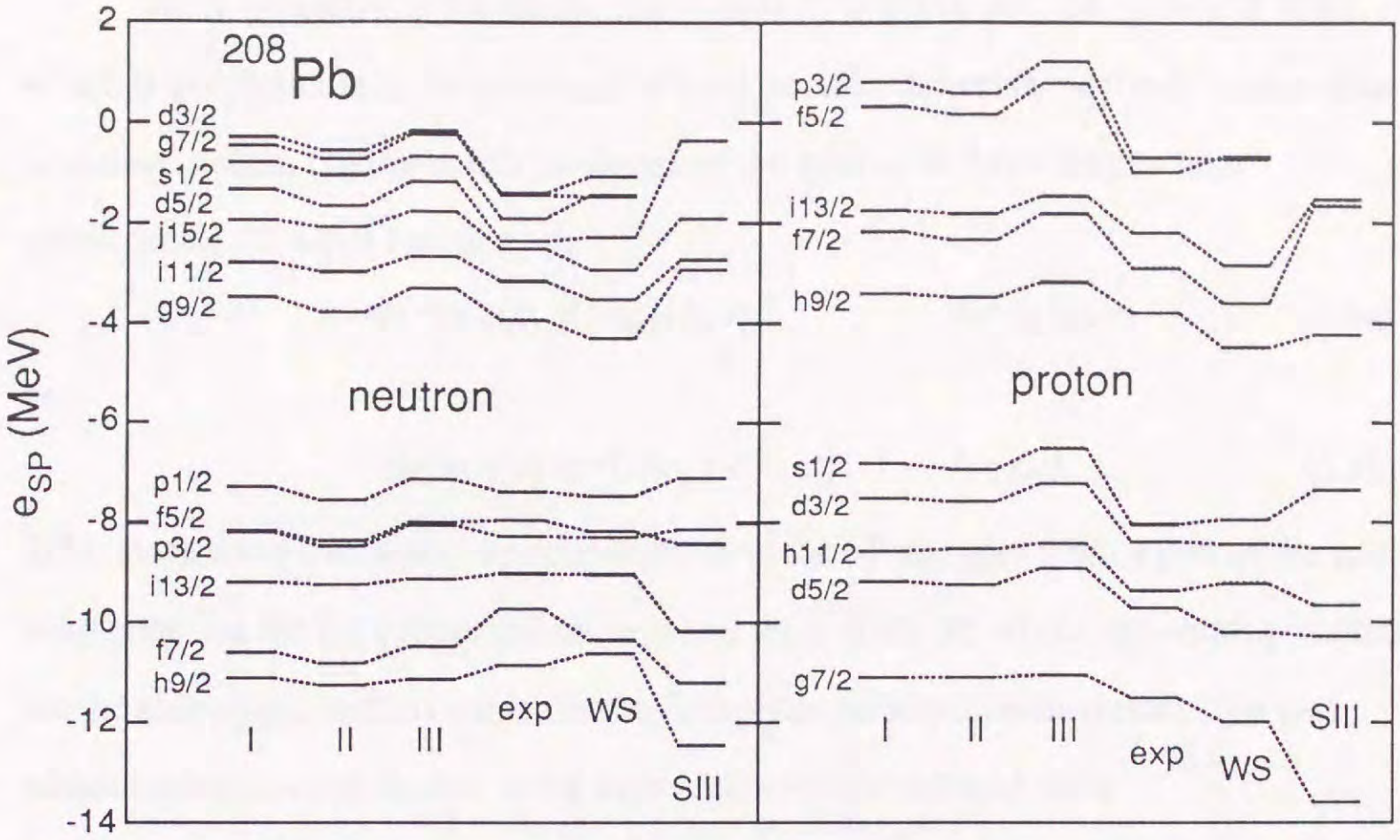

Fig. 5-2. Single-particle levels of ^{208}Pb. The levels obtained with our three models are marked with I, II and III, while WS and SIII are the levels with the Woods-Saxon potential [33] and SIII interaction [34] taken from the table of ref. [35]. The experimental levels [36] are marked with exp.

The length of the cylinder and the area of the slab are essentially infinite. However, for convenience, we use the same three dimensional cells of volume a^3 as defined in Chapter 3.

For cylindrical nuclei, we assume that $V_{\rm LS}(r)$ depends on the distance r from the central axis which we take as z-axis. Then, Eq. (5.5) is written as

$$V_{\rm LS}(r) = \frac{1}{r}\left\{\lambda_1 \frac{{\rm d}n(r)}{{\rm d}r} \pm \lambda_2 \frac{\rm d}{{\rm d}r}[n_{\rm n}(r) - n_{\rm p}(r)]\right\} \frac{1}{2}\left(l_z\sigma_z + yk_z\sigma_x - xk_z\sigma_y\right), \qquad (5.7)$$

where l_z is the z-component of the orbital angular momentum and σ_i is the i-th component of the Pauli spin operator. For slab-shape nuclei, we assume that $V_{\rm LS}(r)$ depends on the distance from the central plane which we take as x=0. Then, Eq. (5.5) is written as

$$V_{\rm LS}(r) = \left\{\lambda_1 \frac{{\rm d}n(r)}{{\rm d}r} \pm \lambda_2 \frac{\rm d}{{\rm d}r}[n_{\rm n}(r) - n_{\rm p}(r)]\right\} \frac{1}{2}\left(k_y\sigma_z - k_z\sigma_y\right) \qquad (5.8)$$

with r=|x|.

Since we consider the matter fairly close to uniform one, the spin-orbit force, which is proportional to the gradients of local nucleon densities, is much weaker than in normal nuclei. Owing to this weakness of the spin-orbit force we can take approximate SP wave functions as

$$\psi(\boldsymbol{r}) = \varphi(x, y) \exp\left(\mathrm{i}\, k_z\, z\right) \qquad \text{for cylinder} \qquad (5.9a)$$

and

$$\psi(\boldsymbol{r}) = \varphi(x) \exp\left[\mathrm{i}\left(k_y\, y + k_z\, z\right)\right] \qquad \text{for slab.} \qquad (5.9b)$$

With these wave functions, the contributions to the SP energies from a part of the spin-orbit potential for the cylindrical nucleus and those from the whole spin-orbit potential for the slab-shape nucleus vanish in the first-order perturbation treatment. The part which makes no contribution in the case of the cylindrical nucleus is

$$\delta V_{\mathrm{LS}}(r) = \frac{1}{r}\left\{\lambda_1 \frac{\mathrm{d}n(r)}{\mathrm{d}r} \pm \lambda_2 \frac{\mathrm{d}}{\mathrm{d}r}\left[n_{\mathrm{n}}(r) - n_{\mathrm{p}}(r)\right]\right\} \frac{1}{2}\left(y k_z \sigma_x - x k_z \sigma_y\right). \qquad (5.10)$$

Therefore, we can approximate the spin-orbit potential for the cylindrical nucleus to

$$V_{\mathrm{LS}}(r) = \frac{1}{r}\left\{\lambda_1 \frac{dn(r)}{dr} \pm \lambda_2 \frac{d}{dr}\left[n_{\mathrm{n}}(r) - n_{\mathrm{p}}(r)\right]\right\} \frac{1}{2}\, l_z \sigma_z, \qquad (5.11)$$

and neglect the spin-orbit potential for the slab-shape nucleus. In these approximations we can write the SP energies as

$$e_{\mathrm{SP}} = e_{xy} + \frac{\hbar^2}{2m_{\mathrm{i}}} k_z^2 \qquad \text{for cylinder,} \qquad (5.12a)$$

and

$$e_{\mathrm{SP}} = e_x + \frac{\hbar^2}{2m_{\mathrm{i}}}\left(k_y^2 + k_z^2\right) \qquad \text{for slab.} \qquad (5.12b)$$

Some examples of $U(r)$ and $V_{\mathrm{LS}}(r)$ are shown in Figs. 5-3 and 5-4, respectively. In calculating $U(r)$ with Eq. (5.4), the integration is performed over the Wigner-Seitz cell for spherical and cylindrical nuclei, and over the whole space for slab-shape nuclei. We see from Figs. 5-3 and 5-4 that, regardless of the nuclear shape, the SP potentials approach flat ones as the average matter density increases.

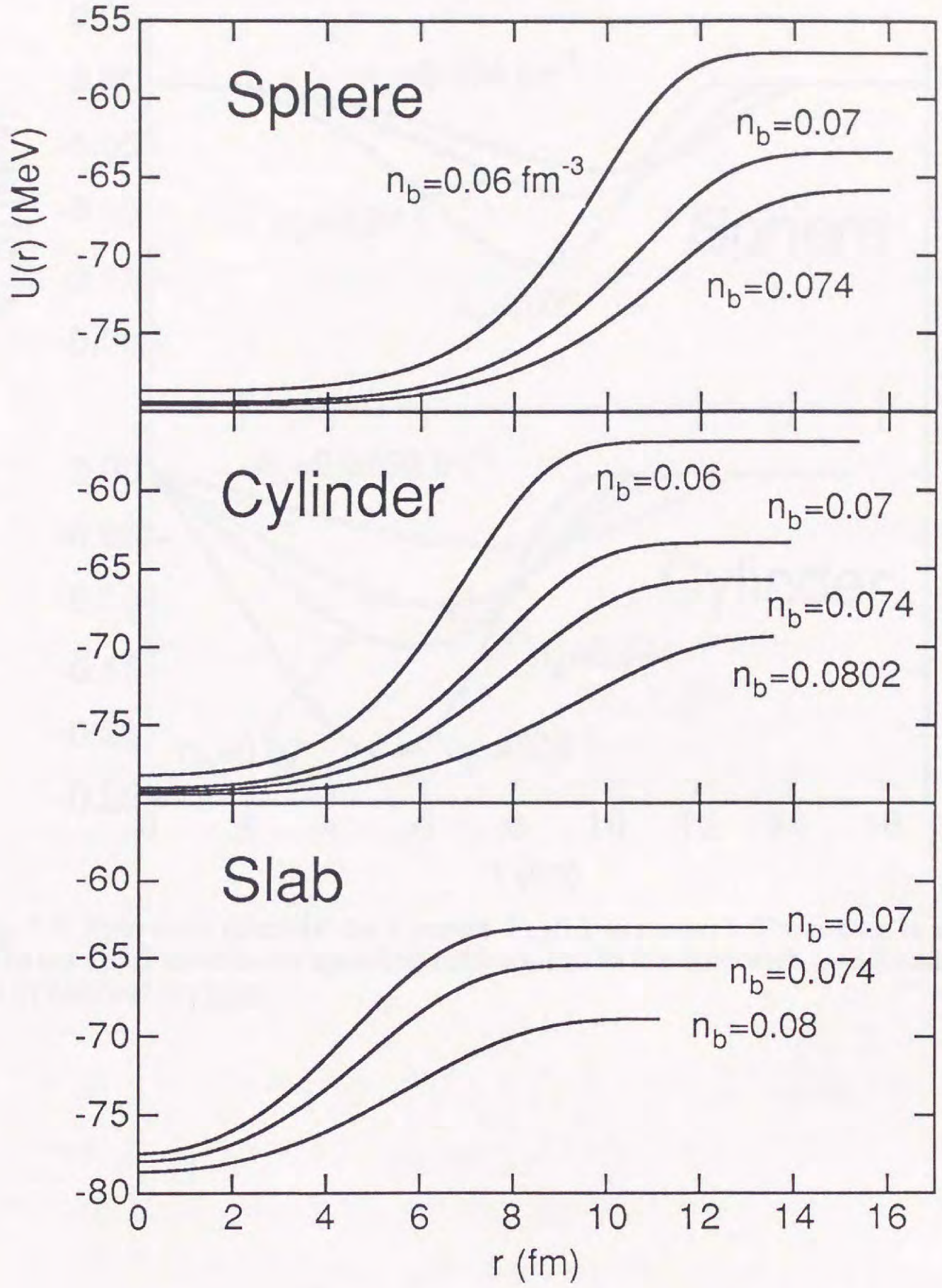

Fig. 5-3. Central component of the proton SP potential, $U(r)$, in model I. The symbol n_b denotes the average nucleon number density.

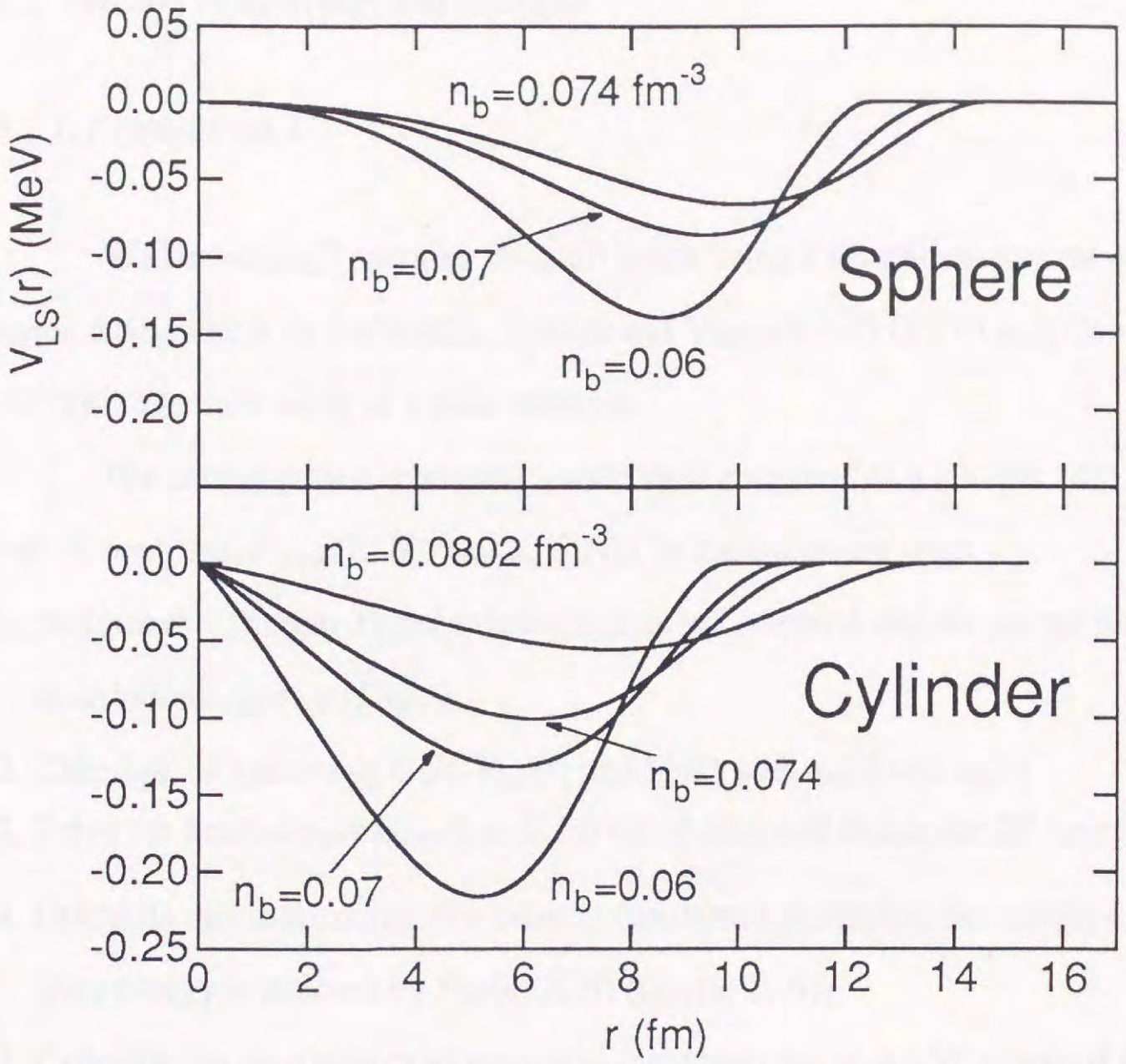

Fig. 5-4. Spin-orbit potential for a proton, $V_{LS}(r)$, in model I. The proton is assumed to be in the 1p3/2 state in the spherical nucleus, and in the state with j_z=3/2 and l_z=1 for the cylindrical nucleus.

5.2. Method of deriving shell energies

5.2.1. Prescription 1

We derive shell energies from SP levels using a simplified version of the method developed by Tachibana, Takano and Yamada [37] (TTY) and Uno et al. [38] (UTTKY) in their study of a mass formula.

We extract proton (neutron) "crude shell energies" of a nuclide with Z protons and N neutrons, $P_{\rm crude}(Z, N)$ ($Q_{\rm crude}(Z, N)$), in the following way:

1. Perform the Thomas-Fermi calculations as in Chapter 4 and obtain the nucleon distributions $n_{\rm n}(r)$ and $n_{\rm p}(r)$.
2. Calculate SP potentials $U(r)$, $V_{\rm LS}(r)$ and $V_{\rm C}(r)$ with $n_{\rm n}(r)$ and $n_{\rm p}(r)$.
3. Solve the Schrödinger equation (5.1a) (or (5.1b)) and obtain the SP energies $e_{\rm SP}$.
4. Calculate the total energy of n protons (neutrons) occupying the lowest SP states. This energy is denoted by $P_{\rm SP}(n; Z, N)$ ($Q_{\rm SP}(n; Z, N)$).
5. Calculate the total energy of n protons (neutrons) put in the SP potential $U(r)+V_{\rm C}(r)$ ($U(r)$) in the Thomas-Fermi approximation. This energy is denoted by $P_{\rm TF}(n; Z, N)$ ($Q_{\rm TF}(n; Z, N)$).
6. The differences $P_{\rm SP}(n; Z, N) - P_{\rm TF}(n; Z, N)$ ($Q_{\rm SP}(n; Z, N) - Q_{\rm TF}(n; Z, N)$) still include, in addition to shell effects, energies which can be represented by a smooth function of n as shown in Fig. 5-1. Then, approximate this smooth function by

$$g_{\rm i}(n; Z, N) = c_{\rm i1}(Z, N)\, n + c_{\rm i2}(Z, N)\, n^{4/3} + c_{\rm i3}(Z, N)\, n^2 \,. \qquad ({\rm i=n,p}) \qquad (5.13)$$

The values of the parameters $c_{\rm i1}(Z, N)$, $c_{\rm i2}(Z, N)$ and $c_{\rm i3}(Z, N)$ are chosen for each nuclide.

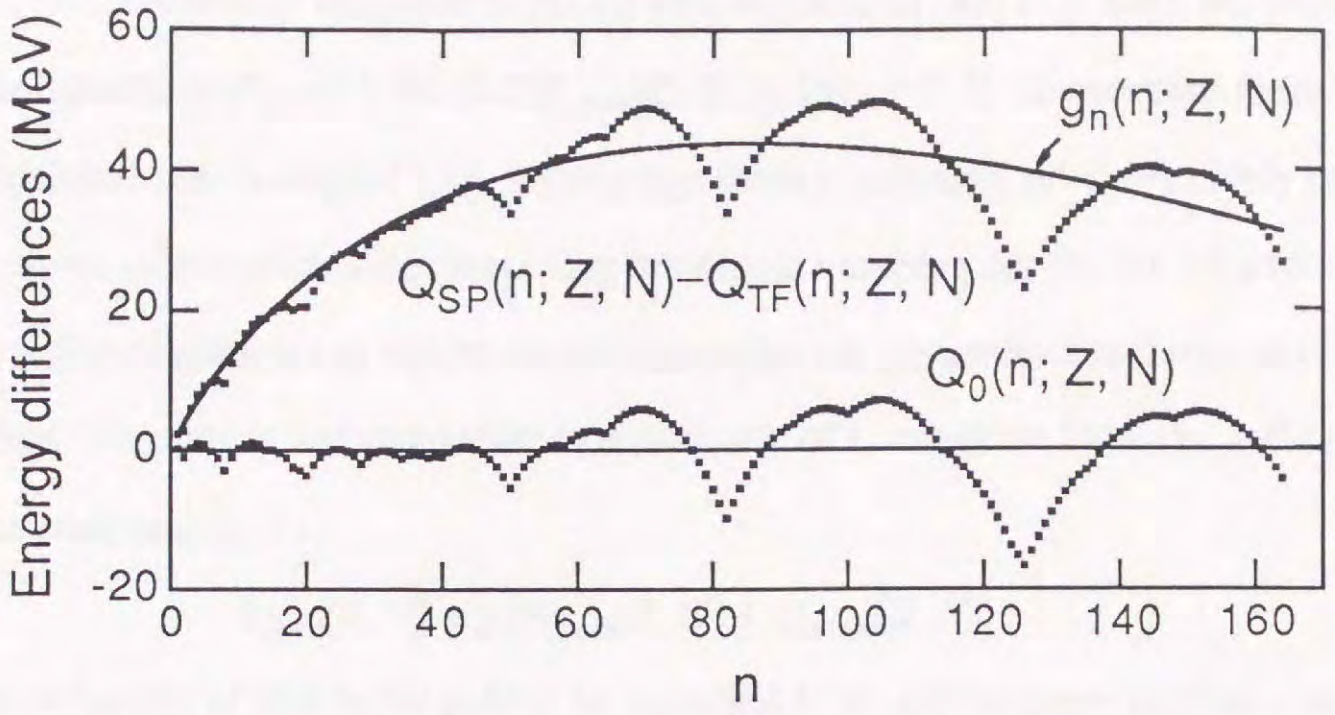

Fig. 5-5. Subtraction of residual smooth energies in the case of the neutron shell energy in ^{208}Pb obtained with model I.

7. Calculate the energy differences

$$P_0(n; Z, N) = P_{SP}(n; Z, N) - P_{TF}(n; Z, N) - g_p(n; Z, N) \quad \text{for protons,} \quad (5.14a)$$

and

$$Q_0(n; Z, N) = Q_{SP}(n; Z, N) - Q_{TF}(n; Z, N) - g_n(n; Z, N) \quad \text{for neutrons.} \quad (5.14b)$$

These differences are the results of subtraction of smooth parts from $P_{SP}(n; Z, N)$ and $Q_{SP}(n; Z, N)$.

8. Define the crude shell energies for protons and neutrons respectively as

$$P_{crude}(Z, N) = P_0(Z; Z, N), \quad (5.15a)$$

and

$$Q_{crude}(Z, N) = Q_0(N; Z, N). \quad (5.15b)$$

The above method has been simplified from the original one proposed by TTY in the following two points:

(i)We neglect the spin-orbit potential in calculating $P_{TF}(n; Z, N)$ and $Q_{TF}(n; Z, N)$.

(ii) We choose the values of the coefficients in $g_i(n; Z, N)$ independently for each nuclide while TTY and UTTKY expressed these coefficients as smooth functions of Z and N.

These simplifications are unlikely to change the results appreciably.

For nearly spherical nuclides with $40 \leq A \leq 233$ (see Fig. 5-6), we show the crude shell energies $P_{\text{crude}}(Z, N)$ and $Q_{\text{crude}}(Z, N)$ in Fig. 5-7. If we compare them with the empirical shell energies [30], we see that these crude shell energies nicely reproduce the features of empirical ones including the magic numbers 20, 28, 50, 82 and 126 except that the magnitudes of the crude shell energies are about twice as large as the empirical ones. We correct this overestimation with use of a reduction factor μ, and approximate the shell energy to

$$E_{\text{shell}}(Z, N) = \mu \left[P_{\text{crude}}(Z, N) + Q_{\text{crude}}(Z, N) \right]. \tag{5.16}$$

Introduction of this factor μ may be regarded as an approximate inclusion of the effects of configuration mixing. With this shell energy, the nuclear mass in our model is given by

$$M_{\text{model}}(Z, N) = M_{\text{TF}}(Z, N) + E_{\text{shell}}(Z, N), \tag{5.17}$$

where $M_{\text{TF}}(Z, N)$ is the mass in the Thomas-Fermi approximation. The value of μ is determined so that the differences between the calculated masses $M_{\text{model}}(Z, N)$ and the experimental masses $M_{\text{exp}}(Z, N)$ [27] show as little staggering as possible as a function of Z and N. The deviations of $M_{\text{TF}}(Z, N)$ and $M_{\text{model}}(Z, N)$ from $M_{\text{exp}}(Z, N)$ are shown in Fig. 5-8 for model I with the best value of μ(=0.45), and the root-mean-square deviations are given in Table 5-2. As seen in Fig. 5-8 and Table 5-2, the inclusion of shell energies substantially improves the calculated masses. The remaining deviations are due not only to the inaccuracies of the shell energies but also to those of $M_{\text{TF}}(Z, N)$. The simple relation between the crude shell energies and the final shell energies (Eq. (5.16)) is acceptable when the nuclides are limited, e.g., to those in Fig. 5-6. TTY and UTTKY who treated essentially all the nuclides used a more complicated relation to take into account the effects of pairing and deformation. However, our simple method will be a good first approximation for the study of the nuclei in a neutron star for the following reason. In the region of the neutron-star crust where the shape change is expected, the proton number of a nucleus or a cell is in the range 30-50 as shown in chapter 4. This range is included in Fig. 5-6. In the adjacent excluded region, the nuclei are deformed and the deformation effects must be taken into account. However, the

deformation seems to occur as a cooperative phenomenon between proton and neutron shell structures. As will be shown in the next section, the neutron shell energies are very small compared with the proton shell energies in the nuclei treated in this paper. Therefore, strong deformation (deviation from sphere or deviation from cylinder) is unlikely and we adopt Eq. (5.16) as a first approximation.

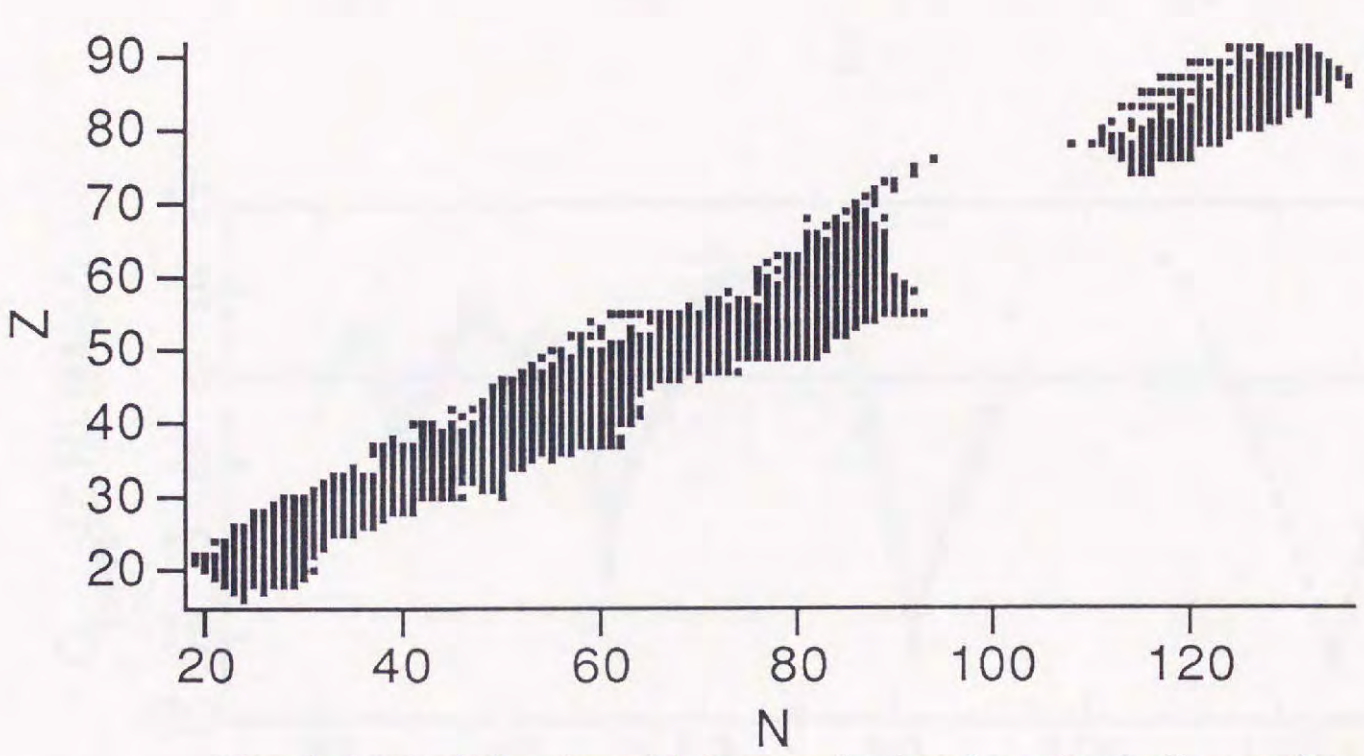

Fig. 5-6. Nuclides for which we calculated crude shell energies.

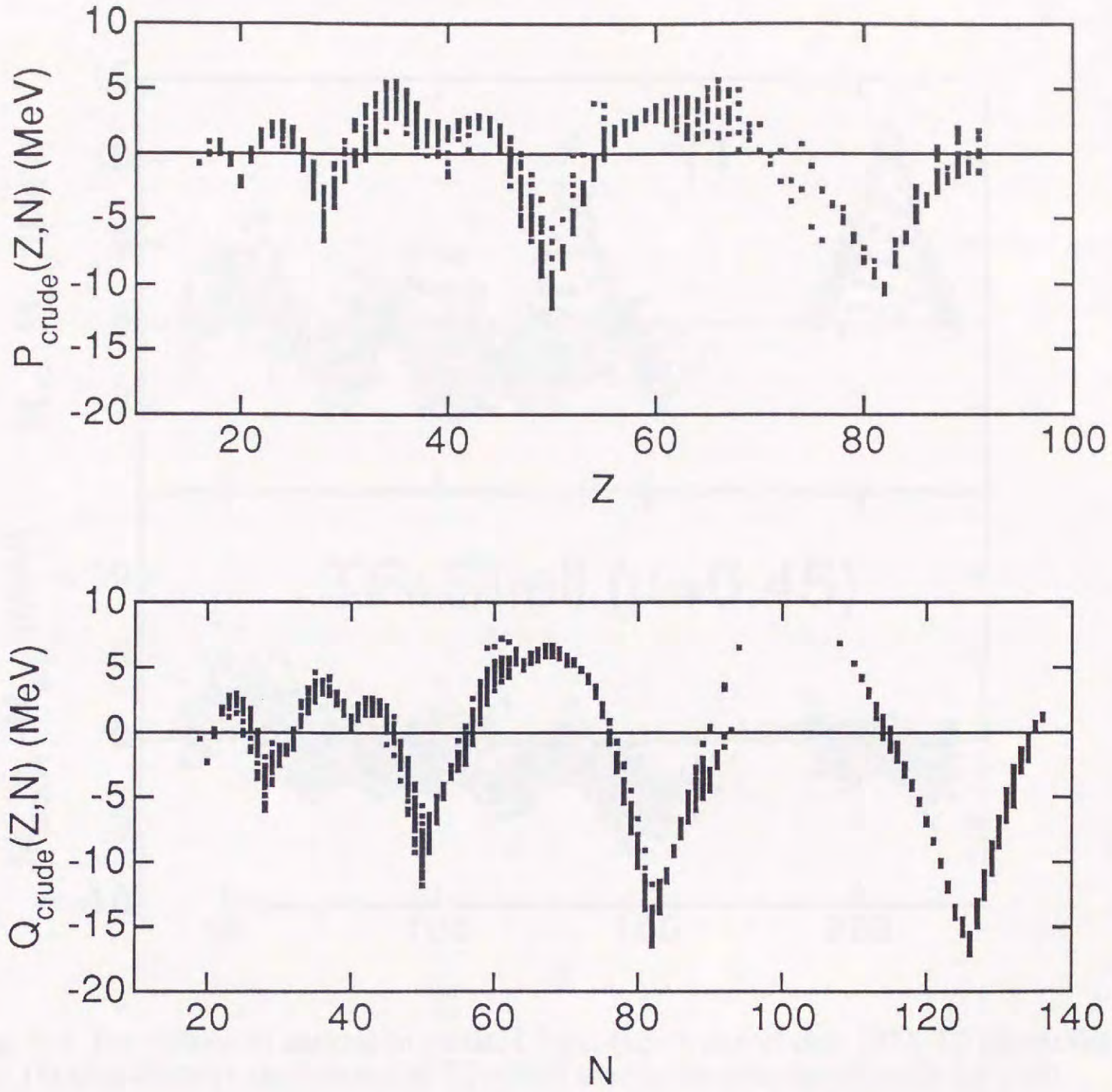

Fig. 5-7. Proton (neutron) crude shell energies $P_{crude}(Z, N)$ ($Q_{crude}(Z, N)$) in model I.

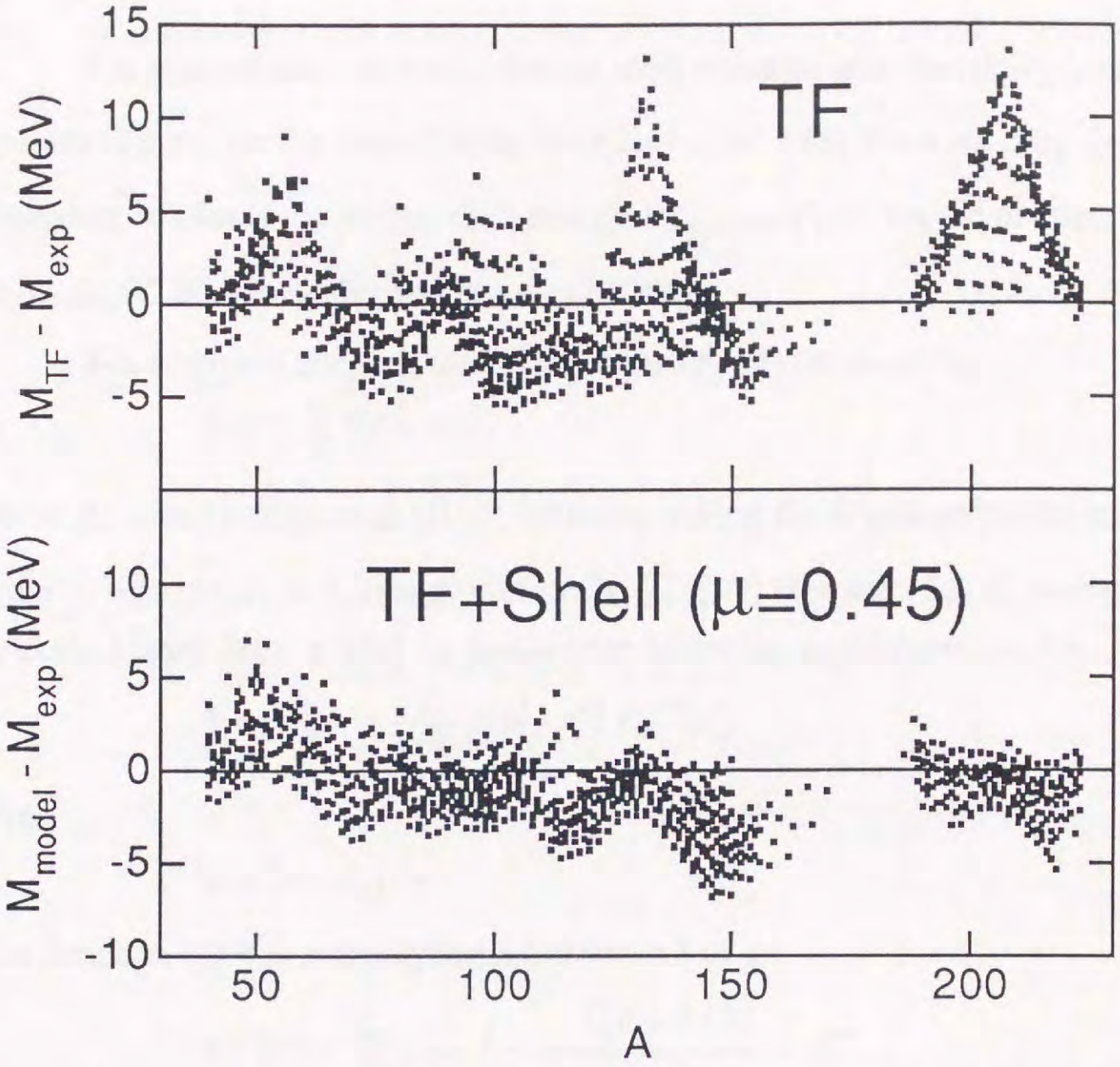

Fig. 5-8. Deviations of masses in model I from experimental data [27]. TF stands for the Thomas-Fermi calculation and TF+Shell means the calculation with the shell energies.

Table 5-2

Root-mean-square deviations (in MeV) of calculated masses from experimental data[27]. In the last column I(ST4), shell energies of model I are calculated with Strutinsky's method. TF stands for the Thomas-Fermi calculation and TF+Shell means the calculation with the shell energies

	model			
	I	II	III	I(ST4)
μ	0.45	0.45	0.45	0.50
TF	3.62	3.53	4.18	3.62
TF+shell	2.28	2.19	3.39	2.33

5.2.2. Prescription 2 (Strutinsky's method)

For comparison, we also calculate shell energies with Strutinsky's method [39]. Specifically we use the prescription described in ref. [40]. Here we only describe the procedure to obtain the proton shell energy $P_{\text{Strutinsky}}(Z, N)$ but the neutron shell energy $Q_{\text{Strutinsky}}(Z, N)$ can be derived in a similar way.

For a normal nucleus, the SP level density $\eta(e)$ is given by

$$\eta(e) = \sum_i \delta\left(e - e^i_{\text{SP}}\right), \tag{5.18}$$

where the sum is taken over all the SP states, taking the degeneracy into account. In order to obtain a smooth energy part of $P_{\text{SP}}(n; Z, N)$ (see sect. 5.2.1), we construct a smoothed level density $\tilde{\eta}(e)$ by making the following replacement in Eq. (5.18):

$$\delta\left(e - e^i_{\text{SP}}\right) \rightarrow \frac{1}{\gamma\sqrt{\pi}} \exp\left(-u_i^2\right)\ L_S^{1/2}\left(u_i^2\right) \tag{5.19}$$

with

$$u_i = \left(e - e^i_{\text{SP}}\right) / \gamma\,. \tag{5.20}$$

The function $L_S^{1/2}(x)$ is a polynomial of order S in x:

$$L_S^{1/2}(x) = \sum_{m=0}^{S} \frac{1}{(S-m)!\ m!} \frac{\Gamma(S+3/2)}{\Gamma(m+3/2)} (-x)^m, \tag{5.21}$$

where $\Gamma(S)$ is the Γ-function. We extend the e-space from $-\infty$ to ∞. This replacement (5.19) preserves not only the normalization of each level but also all the moments of orders ranging from 0 to 2S+1 for the distribution of the delta functions. The function $L_S^{1/2}(x)$ is often called the curvature function of $(2S)$th order; we use S=4. With the above replacement, the smoothed level density can be written as

$$\tilde{\eta}(e) = \frac{1}{\gamma\sqrt{\pi}} \sum_i \exp\left(-u_i^2\right)\ L_S^{1/2}\left(u_i^2\right), \tag{5.22}$$

with u_i defined in Eq. (5.20). Since we extend the e-space from $-\infty$ to ∞, the smoothed total proton energy $\tilde{P}(n; Z, N)$ with n protons is defined by

$$\tilde{P}(n; Z, N) = \int_{-\infty}^{\tilde{\lambda}} \tilde{\eta}(e)\, e\, de \tag{5.23}$$

with

$$n = \int_{-\infty}^{\tilde{\lambda}} \tilde{\eta}(e)\, de\,. \tag{5.24}$$

Then the proton shell energy for a normal nucleus in Strutinsky's method is given by

$$P_{\text{Strutinsky}}(Z, N) = P_{\text{SP}}(Z, Z, N) - \tilde{P}(Z; Z, N)\,. \tag{5.25}$$

In the cases of the cylindrical and slab-shape nuclei, the level densities $\eta(e)$ are continuous and we have to modify the above procedure. With the continuous level density $\eta(e)$ we define a smoothed level density defined as

$$\tilde{\eta}(e) = \frac{1}{\gamma\sqrt{\pi}} \int de'\, \eta(e') \exp\left(-\left(\frac{e-e'}{\gamma}\right)^2\right) L_S^{1/2}\left(\left(\frac{e-e'}{\gamma}\right)^2\right). \tag{5.26}$$

This definition is an extention of Eq. (5.22) and also applicable to the case of spherical nuclei.

We choose the width γ to be equal to the spacing between e_{SP}'s of the two least bound s-waves for spherical nuclei, between e_{xy}'s of the two least bound levels with l_z=0 for cylindrical nuclei, or between e_x's of the two least bound levels for slab-shape nuclei. For normal nuclei, we have obtained neutron and proton shell energies similar to those in Fig. 5-7. The magnitudes of the above shell energies are also about twice as large as the empirical ones. Therefore we redefine the shell energy as in sect. 5.2.1:

$$E_{\text{shell}}(Z, N) = \mu\left[P_{\text{Strutinsky}}(Z, N) + Q_{\text{Strutinsky}}(Z, N)\right]. \tag{5.27}$$

We also use Eq. (5.17) to define $M_{\text{model}}(Z, N)$ in the present case. As shown in Table 3 the deviation of $M_{\text{model}}(Z, N)$ from $M_{\text{exp}}(Z, N)$ are comparable to that calculated with prescription 1 in sect. 5.2.1.

In closing this section a note is added on the style of presenting functions of Z and N. When we treat nuclei at high matter densities as in this paper, we cannot specify Z and N beforehand; they are known as results of calculations. For this reason and also for simplicity we do not write the arguments Z and N explicitly in the following.

5.3. Shell energies of the nuclei in the inner crust of a neutron star

At the densities in the inner crust of a neutron star, most neutrons occupy continuum states. Therefore, neutron shell effects are expected to be much smaller than proton shell effects. In order to confirm it, we have calculated the neutron shell energies for slab-shape nuclei. For simplicity, we consider an equivalent square-well potential $U_{\rm sq}(|x|)$ chosen such that this potential can bind, in the Thomas-Fermi approximation, the same number of neutrons with the same total energy as the potential $U(|x|)$ described in sect. 5.1. Then, we solve the one-dimensional Schrödinger equation:

$$\left\{-\frac{\hbar^2}{2m_{\rm n}}\frac{{\rm d}^2}{{\rm d}x^2}+U_{\rm sq}(|x|)\right\}\varphi(x)=e_x\,\varphi(x)\,. \tag{5.28}$$

Since the nuclei form a one-dimensional lattice, we use the periodic boundary condition,

$$\varphi(a/2)=\exp(ik_x a)\varphi(-a/2)\,,\quad \varphi'(a/2)=\exp(ik_x a)\varphi'(-a/2)\,. \tag{5.29}$$

Here, a is the lattice constant which is the distance between the central planes of the neighboring nuclei. With this periodic boundary condition, we obtain energy bands as shown in Fig. 5-9. There are energy gaps at integral $k_x a/\pi$ values, but some of them can hardly be seen in this figure especially at high energies. Note that the energy bands for the bound neutrons are very narrow. From these band energies supplemented by the kinetic energies in y and z directions as in Eq. (5.12b), we extract neutron crude shell energies by the method described in sect. 5.1 with the following modification on Eq. (5.13). This modification is necessary since we have to treat much more particles (≈1000 neutrons) and the shell effects are dominant at small n values. In order to represent the behavior of $g_{\rm n}(n)$ ($g_{\rm n}(n;Z,N)$ in Eq. (5.13)) at small n values accurately, we add two terms in lower powers of n as

$$g_{\rm n}(n)=c'_{\rm n1}\,n^{1/3}+c'_{\rm n2}\,n^{2/3}+c'_{\rm n3}\,n+c'_{\rm n4}\,n^{4/3}+c'_{\rm n5}\,n^{2}\,. \tag{5.30}$$

The resultant energies per cell after subtraction of smooth energies (Eq. (5.14b)) are shown in Fig. 5-10. At the average nucleon number density $n_{\rm b}$=0.074 fm^{-3}, there are 1073 neutrons per cell and, reading the corresponding energy value from Fig. 5-10, we

see that the neutron crude shell energy per cell is 0.03 MeV, while the proton crude shell energy at this density amounts to 0.24 MeV as shown later.

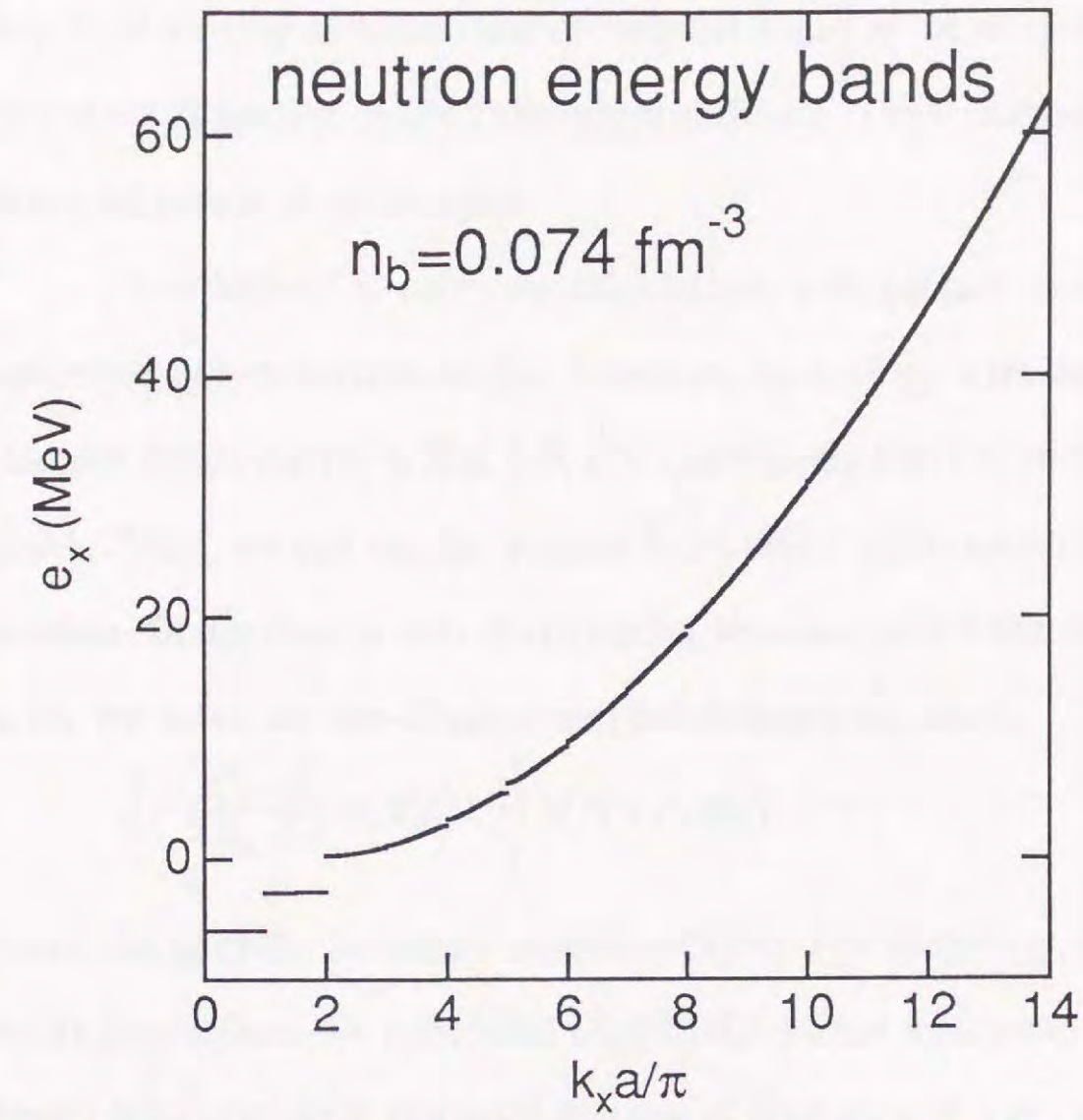

Fig. 5-9. Neutron SP energy for the slab-shape nucleus at the average nucleon number density n_b=0.074 fm^{-3} in model I. In this figure, the zero energy is taken equal to the potential energy at the edges of the cell ($U_{sq}(|\pm a/2|)$).

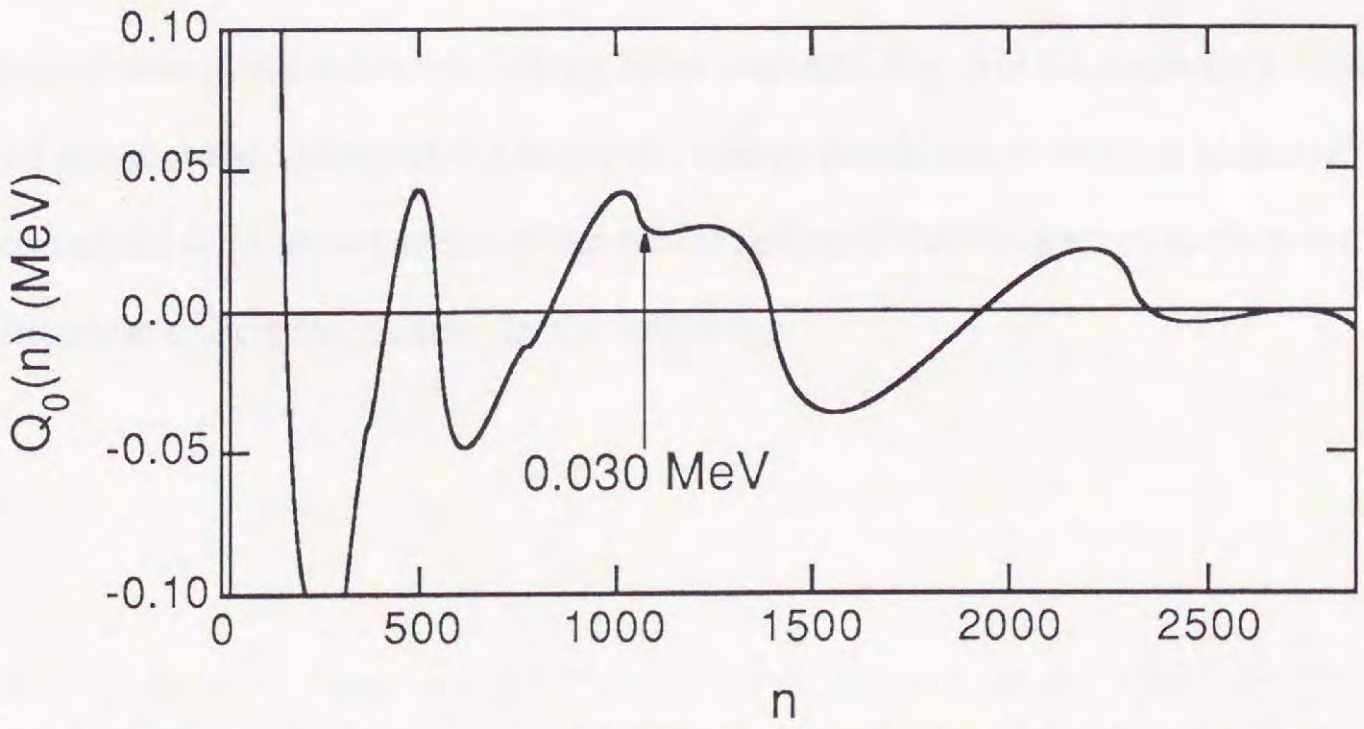

Fig. 5-10. Energy difference $Q_0(n)$ (Eq. (5.14b)) for the slab-shape nucleus at n_b=0.074 fm^{-3} in model I. The arrow indicates the position of the predicted neutron number.

Generally, the neutron shell energies for slab-shape nuclei are one order of magnitude smaller than the proton shell energies. Similar smallness of the neutron shell energies is expected also for spherical and cylindrical nuclei at the densities of interest, although actual confirmation seems to be rather difficult. Thus, in the following, we only consider proton shell energies.

It is difficult to carry out calculations with periodic boundary conditions for spherical and cylindrical nuclei. However, by analogy with the narrow low-lying neutron bands shown in Fig. 5-9, it is quite likely that the bound protons lie in narrow bands. Then, we can use the Wigner-Seitz cell method to calculate SP energies for protons. In the case of slab-shape nuclei we can confirm the above statement. To begin with, we solve the one-dimensional Schrödinger equation,

$$\left\{-\frac{\hbar^2}{2m_{\mathrm{p}}}\frac{d^2}{dx^2}+U_{\mathrm{sq}}(|x|)\right\}\varphi(x)=e_x\,\varphi(x), \tag{5.31}$$

under the periodic boundary condition (5.29). For simplicity, we use, in Eq. (5.31), an equivalent square-well potential $U_{\mathrm{sq}}(|x|)$ for proton which can bind, in the Thomas-Fermi approximation, the same number of protons with the same total energy as the potential $U(r)+V_{\mathrm{C}}(r)$. Table 5-4 shows the highest and lowest SP energies of each energy band relative to the potential energy at the edges of a cell ($U_{\mathrm{sq}}(|\pm a/2|)$). With a square-well potential, the cases $k_x=2(n-1)\pi/a$ and $(2n-1)\pi/a$ give the highest and the lowest energies for the i-th energy band (see also Fig. 5-9 for neutrons). From Table 5-4 we see that the widths of the occupied energy bands are so narrow (order of 1 keV) comapred with the spacings of the bands (order of MeV) that we neglect the band-structure effects for protons in the following.

Table 5-4

The highest and the lowest proton single-particle energies e_x for each energy band with an eqivalent SP potential in model I. The potential energy at the edges of the cell ($U_{sq}(|\pm a/2|)$) is -62.9948 MeV at n_b=0.07 fm^{-3} and it is -65.4139 MeV at n_b=0.074 fm^{-3}. The protons occupy the lowest one or two bands at the densities listed in this table.

	boundary conditions	
	k_x=0	k_x=π/a
n_b (fm^{-3})	e_x (MeV)	e_x (MeV)
0.07	-63.2291	-62.9560
	-67.8213	-67.8228
	-71.5098	-71.5098
0.074	-65.7617	-65.4177
	-69.7482	-69.7558
	-72.8928	-72.8924

Furthermore, proton SP energies do not depend much on a choice of the boundary condition. We calculate SP energies in a slab-shape nucleus (or cell) under three different boundary conditions with the SP potential discussed in sect. 5.1. These energies are calculated from the one-dimensional Schrödinger equation:

$$\left\{-\frac{\hbar^2}{2m_p}\frac{d^2}{dx^2} + U(|x|) + V_C(|x|)\right\}\varphi(x) = e_x\,\varphi(x)\ , \tag{5.32}$$

in which the absolute value of $V_C(|x|)$ is chosen so that it vanishes at the edges of the cell (at x=$\pm a/2$). The spin-orbit potential is not included in Eq. (5.32) in accordance with the argument in sect. 5.1. In Table 5-5, we show the SP energies obtained with the following three different boundary conditions:

$$\varphi'(\pm a/2) = 0, \tag{5.33a}$$

$$\varphi(\pm a/2) = 0, \tag{5.33b}$$

$$\varphi(\pm\infty) = 0. \tag{5.33c}$$

In the case of the boundary condition (5.33c), we have used a potential outside the cell as

$$U(|x|) + V_C(|x|) = U(|a/2|) \qquad \text{for } |x| > a/2, \tag{5.34}$$

instead of the periodic potential.

Table 5-5
The x-component of the single-particle energies e_x for slab-shape nuclei under different boundary conditions in model I. For the boundary conditions a and b, $x=\pm a/2$ corresponds to the cell edges. The protons occupy the lowest one or two bands at the densities listed in this table

	boundary conditions		
	a ($\varphi'(\pm a/2)=0$)	b ($\varphi(\pm a/2)=0$)	c ($\varphi(\pm\infty)=0$)
n_b (fm^{-3})	e_x (MeV)	e_x (MeV)	e_x (MeV)
0.07	-63.295	-63.058	-63.153
	-67.278	-67.276	-67.276
	-72.292	-72.292	-72.292
0.074	-65.875	-65.511	-65.658
	-69.279	-69.268	-69.271
	-73.590	-73.590	-73.590

As shown in Table 5-5, the SP energies under different boundary conditions do not differ much from each other. Although the SP potentials are not the same, the width of each energy band in Table 5-4 is approximately equal to the corresponding difference between the energies obtained with the boundary conditions (5.33a) and (5.33b) in Table 5-5. At lower densities the width of each energy band for the slab-shape nucleus becomes narrower. Then, for simplicity, we use the boundary condition for the slab-shape nucleus as Eq. (5.33a) in the following. For spherical and cylindrical nuclei we can also expect that the SP energies do not depend much on the boundary condition, and adopt the Wigner-Seitz cell approximation. We denote the radius of the Wigner-Seitz cell by R_C and use the following conditions for the spherical (cylindrical) nucleus

$$\frac{\partial}{\partial r}\psi(R_C)=0 \quad \left(\frac{\partial}{\partial r}\varphi(R_C)=0\right) \qquad \text{for even } l\ (l_Z), \tag{5.35a}$$

and

$$\psi(R_C)=0 \quad (\varphi(R_C)=0) \qquad \text{for odd } l\ (l_Z). \tag{5.35b}$$

For a spherical nucleus these conditions are the same as the one used by Negele and Vautherin for a neutron-star matter calculation [19], and as the one of two conditions used by Bonche and Vautherin for a supernova-matter calculation [41]. With the

present boundary conditions, we have discrete eigenvalues for e_{SP} for spherical nuclei, e_{xy} for cylindrical nuclei and e_x for slab-shape nuclei.

In Fig. 5-11 we show proton SP energies for spherical nuclei relative to that of the $2p_{1/2}$ state as functions of the average matter density. Note that the nucleus has approximately 40 protons in this density range (Fig. 4-8) filling up to a level around the $2p_{1/2}$ level. As the average matter density increases, the average level spacings and the spin-orbit splittings decrease appreciably. In particular the latter become very small at the density $n_b \approx 0.06$ fm^{-3} ($\rho \approx 1\times10^{14}$ g/cm^3) where the cylindrical nucleus becomes stable in the Thomas-Fermi approximation. This decrease of the spin-orbit splittings is understood from decrease of the local density gradients which cause the spin-orbit forces (see also Fig. 5-4). In Fig. 5-12 we show the energy differences $P_0(n)$ ($P_0(n; Z, N)$ in Eq. (5.14a)) for n protons to be in a cell. This figure shows that, as the matter density increases, the amplitude of the energy oscillation due to the shell structure decreases. It also shows that the rapid decrease of the spin-orbit splittings changes the magic number; for example, the number 50 is a strong magic number at n_b=0.01 fm^{-3} but it is only a moderate submagic number at n_b=0.06 fm^{-3}, transferring its magicity to the number 40. Including this change of magic number, our results are in good agreement with the Hartree-Fock calculation by Negele and Vautherin [19] except that our models give somewhat narrower level spacings as shown in Fig. 5-11.

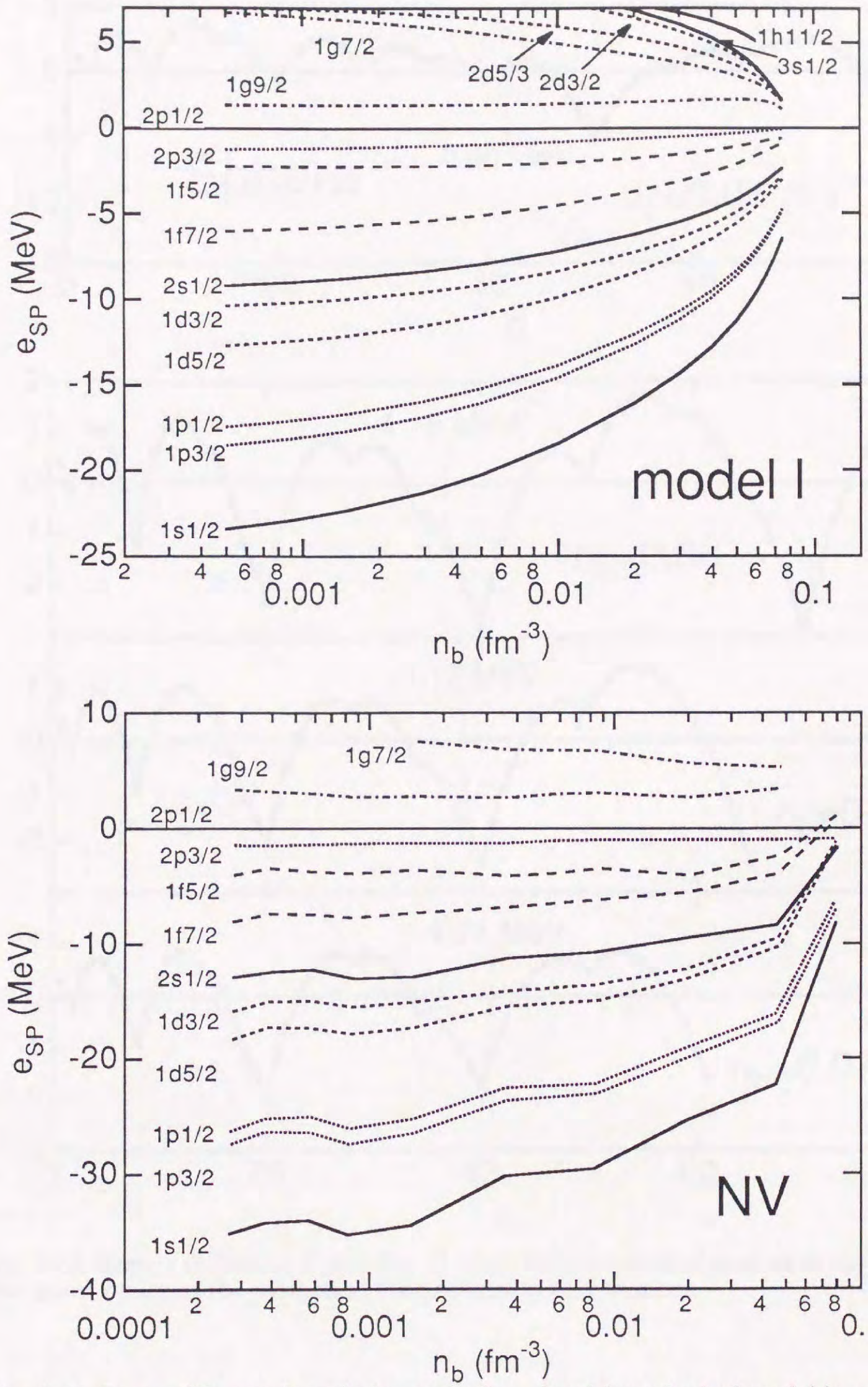

Fig. 5-11. Proton SP energies relative to the $2p_{1/2}$ level for spherical nuclei in model I (upper) and in the Hartree-Fock calculation by Negele and Vautherin [19] (lower).

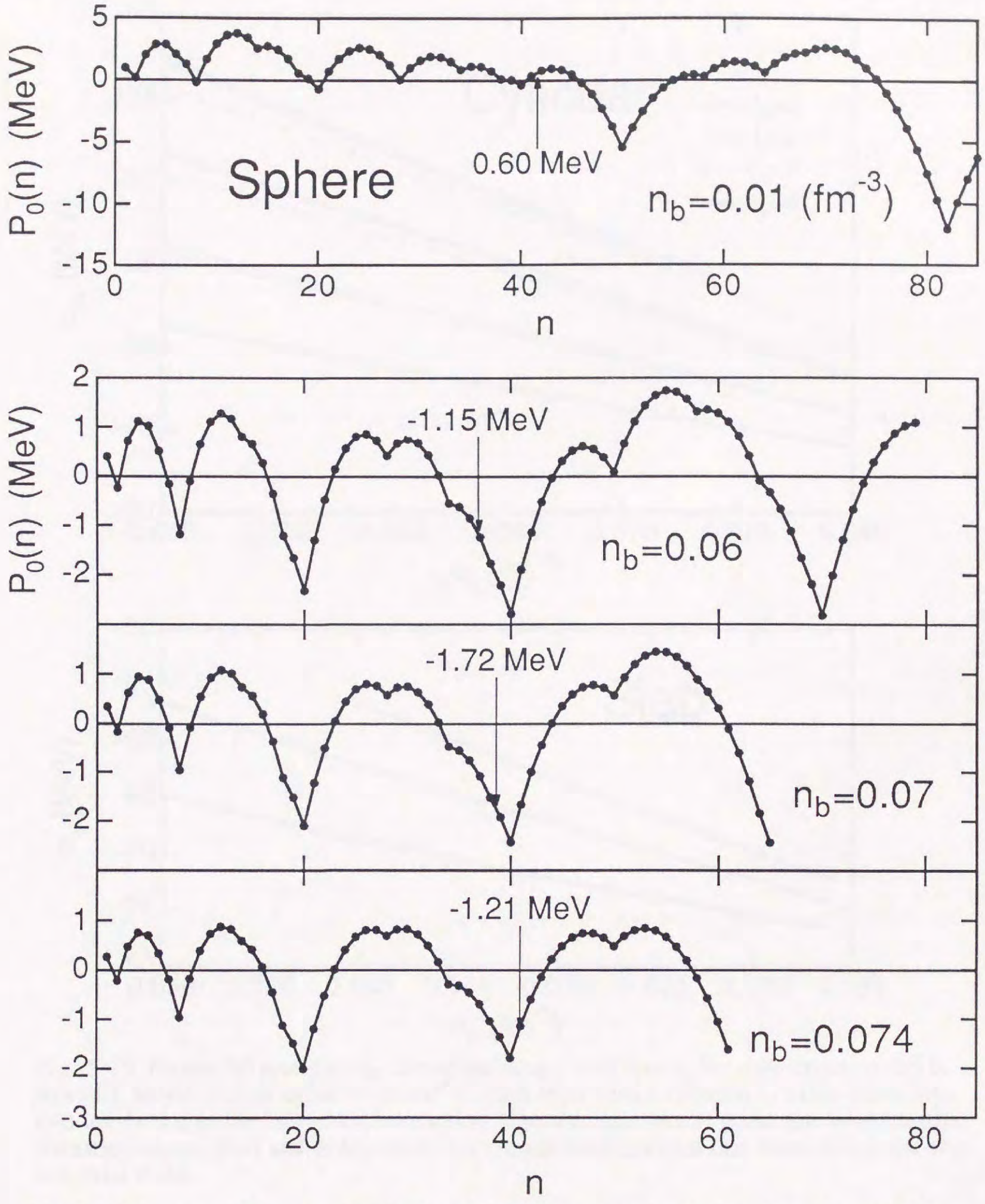

Fig. 5-12. Energy difference $P_0(n)$ (Eq. (5.14a)) for the spherical nucleus in model I. The arrow indicates the position of the predicted proton number.

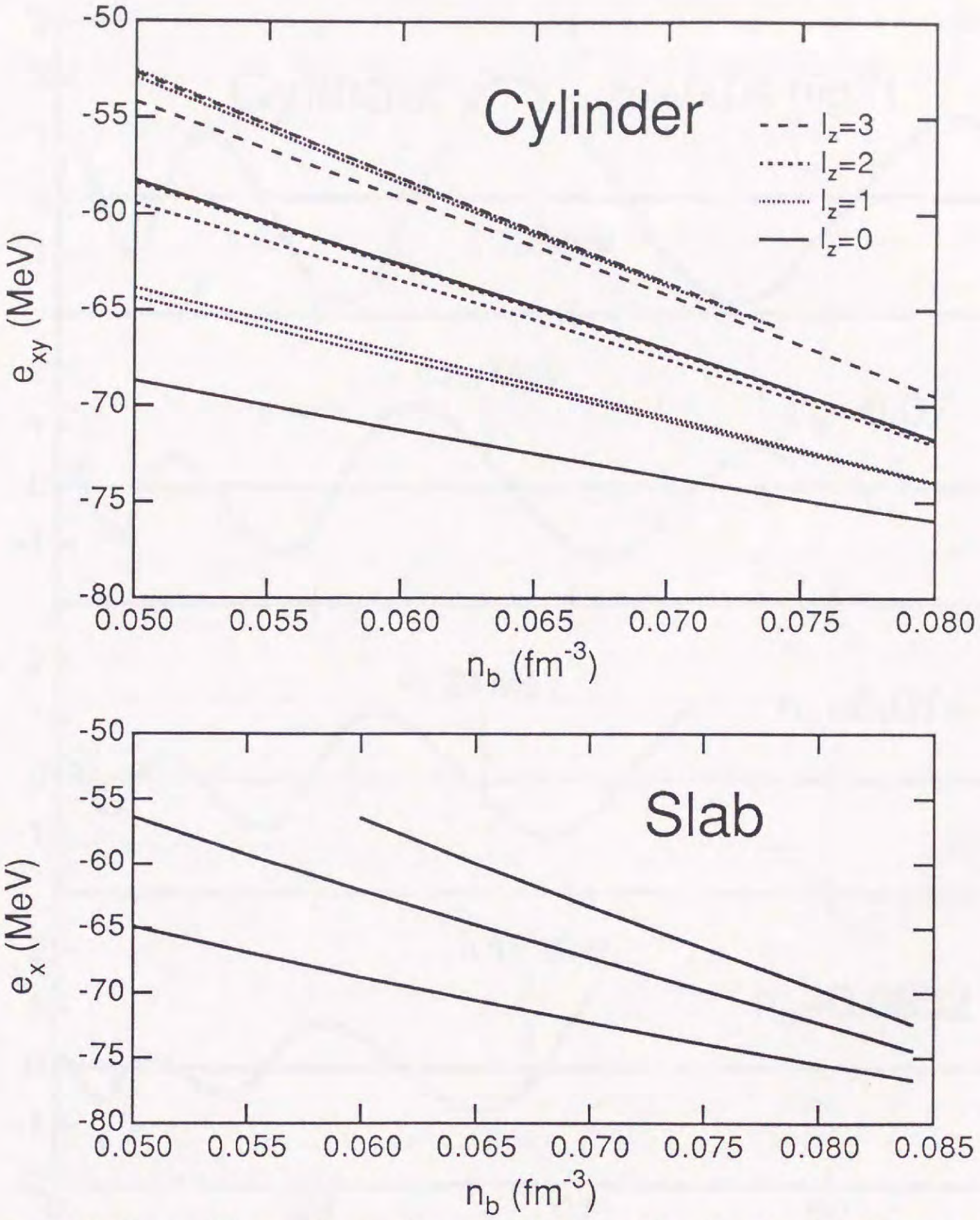

Fig. 5-13. Proton SP energies e_{xy} for cylindrical nuclei and e_x for slab-shape nuclei in model I. In the case of cylindrical nuclei, each state with a nonzero l_z value splits into two levels due to the spin-orbit interaction. The terminations of some top levels at high densities (upper box) and at low densities (lower box) indicate that these levels become unbound there.

In Fig. 5-13 we show the SP energies e_{xy} for cylindrical nuclei and e_x for slab-shape nuclei as functions of the matter density. The SP energies for these nuclei also show appreciable decrease of spacings with increase of the density. For cylindrical nuclei, the spin-orbit splittings are not very large, and rapidly decrease as the density increases.

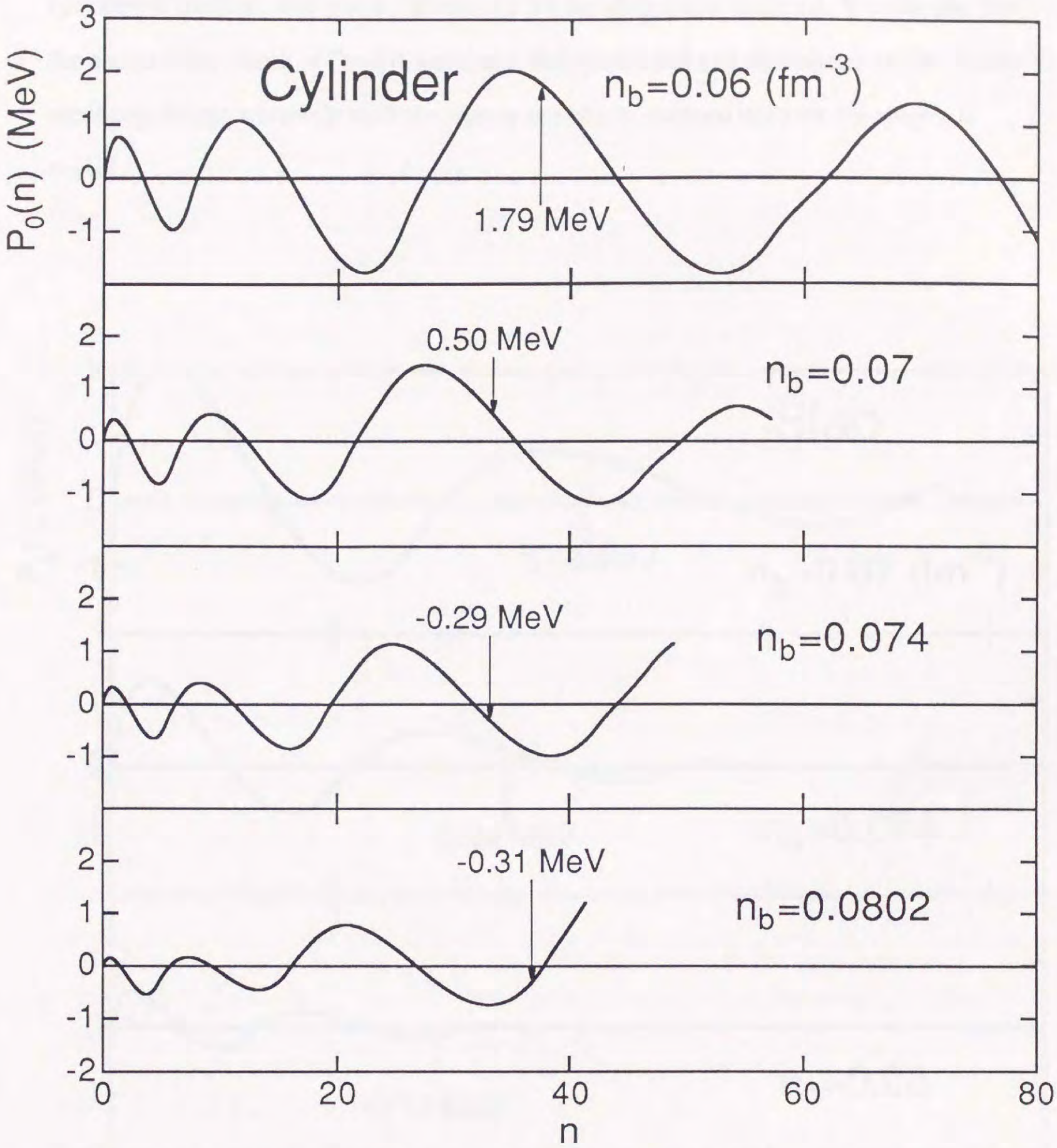

Fig. 5-14. Energy difference $P_0(n)$ (Eq. (5.14a)) for the cylindrical nucleus in model I. The arrow indicates the position of the predicted proton number.

In Figs. 5-14 and 5-15 we show $P_0(n)$ for the cylindrical and slab-shape nuclei, respectively. For these nuclei $P_0(n)$ are smooth functions of n unlike that for the spherical nucleus because the SP energies for these shapes are continuous; this continuity results from the presence of the directions of free motion (z direction for the

cylindrical nucleus, and y and z directions for the slab-shape nucleus). We can see that there also exist a kind of "magic numbers" for cylindrical and slab-shape nuclei. These numbers change smoothly with the matter density in contrast to those for spherical nuclei.

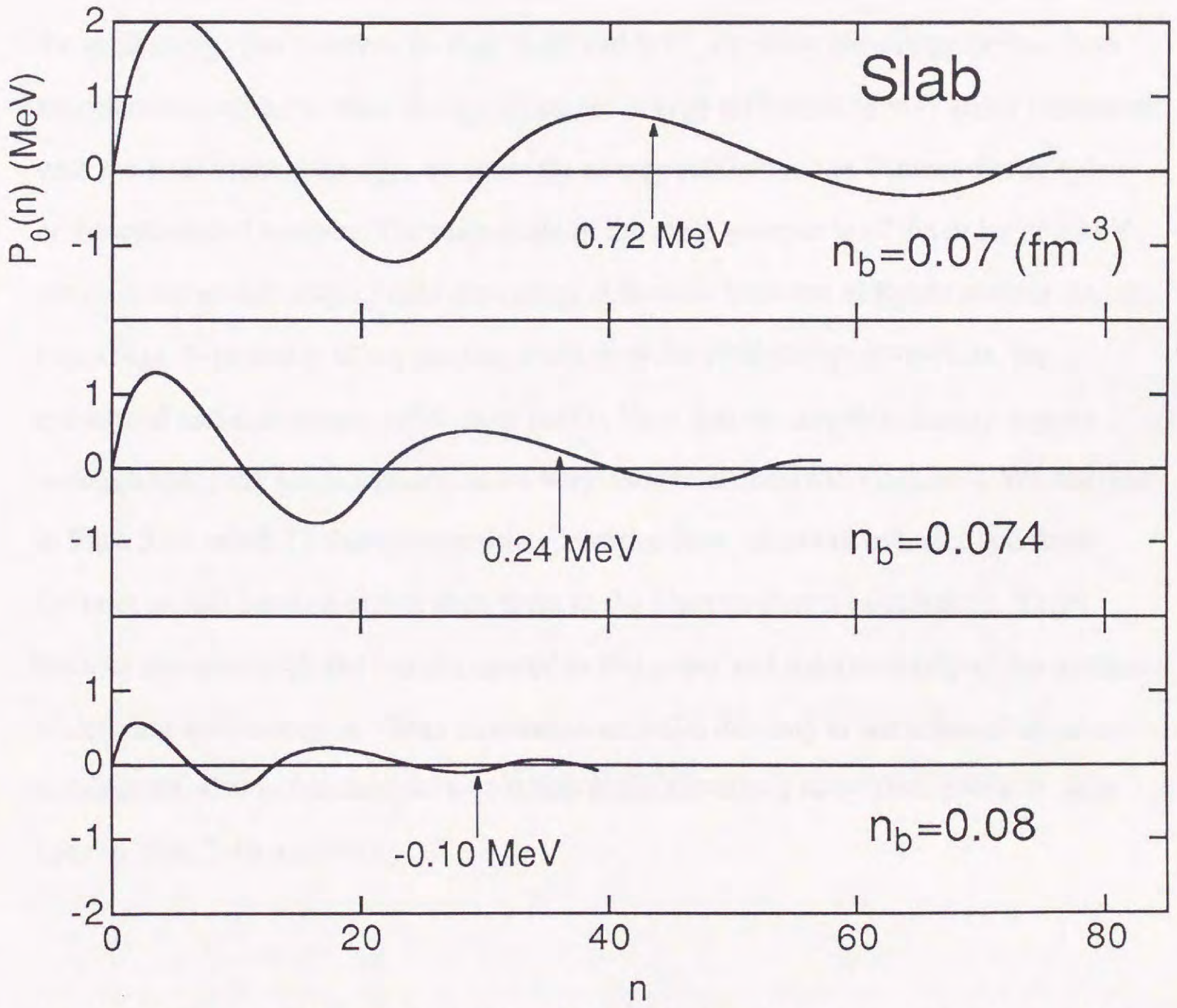

Fig. 5-15. Energy difference $P_0(n)$ (Eq. (5.14a)) for the slab-shape nucleus in model I. The arrow indicates the position of the predicted proton number.

With the above energy difference $P_0(n)$ and the proton number $Z \equiv (Z_{TF})$ obtained in the Thomas-Fermi calculation, we get the crude shell energy, corresponding to Eq. (5.15a), as

$$P_{\text{crude}} = P_0(Z_{TF}). \tag{5.36}$$

We neglect the neutron shell energy and write the shell energy per cell as

$$E_{\text{shell}} = \mu P_{\text{crude}}, \tag{5.36}$$

in place of Eq. (5.16). By dividing it by the total nucleon number in a cell, we obtain the shell energy per nucleon. In Figs. 5-16 and 5-17, we show the energy per nucleon supplemented with the shell energy. Since the energy difference is very small compared with the total binding energy, we show the energy relative to the Thomas-Fermi value of the cylindrical nucleus. The magnitude of the shell energies is of the order of 1 keV which is somewhat smaller than the energy difference between different nuclear shapes. From Figs. 5-16 and 5-17 we see that, even with the shell energy correction, the cylindrical and slab-shape nuclei exist stably. Note that the unstable density regions accompanying the phase transitions are very narrow as shown in Chapter 4. We also see in Figs. 5-16 and 5-17 that the transition densities from sphere to cylinder and from cylinder to slab become higher than those in the Thomas-Fermi calculations. These features are seen in all the models treated in this paper and independently of the method of deriving shell energies. These statements are valid not only in the cases of optimum μ values but also in the cases of μ=1 which gives extremely large shell energies (thin lines in Figs. 5-16 and 5-17).

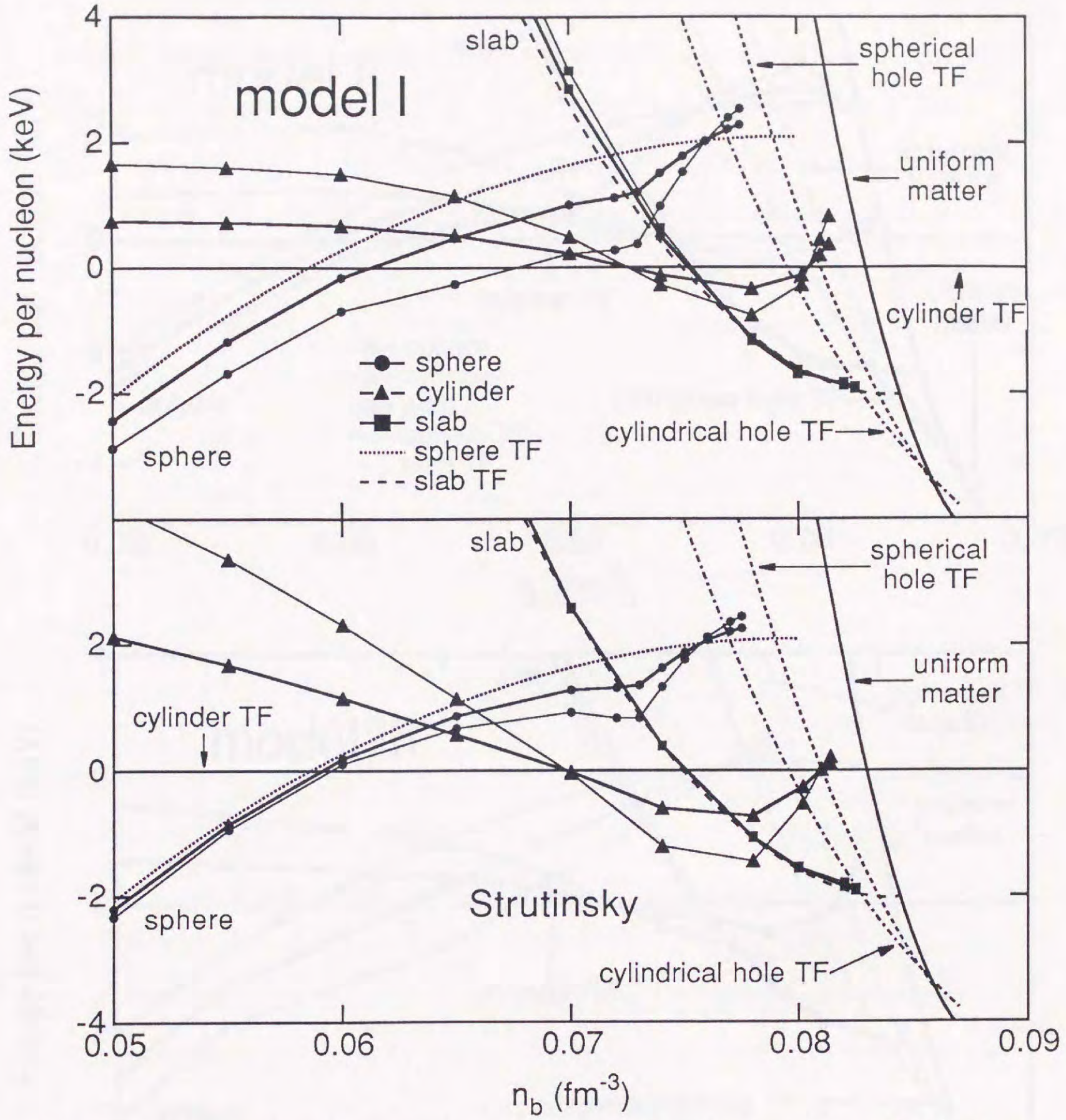

Fig. 5-16. Energy per nucleon relative to the Thomas-Fermi value of the cylindrical nucleus in model I. Shell energies are calculated with prescription 1 in sect. 5.2.1 (upper) and Strutinsky's method (lower). The thick lines correspond to the choice of the optimum μ values while the thin lines correspond to the choice of μ=1. TF stands for the Thomas-Fermi value.

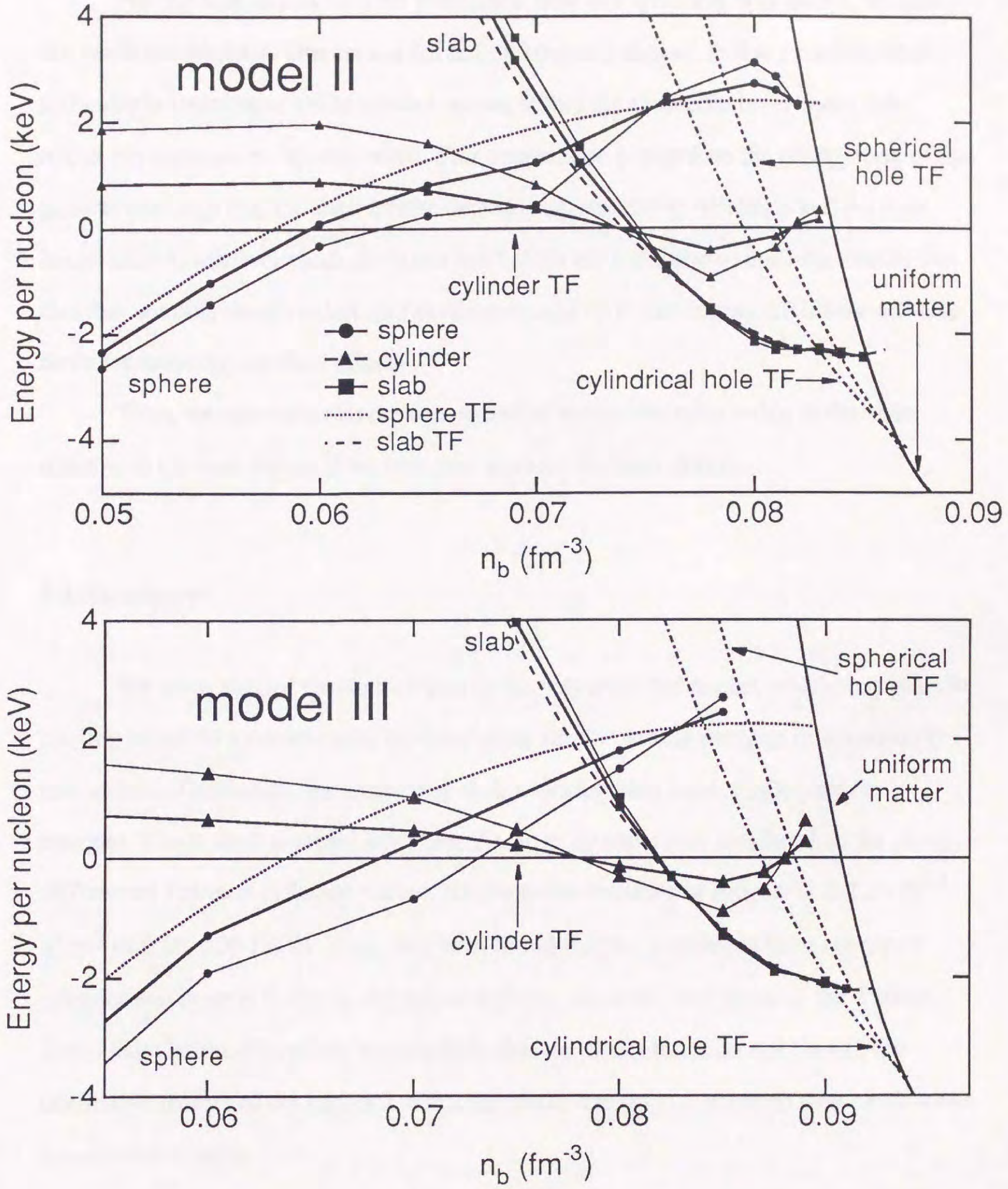

Fig. 5-17. Energy per nucleon relative to the Thomas-Fermi value of the cylindrical nucleus in models II and III. Shell energies are calculated with prescription 1 in sect. 5.2.1. The thick lines correspond to the choice of the optimum μ values while the thin lines correspond to the choice of μ=1. TF stands for the Thomas-Fermi value.

For the hole nuclei, i.e., the cylindrical hole and spherical hole nuclei, we have not made calculations. One reason for not making calculations is that a considerable difficulty is anticipated while another reason is that the shell effects for these hole nuclei are expected to be very small. This expectation is based on the observation of the general tendency that the shell effects decrease as the density increases and the hole nuclei exist at relatively high densities just before the transition to uniform matter. The fact that not only neutrons but also protons occupy up to continuous SP levels will also serve for reducing the shell effects.

Thus, we conclude that the non-spherical nuclei can exist stably in the same order as in Chapter 4 even if we take into account the shell effects.

5.4. Summary

We have studied the shell effects in the non-spherical nuclei, which may exist in the inner crust of a neutron star, by calculating single-particle energies in appropriate non-spherical potentials and extracting shell energies from these single-particle energies. These shell energies have been found to be somewhat smaller than the energy differences between different nuclear shapes at the densities of interest ($1.0\text{-}1.5\times10^{14}$ g/cm^3 or 0.06-0.09 fm^{-3}). It has also been found that the transitions from sphere to cylinder and from cylinder to slab occur at higher densities than those of the Thomas-Fermi calculation. Therefore, we conclude that the shell effects do not change the qualitative feature of the successive nuclear shape transitions, although they cause some quantitative change.

Chapter 6

Discussions

This chapter gives some discussions about the non-spherical nuclei in connection with the structure and evolution of a neutron star.

6.1. Layer in the neutron-star crust where non-spherical nuclei exist

As a result of the Thomas-Fermi calcultion in Chapter 4, we obtain the equation of state (EOS) of the neutron-star matter. The energy difference due to the nuclear shape change is rather small resulting in a relatively minor change in the EOS. The existence of non-spherical nuclei merely makes the transition from the ordinary matter to the dense uniform matter smoother. In Fig. 6-1 we show the energy per nucleon of the neutron-star matter. The energy in the density range 0.06-0.09 fm^{-3}, where non-spherical nuclei exist, is 7-9 MeV per nucleon, while the difference due to the different nuclear shapes is of the order of 1 keV per nucleon. Since we paid little attention to the high-density part of the EOS in constructing the energy-density functional, we now connect its low-density part to the high-density part of the β-stable EOS derived from a many-body calculation by Wiringa, Fiks and Fabrocini [11].

With this EOS we can calculate the density distribution in a neutron star by sloving the following Tolman-Oppenheimer-Volkoff (TOV) equation [42]:

$$\frac{dm}{dr} = 4\pi r^2 \rho, \tag{6.1a}$$

$$\frac{dP}{dr} = -\frac{\rho m}{r^2}\left(1+\frac{P}{\rho}\right)\left(1+\frac{4\pi P r^3}{m}\right)\left(1-\frac{2m}{r}\right)^{-1}, \tag{6.1b}$$

where P is the pressure and ρ is the matter density. In order to solve Eqs. (6.1a) and (6.1b) simultaneously, we need the EOS of the form

$$P=P(\rho). \tag{6.2}$$

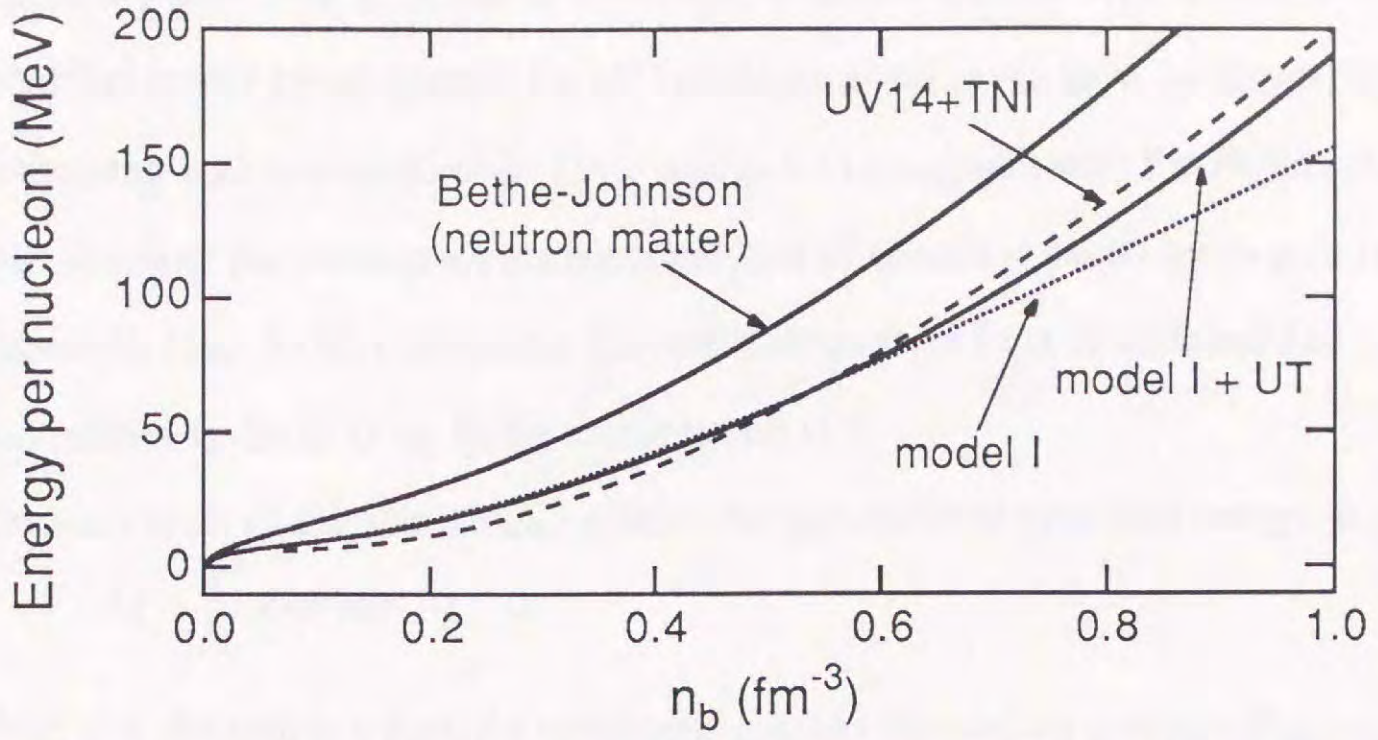

Fig. 6-1. Energy per nucleon relative to the neutron mass. UV14+TNI means a many-body calculation with the two-body potential UV14 and the three-body potential TNI by Wiringa, Fiks and Fabrocini [11]. This EOS is a refined version of EOS by Friedman and Pandharipande [12] in which some errors at high densities have been corrected. The curve labeled model I + UT is the one obtained by connecting the model I EOS at low denisties with the high density part of UV14+TNI. For comparison the EOS of pure neutron matter by Bethe and Johnson [13] is also shown.

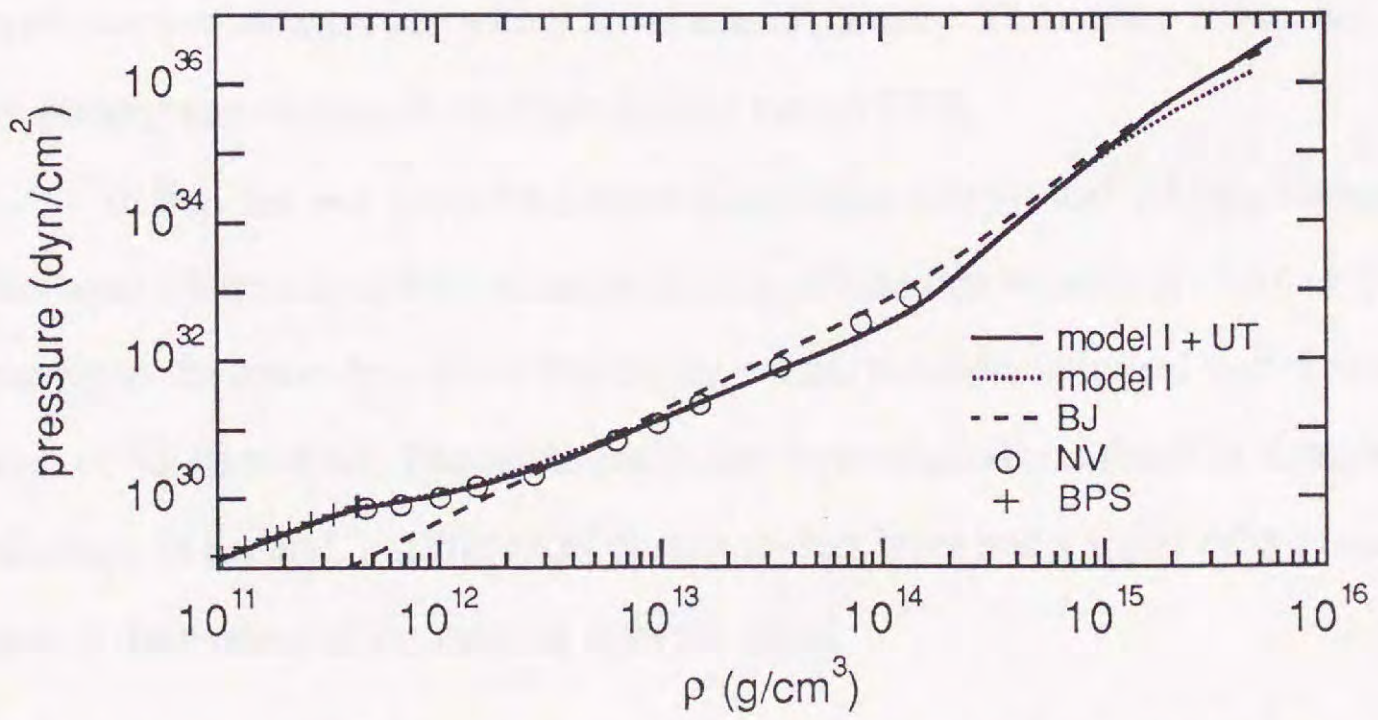

Fig. 6-2. Pressure as a function of matter density. BJ means the EOS of pure neutron matter by Bethe and Johnson [13]. Crosses indicate the EOS below the neutron drip point by Baym, Pethick and Sutherland [14]. Circles shows the Hartree-Fock calculation of the inner-crust matter by Negele and Vautherin[19].

Figure 6-2 shows the pressure as a function of matter density. At low densities, the modified model I EOS (model I + UT) is nearly equal to the EOS by Baym, Pethick and Sutherland with a mass formula [14], and is also consistent with the Hartree-Fock calculation of the inner-crust matter composed of spherical nuclei by Negele and Vautherin [19]. At high densities, the modified model I EOS is stiffened and approaches to the EOS by Bethe and Johnson [13].

The total mass of the star which includes the gravitational potential energy, is given by

$$M = \int_0^R 4\pi r^2 \rho dr \,. \tag{6.3}$$

Here, R is the radius where the pressure P reaches the surface pressure P_{surf}, or, alternatively, the density ρ reaches the surface density ρ_{surf}. The value of ρ_{surf} used by Arnett and Bowers [43] was 7.86 g/cm^3 which is the density of solid ^{56}Fe. In numerical calculations, two conditions, ρ_{surf}=7.86 g/cm^3 and ρ_{surf}=0, make no significant difference.

Figure 6-3 shows the gravatational mass of a neutron star as a function of the central density. The mass of a neutron star is mainly determined by the high-density part of the EOS above nuclear density. Roughly speaking a stiffer EOS can support a more massive neutron star with a lower central density. The curves in Fig. 6-3 reflect the present uncertainty on the high-density part of EOS.

In Fig. 6-4, we show the density distribution of a typical 1.4 $M_\odot$ neutron star. The layer where non-spherical nuclei exist is so thin that we enlarge the part of our interest in the lower box. From this figure we see that non-spherical nuclei exist in a layer of 70-80 m thick. The thickness of this layer depends on the EOS at high densities. In general, a stiffer EOS gives a thicker layer and a softer EOS gives a thinner layer if the masses of the neutron stars are equal.

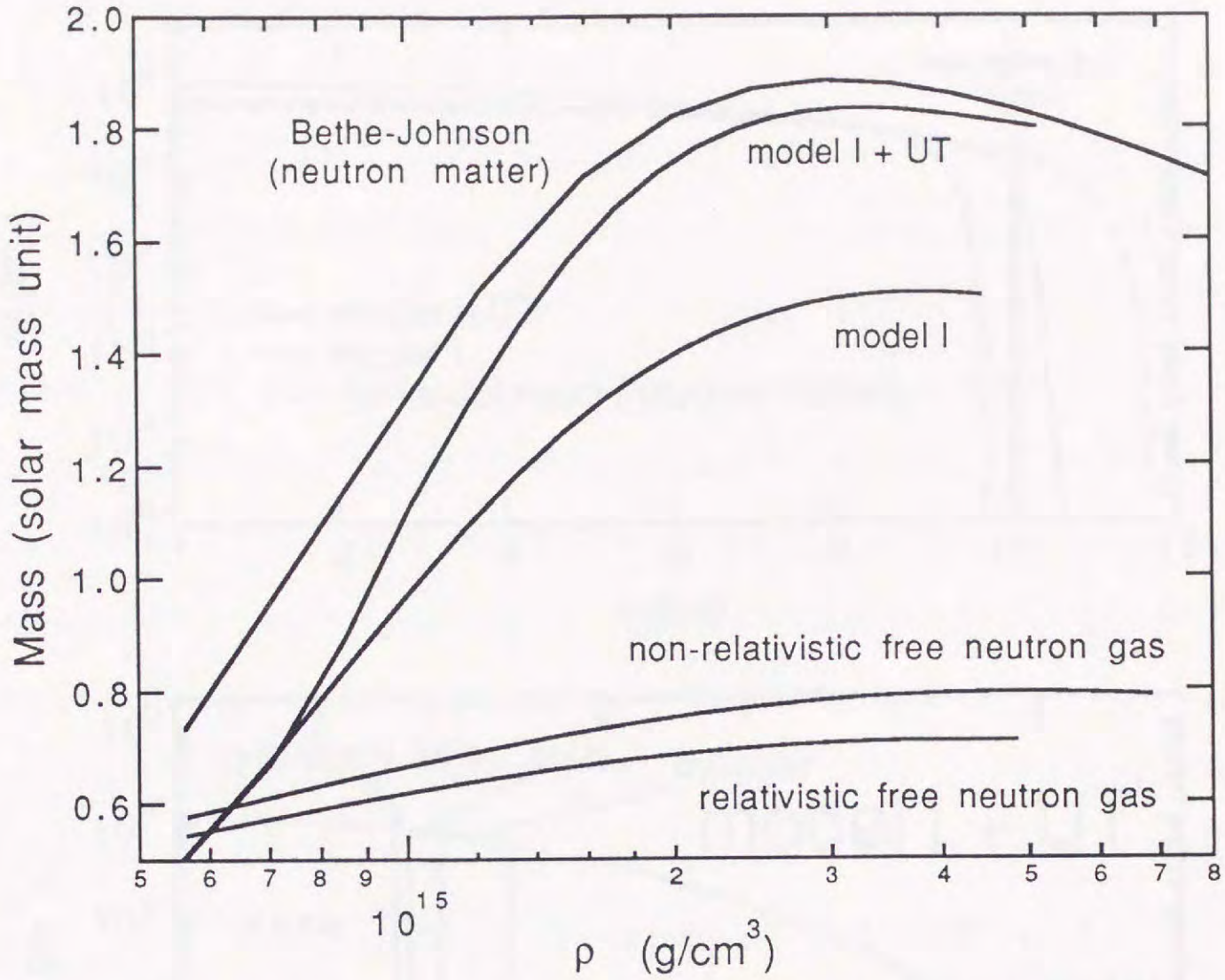

Fig. 6-3 Neutron star mass as a function of the central density calculated with EOS in Figs. 6-1 and 6-2. For comparison, we also show the curves for non-relativistic and relativistic free neutron gases.

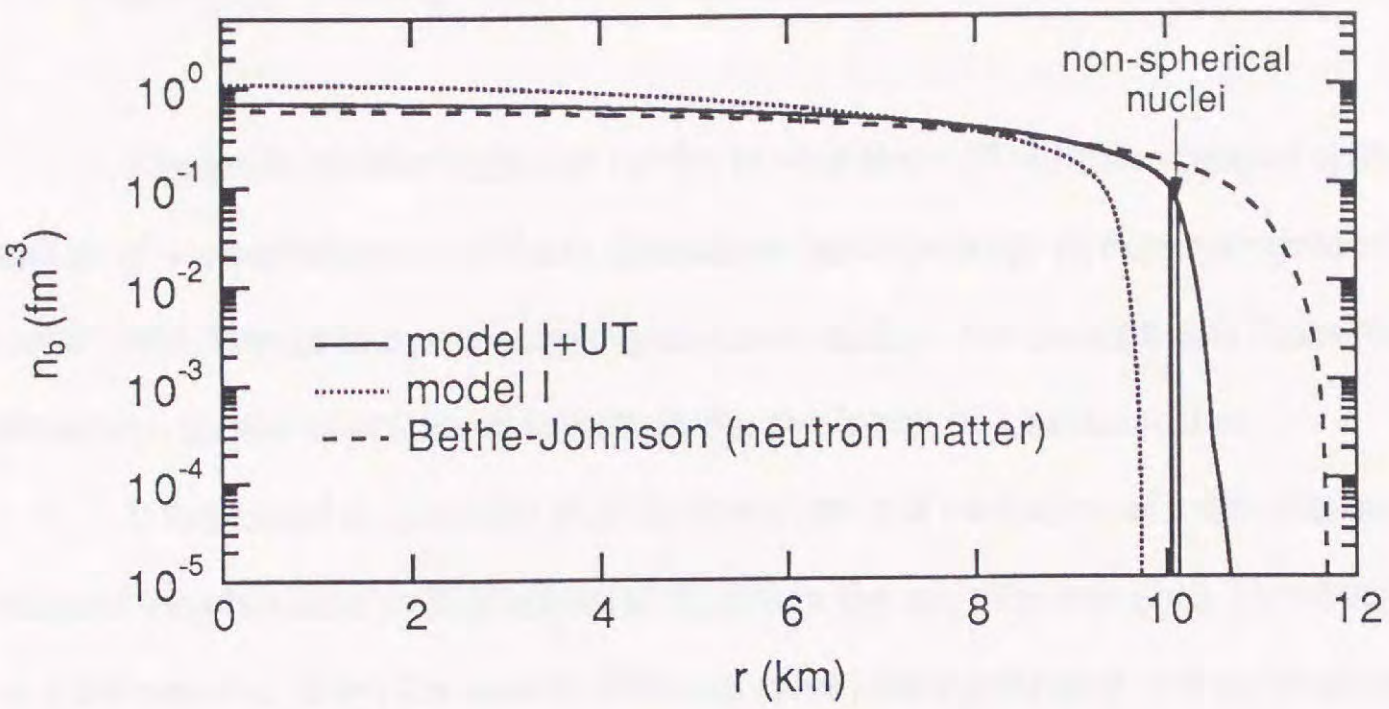

Fig. 6-4. Density distribution in a 1.4 $M_\odot$ star calculated with EOS of model I + UT shown in Figs. 6-1 and 6-2. In the upper box, density profiles calculated with model I EOS and neutron-matter EOS by Bethe and Johnson are also shown for comparison. The layer of non-spherical nuclei is shown for model I + UT. In the lower box, regions for various nuclear shapes are shown for model I + UT. The region for spherical hole nuclei is hardly distinguishable even in this enlarged figure.

6.2. Arguments relating with the structure and evolution of a neutron star

The layer of non-spherical nuclei is very thin (70-80m) compared with the radius of a neutron star (~10 km). Therefore the existentce of non-spherical nuclei will cause little change in macroscopic quantities, such as the neutron-star mass and radius. However, it may cause some effects in the evolution of a neutron star.

It is natural to consider that the structure and evolution of a neutron star mainly reflects the character of high-density matter in the neutron-star core. However, since any information from the core is obtained after passing through the layer of non-spherical nuclei, this layer may cause some anomalous effects.

In this thesis we have neglected temperature effects. The non-spherical nuclei will probably survive even if we take these effects into account in most cases. The energy difference between the lowest two phases is of the order of 0.1-1 MeV per cell. In a cell a majority of the nucleon degrees of freedom are frozen. If we assume the active degrees in a cell to be of the order of 10, then above energy difference corresponds to a temperature of 10^8-10^9 K, which is sufficiently higher than the temperature in the neutron-star crust except for a very young neutron star. However, in studing evolution of a hot young neutron star, it may be important to consider how the layer of non-spherical nuclei is formed at relatively high temperatures.

If we assume that the length of cylinders and the area of slab are comparable to the size of the layer in a neutron star, they may cause observable phenomena. Vibration of cylinders and slab may affect the energy transport from the neutron-star core to the surface.

The direction of the cylinders and slab can not be known from the present study. It might be determined by properties of the neutron star such as the strong magnetic field and the rapid rotation. For convenience we have assumed inifinitely long cylinders and slabs of infinitely large area. However, the length of cylinders and the area of slabs may not necessarily be comparable to the size of these layers in a neutron star. The diameter of cylinders and the width of slabs are of the order of only 10 fm. They are

much smaller than the thickness of these layers which are of the order of 10 m. Therefore, the direction of cylinders and slabs may not necessarily be the same over the star. Although we have singled out the most stable nuclear shape, it is also possible that the matter is a mixture of non-spherical phases because the energy difference between these phases is rather small. In fact, crystal structures found at the atomospheric temperature and pressure are not necessarily the most stable ones. For example we see both the diamond and graphite structure of carbon in our everyday life although the former has a larger free energy than the latter.

Nuclear shapes assumed in this thesis can be considered as one-, two- or three-dimensional spheres. These shapes are assumed because they minimize the surface areas, and accordingly the surface energies. Hence we have neglected deformation from these spheres. However, some deformation from these shapes probably exists in reality. As we have seen so far, the energy difference due to the geometry is quite small compared with the total binding energy as is often the case with atomic and molecular physics. Deformation of normal nuclei occurs essentially as a result of shell (quantumn mechanical) effects. Therefore it is possible that nuclei deform from the shapes assumed in this thesis. An approximate inclusion of the deformation may be usuful for the supernova matter. Ravenhall, Pethick and Wilson [1] argued continual change of the nuclear shape noting that the surface and Coulomb energy densities in the case of a d-demensional sphere can be written, respectively, as

$$E_s=u\sigma d/r \tag{6.4}$$

and

$$E_C=2\pi(exn^{in})^2 u f_d(u), \tag{6.5}$$

with

$$f_d(u)=\left\{\frac{2}{(d-2)\left(1-\frac{1}{2}d\,u^{1-2/d}\right)}+u\right\}/(d+2), \tag{6.6}$$

where r is the radius of the nucleus and the other symbols mean the quantities deifined in chapter 3. They argued that these expressions might be used even for fractional values of d and that the value of d could be considered as a sort of a fractal dimension.

Their treatment may be a usuful approximation for the supernova matter which can be realized as a transient matter in a supernova explosion. However, this treatment seems to be an oversimplification, and the author feels that a variety of microscopic structures in the neutron-star matter are possible as we see in solid state and molecular physics.

Nuclei with peculiar geometries may affect spinning of a pulsar. Pulsar glitches have been attributed to the sudden angular momentum transfer from the superfluid to the crust by catastrophic unpinning of neutron votex lines in the inner crust [44]. The layer of non-spherical nuclei does overlap the pinning region of neutron vortex [3]. Recently Mochizuki and Izuyama [45] presented a vortex trap/discharge model for pulsar glitches taking non-spherical nuclei into account. This line of studies has just begun and may provide a good description of glitch phenomena.

Chapter 7

Conclusion

We started a study on the nuclear shapes in the inner crust of a neutron star with the compressible liquid-drop model and predicted a possibility of successive change of the nuclear shape. The liquid-drop model provided us with a general result, based on a geometrical argument, that non-spherical nuclei become energetically favorable if the volume fraction of the nucleus in a cell exceeds a certain value. However, we could not know from this geometrical argument whether the volume fraction can exceed the critical value or not.

In the liquid-drop model we can not explicitly take into account the diffuseness of the nuclear surface. Moreover, in extremely neutron-rich nuclei treated in this paper the surfaces for neutrons and protons are not necessarily equal as are inferred from recent experiments on unstable nuclei. In order to go beyond the liquid-drop model, we performed the Thomas-Fermi calculation. In this calculation we paid special attention to the energy-density functionals and nucleon distributions because the surface energy is the most important nuclear energy to determine the nuclear shape. From this calculation we confirmed the liquid-drop prediction that the nuclear shape changes successively from sphere to cylinder, slab, cylindrical hole and spherical hole at densities $(1.0\text{-}1.5)\times10^{14}$ g/cm^3 or 0.06-0.09 fm^{-3}.

It is well known that shell effects are important in normal nuclei. The masses of normal nuclei are well reproduced by supplementing the shell energies to the semi-classical energies; we employed the same strategy to the non-spherical nuclei. We calculated the shell energies of non-spherical nuclei making full use of the results obtained from the Thomas-Fermi calculation. Then, we added the shell energies to the Thomas-Fermi energies of the matters composed of non-spherical nuclei. We found that, even in the presence of the shell energy, the conclusion of the Thomas-Fermi calculation persists qualitatively although there are some quantitative changes.

In conclusion, at densities (1.0-1.5)×10^{14} g/cm^3 in the inner crust of a neutron star, our familiar spherical shape is no longer stable but the stable nuclear shape changes successively from sphere to cylindrical, slab, cylindrical hole and spherical hole shape with increase of matter density.

More detailed studies will be necessary for more quantitative arguments of these non-spherical nuclei. The author hopes that the present work will serve as a starting point for such detailed studies and for understanding the evolution and structure of a neutron star.

Acknowledgments

The author wishes to express his gratitude to Prof. M. Yamada for continual encouragement and stimulating discussion. He would also like to express his thanks to Profs. T. Takatsuka, R. Tamagaki, H. Toki, I. Tanihata and K. Sato for their interests and comments on the subject of this thesis. He thanks Drs. M. Uno and T. Tachibana for providing him with tables of atomic mass predictions, and Messrs. N. Akino, H. Nakata, M. Takano, S. Matsumoto and A. Yamada for their assistance at the early stage of this work.

Appendix A

Coulomb energies for spherical and cylindrical nuclei in the compressible liquid-drop model

Since nuclei form a lattice we have to take into account the lattice contribution to the Coulomb energy. For a given periodic charge distribution $\rho(\boldsymbol{r})$, the Coulomb energy per cell is given by

$$W_{\mathrm{C}} = \frac{1}{2}\int_{\mathrm{cell}} \rho(\boldsymbol{r})\phi(\boldsymbol{r})d\boldsymbol{r}\,, \tag{A.1}$$

where $\phi(\boldsymbol{r})$ stands for the electrostatic potential, which is the solution of Poisson's equation:

$$\nabla^2\phi(\boldsymbol{r}) = 4\pi e\rho(\boldsymbol{r})\,. \tag{A.2}$$

Expanding $\rho(\boldsymbol{r})$ and $\phi(\boldsymbol{r})$ into Fourier series, and then eliminating $\phi(\boldsymbol{r})$ with use of Eq. (A.2), we obtain

$$W_{\mathrm{C}} = \frac{2\pi(e\,n^{in}\,x)^2}{a^3}\sum_{hkl}{}' \left(\frac{I_{hkl}}{|\boldsymbol{G}_{hkl}|}\right)^2 \tag{A.3}$$

Here, $\boldsymbol{G}_{hkl}$ is the reciprocal lattice vector given by

$$\boldsymbol{G}_{hkl} = h\boldsymbol{A} + k\boldsymbol{B} + l\boldsymbol{C}\,, \tag{A.4}$$

where h, k and l are integers, and $\boldsymbol{A}$, $\boldsymbol{B}$ and $\boldsymbol{C}$ are the primitive transformation vectors of the reciprocal lattice. The prime on the summation symbol means that the point $\boldsymbol{G}_{hkl}=0$ is excluded. The quantity I_{hkl} is given by

$$I_{hkl} = \int_{\Omega} d\boldsymbol{r}\,\exp\left(-i\boldsymbol{G}_{hkl}\cdot\boldsymbol{r}\right). \tag{A.5}$$

The symbol Ω denotes the domain occupied by protons (nucleus).

Because of the periodic boundary condition, we have

$$\int_{\Omega} d\boldsymbol{r}\,\exp\left(-i\boldsymbol{G}_{hkl}\cdot\boldsymbol{r}\right) = -\int_{\mathrm{cell}-\Omega} d\boldsymbol{r}\,\exp\left(-i\boldsymbol{G}_{hkl}\cdot\boldsymbol{r}\right), \tag{A.6}$$

where the integration in the right-hand side of (A.6) is performed over the cell except for Ω. Therefore, the expressions for hole nuclei are obtained by replacing u by $1-u$. In

the following, we present the relative Coulomb energies $w_{C1}(u, \mathit{shape}, \mathit{lattice})$ of spherical, cylindrical and slab-shape nuclei for the proton distribution described in Chapter 3.

The relative Coulomb energies in the cases of spherical nuclei are given by

$$w_{C1}(u, \text{sphere, bcc}) = C_1 (4u)^{4/3} \sum_{hkl}{}' \left[j_1\left(4^{-1/3} u^{1/3} C_2 R_{\text{bcc}}\right)/R_{\text{bcc}}^2 \right]^2 , \tag{A.7}$$

$$w_{C1}(u, \text{sphere, fcc}) = C_1 (2u)^{4/3} \sum_{hkl}{}' \left[j_1\left(2^{-1/3} u^{1/3} C_2 R_{\text{fcc}}\right)/R_{\text{fcc}}^2 \right]^2 \tag{A.8}$$

and

$$w_{C1}(u, \text{sphere, sc}) = C_1 u^{4/3} \sum_{hkl}{}' \left[j_1\left(u^{1/3} C_2 R_{\text{sc}}\right)/R_{\text{sc}}^2 \right]^2 \tag{A.9}$$

with

$$C_1=3(4\pi^2)^{-1}(6/\pi)^{1/3}, \qquad C_2=\pi(6/\pi)^{1/3}, \tag{A.10}$$

$$R_{\text{bcc}}=[(h+k)^2+(k+l)^2+(l+k)^2]^{1/2}, \tag{A.11}$$

$$R_{\text{fcc}}=[(h+k-l)^2+(h-k+l)^2+(-h+k+l)^2]^{1/2}, \tag{A.12}$$

$$R_{\text{sc}}=(h^2+k^2+l^2)^{1/2}. \tag{A.13}$$

Here, j_1 denotes the spherical Bessel function of the first order.

In the cases of cylindrical nuclei, the relative Coulomb energies are written as

$$w_{C1}(u, \text{cylinder, hex}) = \frac{2u}{3\pi^2} \sum_{hk}{}' \left[J_1\left(\sqrt{2\sqrt{3}\,\pi u}\, R_{\text{hex}}\right)/R_{\text{hex}}^2 \right]^2 , \tag{A.14}$$

$$w_{C1}(u, \text{cylinder, ss}) = \frac{u}{2\pi^2} \sum_{hk}{}' \left[J_1\left(2\sqrt{\pi u}\, R_{\text{sq}}\right)/R_{\text{sq}}^2 \right]^2 \tag{A.15}$$

with

$$R_{\text{hex}} = \left[h^2 + \frac{1}{3}(h-2k)^2 \right]^{1/2} , \tag{A.16}$$

$$R_{\text{ss}}=(h^2+k^2)^{1/2}. \tag{A.17}$$

Here, J_1 denotes the cylindrical Bessel function of the first order.

Appendix B

Determination of parameter values in the energy density functional ε

In determining the parameter values in the energy density functional ε, we use an EOS of pure neutron matter from a many-body calculation as well as gross properties of β-stable nuclei.

First, we determine the potential energy density of pure neutron matter in the following way. We write a tentative potential energy density as

$$v_{n0}(n) = b_{10}n^2 + \frac{b_{20}n^3}{1 + b_3 n} \tag{B.1}$$

and choose the values of b_{10}, b_{20} and b_3 to fit eq. (B.1) supplemented by a kinetic term to the EOS of neutron matter by Friedman and Pandharipande [12] at $n \leq 0.4$ fm^{-3}. In order to get a better fit to masses and sizes of normal nuclei, we introduce a new parameter ξ as

$$b_1 = \xi b_{10},\ b_2 = \xi b_{20}\,. \tag{B.2}$$

The parameter β in Eq. (4.5) is related to the surface symmetry energy, but its value is very uncertain. Therefore, we take two typical cases, β=0 and β=1. We also consider the case α=0 in addition to the case α=1, since, in many Thomas-Fermi calculations, the inhomogeneous energy ε_g does not include the explicit kinetic energy term as in Eq. (4.14); in such calculations both the kinetic and potential energies are supposed to be represented by a term similar to the last term of Eq. (4.14).

Values of the five independent parameters a_1, a_2, a_3, ξ and F_0 in the energy density functional ε are determined so as to reproduce approximately the smoothed β-stability line and the smoothed nuclear masses and charge radii on this β-stability line. These β-stability line and masses are taken from ref. [46], and the charge radii are

calculated from the table in ref. [29]. The values of these input data and results calculated with models I~IV are listed in table B-1.

Table B-1
List of the empirical data (input data) and the corresponding values calculated with models I~IV. In (a) listed is the proton number on the smoothed β-stability line corresponding to the indicated mass number A, in (b) the smoothed mass excess (in MeV) of the nucleus having the proton number given in (a), in (c) the root-mean-square radius.

A	input data	model I	II	III	IV
(a) proton number					
25	12.41	11.774	11.747	11.765	11.771
47	21.855	21.463	21.413	21.448	21.455
71	31.695	31.563	31.499	31.544	31.552
105	45.085	45.218	45.148	45.196	45.204
137	57.145	57.495	57.436	57.475	57.482
169	68.845	69.303	69.267	69.279	69.294
199	79.61	80.003	80.003	79.996	80.002
225	89.18	89.014	89.053	89.016	89.021
245	96.39	95.797	95.868	95.805	95.809
(b) mass excess in MeV					
25	−13.10	−9.8929	−9.3022	−5.9961	−11.213
47	−46.17	−44.992	−44.101	−40.723	−45.303
71	−72.38	−73.188	−72.180	−69.202	−72.897
105	−89.69	−91.667	−90.764	−88.691	−91.031
137	−84.89	−86.967	−86.346	−85.284	−86.341
169	−61.18	−62.645	−62.395	−62.410	−62.239
199	−23.12	−23.562	−23.689	−24.745	−23.495
225	21.22	22.044	21.600	19.629	21.740
245	61.21	64.050	63.382	60.700	63.423
(c) root mean square radius in fm					
25	3.029	2.976	3.001	2.943	3.030
47	3.567	3.523	3.554	3.489	3.578
71	3.997	3.965	4.000	3.929	4.020
105	4.487	4.458	4.498	4.419	4.514
137	4.874	4.841	4.883	4.797	4.896
169	5.206	5.174	5.218	5.126	5.229
199	5.466	5.453	5.499	5.400	5.509

References

[1] D. G. Ravenhall, C. J. Pethick and J. R. Wilson, Phys. Rev. Lett. **50** (1983) 2066

[2] M. Hashimoto, H. Seki and M. Yamada, Prog. Theor. Phys. **71** (1984) 320

[3] C. P. Lorenz, D. G. Ravenhall and C. J. Pethick, Phys. Rev. Lett. **70** (1993) 379

[4] K. Oyamatsu, M. Hashimoto and M. Yamada, Prog. Theor. Phys. **72** (1984) 373

[5] J. Cooperstein and E. A. Baron, in Supernovae, ed. A. G. Petschek (Springer-Verlag, New York, 1990) p. 213

[6] J. M. Lattimer and F. D. Swesty, Nucl. Phys. **A535** (1991) 331

[7] R. D. Williams and S. E. Koonin, Nucl. Phys. **A435** (1985) 844

[8] M. Lassaut, H. Flocard, P. Bonche, P. H. Heenen and E. Suraud, Astron. Astrophys. **183** (1987) L3

[9] J. Arponen, Nucl. Phys. **A191** (1972) 257

[10] K. Oyamatsu, in Unstable nuclei in astrophysics, ed. S. Kubono and T. Kajino (World Scientific, Singapore, 1992) p. 327

[11] R.B. Wiringa, V. Fiks and A. Fabrocini, Phys. Rev. **C38** (1988) 1010

[12] B. Friedman and V.R. Pandharipande, Nucl. Phys. **A361** (1981) 502

[13] H.A. Bethe and M.B. Johnson, Nucl. Phys. **A230** (1974) 1

[14] G. Baym, C.J. Pethick and P. Sutherland, Astrophys. J. **170** (1971) 299

[15] P. Haensel and B. Pichon, Astron. Astrophys. **283** (1994) 313

[16] H.A. Bethe, G. Baym and C.J. Pethick, Nucl. Phys. **A175** (1971) 225

[17] D.G. Ravenhall, C.D. Bennett and C.J. Pethick, Phys. Rev. Lett. **28** (1972) 978

[18] Z. Barkat, J.R. Buchler and L. Ingber, Astrophys. J. **176** (1972) 723

[19] J. W. Negele and D. Vautherin, Nucl. Phys. **A207** (1973) 298

[20] D.Q. Lamb, J.M. Lattimer, C.J. Pethick and D.G. Ravenhall, Phys. Rev. Lett. **41** (1978) 1623

[21] S.A. Bludman and C.B. Dover, Phys. Rev. **C22** (1980) 1333

[22] C. F. von Weizsäker, Z. Phys. **96** (1935) 431

[23] M. Brack, B.K. Jennings and Y.H. Chu, Phys. Lett. **65B** (1976) 1

[24] H. S. Köhler, Nucl. Phys. **A258** (1976) 301

[25] H. Krivine, J. Treiner and O. Bohigas, Nucl. Phys. **A336** (1980) 155

[26] R. Brockmann and R. Machleidt, Phys. Rev. **C42** (1990) 1965

[27] A.H. Wapstra, G. Audi and R. Hoekstra, Atomic Data and Nuclear Data Tables **39** (1988) 281

[28] L.R.B. Elton and A. Swift, Nucl. Phys. **A94** (1967) 52

[29] H. de Vries, C. W. de Jager and C. de Vries, Atomic Data and Nuclear Data Tables **36** (1987) 495

[30] T. Tachibana, M. Uno, M. Yamada and S. Yamada, Atomic Data and Nuclear Data Tables **39** (1988) 251

[31] J. Jänecke and P.J. Masson, Atomic Data and Nuclear Data Tables **39** (1988) 265

[32] R. Ogasawara and K. Sato, Prog. Theor. Phys. **68** (1982) 222

[33] J. Dudek, Z. Szymanski and T. Werner, Phys. Rev. **C23** (1981) 920

[34] M. Beiner, H. Flocard, N. van Giai and P. Quentin, Nucl. Phys. **A238** (1975) 29

[35] G.A. Leander, J. Dudek, W. Nazarewicz, J.R. Nix and P. Quentin, Phys. Rev. **C30** (1984) 416

[36] A. Bohr and B.R. Mottelson, Nuclear Structure, vol. 1 (Benjamin, New York,1969) p. 324

[37] T. Tachibana, M. Takano and M. Yamada, JAERI-M 91-032 (1991)

[38] M. Uno, T. Tachibana, M. Takano, H. Koura and M. Yamada, Proc. Conf. on Atomic Masses and Fundamental Constants, Bernkastel-Kues, 1992, eds. R. Neugart and A. Wöhr (Institute of Physics Publishing, Bristol, 1993) p. 117

[39] V.M. Strutinsky, Nucl. Phys. **A95** (1967) 420; **A122** (1968) 1

[40] M.A. Preston and R.K. Bhaduri, Structure of the nucleus (Addison-Wesley, Massachusetts, 1975) p. 579

[41] P. Bonche and D. Vautherin, Nucl. Phys. **A372** (1981) 496

[42] S.L. Shapiro and S.A Teukolsky, "Black Holes, White Dwarfs, and Neutron Stars", (John Wiley, New York, 1983)

[43] W.D. Arnett and R. L. Bowers, ApJ supplement **33** (1977) 415

[44] P. Anderson and N. Itoh, Nature **256** (1975) 25

[45] Y. Mochizuki and T. Izuyama, preprint (1994)

[46] M. Yamada, Prog. Theor. Phys. **32** (1964) 512

主な研究業績

		題目	掲載誌	年月	共著者
論文	○	Further Study of the Nuclear Shape in High-Density Matter	Prog. Theor. Phys.**72** pp. 373-375	1984年8月	橋本正章 山田勝美
	○	Nuclear Shapes in the Crust of the Neutron Stars and in the Core of Supernovae	Proc. Conf. on *Unstable Nuclei in Astrophysics* (World Scientific) pp. 327-330	1992年	
	○	Nuclear shapes in the inner crust of a neutron star	Nucl. Phys. **A561** pp. 431-452	1993年8月	
	○	中性子星内殻における原子核の形状	素粒子論研究８８巻 pp. B28-B35	1993年11月	
	○	Shell energies of non-spherical nuclei in the inner crust of a neutron star	Nucl. Phys. A	（掲載決定）	山田勝美
その他の論文		核物質に対するクラスター変分法	素粒子論研究７５巻 pp.C18-C19	1987年6月	吉越敏郎* 山田勝美
	○	Bose粒子系に対する有限温度のクラスター変分法	素粒子論研究７５巻 pp. C19-C20	1987年6月	吉越敏郎 山田勝美
		Cluster Variation Method for Finite-Temperature Systems II ---Formulation for Nuclear Matter with a Central Potential ---	Prog. Theor. Phys. **74** pp. 493-501	1988年2月	吉越敏郎* 山田勝美

(注) ○印は著者の主業績を、連名者の*はfirst authorを表す。